DEVELOPMENT OF A SHORT-BASELINE TRANSIENT EM MARINE SYSTEM AND ITS APPLICATION IN THE STUDY OF THE TAG HYDROTHERMAL MOUND

by

Graeme Cairns

A thesis submitted in conformity with the requirements
for the degree of Doctor of Philosophy
Graduate Department of Physics
University of Toronto

DEVELOPMENT OF A SHORT-BASELINE TRANSIENT EM MARINE SYSTEM AND ITS APPLICATION IN THE STUDY OF THE TAG HYDROTHERMAL MOUND

Doctor of Philosophy, 1997, Graeme Cairns
Department of Physics, University of Toronto

Abstract

Seafloor hydrothermal mounds are accumulations of polymetallic sulfides that are produced by hydrothermal processes along active plate boundaries. While surficial rocks and fluids of such mounds have been extensively sampled, few geophysical methods are capable of resolving their structure at depth. Consequently, little is known of the resource value of individual deposits. Electrical conductivity is a parameter sensitive to variations in rock porosity, pore fluid salinity and temperature. Perhaps nowhere on Earth are these parameters more variable than in a hydrothermal environment, suggesting that conductivity measurements made with an appropriate technique are a method of choice for imaging the internal features of these deposits.

Innovative transient electric dipole-dipole instruments have been developed for this purpose. The instruments are compact, autonomous, and have dual transmitter/receiver capability. When transmitting, the instruments generate a 3 A bipolar square wave of variable base frequency. When receiving, the instruments act as recording voltmeters which measure the horizontal components of the seafloor electric field.

The instruments were deployed in their first trial in a survey of the Trans-Atlantic Geotraverse (TAG) hydrothermal mound on the mid-Atlantic ridge using the Alvin submersible. One instrument was configured as a transmitter and another as a receiver. Alvin carried the instruments to the seafloor where the receiver was deployed near the center of the mound. The transmitter was then carried through a survey path which circled the re-

ceiver at a range of $\sim$ 70 m, providing measurements of axial variations in the mound's conductivity.

The survey lasted 3.5 hours. One receiver component was damaged during deployment. Measurements made at 12 sites on the second receiver component are interpreted in terms of a uniform seafloor model and a two-layered seafloor model. Results from the layered seafloor interpretation are rejected on the basis of eigenparameter error analysis. Apparent conductivities for the uniform seafloor model range from 1.4 to 15.9 S/m, being generally higher than the 3.2 S/m of seawater. Sensitivity analysis indicates that these values primarily reflect structure over a depth interval of 10 to 30 meters below the seafloor. The results are discussed in terms of known geology of the TAG mound.

Acknowledgments

Throughout the years of work which resulted in this thesis, I have been deeply grateful for the support and assistance of many colleagues, friends and relatives. Foremost among these is my supervisor, Professor R. Nigel Edwards. His vision guided this project from its inception, and his kindness, humour and enthusiasm added immeasurably to the pleasure of the work. I also owe much to the Edwards family, whose hospitality has furnished me with many fond memories, and to Dr. Rob Evans who was involved in the early stages of this project and contributed significantly to the instrument development and the TAG experiment.

One of the most pleasant aspects of my graduate experience has been the close association and cooperation among the faculty and students in the geophysics division. Professors Gordon West, Richard Bailey and Jerry Mitrovica have been mentors whose example at both professional and personal levels I shall seek to emulate. Professors West and Bailey contributed incisive critiques of my thesis and made many valuable suggestions. The meticulous proof-reading of Professor Kim Strong from atmospheric physics also saved the text from many inconsistencies.

Professors Steve Scott and Hisashi Utada, Dr. Richard Von Herzen, Dr. Peter Rona, Dr. Lawrie Law, and Dr. Spahr Webb are scientists whom I met in the course of my campaigns at sea. Their efforts on behalf of my experiments and their ongoing encouragement have meant a great deal to me. I am also grateful to the captains and crews of the several ships that we sailed on, who so often went beyond the call of duty in their efforts to make our experiments successful.

The initial development of the instruments took place under severe time restrictions. The members of PERC worked long hours on the project, and the design of the instruments owes much to their input. The personal kindness of Peter Hurley, Steve Bigg and Alan Graham made the intense pressures of those days much easier to bear. Khader Khan was also a great help when it came time to write up my thesis.

While many contributions to my work were made by my fellow graduate students, I am most grateful to them for the friendship which provided the social fabric of my life throughout graduate school. Roderick Fisher, Liming Yu, Marion Jegen, Marc Constantine, Constantine Latychev, Jianwen Yang, Mladen Nedimovic and Glen Milne were compatriots who enriched my leisure time immensely.

Finally I would like to thank my parents, John and Beverley, without whose example and encouragement I would never have reached this point. While my choice of career seems somewhat perplexing to them, their unconditional support buoyed me through many dark moments.

This project was supported in part by grants to Professor Edwards from the Natural Sciences and Engineering Research Council of Canada, and by the National Science Foundation. I received financial support from the Department of Physics in the form of an E.F. Burton Fellowship and a University of Toronto Open Fellowship, from the Natural Sciences and Engineering Research Council of Canada, and from from the Ontario Government through the Ontario Graduate Scholarship (OGS) Plan.

Contents

List of Figures

List of Tables

Chapter 1

Introduction

1.1 Context of the Thesis

When the advent of deep-ocean manned submersibles first allowed scientists to explore the ocean depths in the mid-1970s, one of their first priorities was the search for massive sulfide deposits created by thermal springs along mid-ocean ridge spreading centers. Such deposits on land, such as the Cretaceous Troodos ores of Cyprus and the Archean Noranda deposits of Canada, are important sources of copper, zinc, lead, silver and gold. Their frequent association in the geologic record with basalts of submarine origin had led, by the mid-1960s, to a consensus that they were initially formed through hydrothermal activity on the ancient seafloor (Bonatti, 1975; Lydon, 1988). Existence of widespread hydrothermal activity along modern spreading centers was inferred from discrepancies of up to 40% between measurements of conductive heat flow and theoretical plate cooling models (Lister, 1972). It was therefore speculated that modern analogs of land deposits might be observed in the process of formation on the seafloor. In 1966, the discovery from surface ships of metalliferous hydrothermal brines and sediments in the Atlantis II Deep deposits of the Red Sea provided a partial confirmation of this theory (Miller *et al.*, 1966). In 1973, the French submersible *Archimede* made the first manned exploration of a ridge crest, and the next decade witnessed spectacular discoveries of active massive sulfide mounds along the Galapagos Rift (Corliss *et al.*, 1979), the East Pacific Rise (Spiess *et al.*, 1980; Ballard *et al.*, 1981; Hekinian *et al.*, 1983), and the Mid-Atlantic Ridge (Rona *et al.*, 1986).

Although the cost of mining such deposits precludes their present classification as ores, active mounds on the seafloor are natural laboratories to study ore-forming processes.

Investigations at sea provide insights into the circumstances surrounding ore formation which guide the search for mineral deposits on land. Seafloor deposits are furthermore products of a hydrothermal convection process which has a mass flow rate comparable to that of the Amazon River and is estimated to account for 20% of the Earth's total heat loss, with profound implications for ridge dynamics and ocean chemistry (Rona, 1986; 1988). This dual significance from both economic and scientific perspectives has made hydrothermal mineralization at seafloor spreading centers one of the most actively researched subjects in the Earth Sciences.

While surficial rocks and fluids of hydrothermal mounds have been extensively sampled, few measurements have been made which are sensitive to the structure at depth. As a result, little is known of the size and resource value of individual deposits. Despite a clear need for measurements imaging the distribution of mineralization, fluid convection and the root structure, hydrothermal mounds are intractable targets for most geophysical techniques.

Sulfide mineral deposits on land are routinely investigated using electromagnetic methods which measure the distribution of electrical conductivity. Such measurements are sensitive to variations in rock porosity, pore fluid salinity and temperature. Perhaps nowhere on earth are these parameters more variable than in a hydrothermal environment, suggesting that conductivity measurements made with an appropriate technique may be a method of choice for imaging the internal features of these deposits as well as the structural controls of the regional geology.

Recent advances in the theory of marine electromagnetic methods are leading to new techniques which are suited to this purpose. Initially developed in the frequency domain, these methods are now beginning to exploit the advantages of broadband time domain measurements which have gained popularity for surveys on land. Modeling suggests that one system, the transient electric dipole-dipole, is sensitive to seafloor conductivities over a broad range of conditions (Edwards and Chave, 1986; Cheesman *et al.*, 1987). This system furthermore lends itself to the development of compact, autonomous instruments which are well suited to submersible-based surveys. Such a system was developed for this thesis, and is described here along with the results of its first trial on an active hydrothermal mound.

1.2 Hydrothermal Mounds on Mid-Ocean Ridges

On a global scale, the distribution of hydrothermal mineralization on mid-ocean ridge spreading centers is poorly understood. Over 100 deposits have been discovered on the less than one percent of the $\sim 55,000$ km global length of spreading centers that has been investigated systematically (Rona, 1988), ranging from small mineral showings a few meters across to mature deposits estimated to contain several million tones of sulfides. Although a full spectrum of deposit sizes has been observed at ridge axes at all spreading rates, deposits seem to occur more often on faster spreading ridge segments, while those on slow spreading centers tend to be larger. The latter is explained by the longer residence time of a portion of the oceanic crust near heat sources beneath the rift valley at slow spreading rates, permitting superposition of the products of multiple mineral forming cycles driven by episodic magmatic intrusions. Sediment-hosted mounds occur when the ridge axis is close to a continental margin that acts as a source of erosional debris. While rare, it is thought that the largest deposits may form under these circumstances due to the efficiency of sediments in conserving hydrothermal precipitates, and that their quick encapsulation in sedimentary structures increases the probability that they will be preserved in the geologic record. Sediment-hosted deposits are unusually significant from a Canadian perspective due to the presence of the heavily sedimented Middle Valley off the coast of Vancouver Island. As over 99% of the global ridge system is unsedimented, however, the majority of the deposits are mounds which outcrop from a basaltic substrate.

The basic hydrothermal process leading to the formation of the deposits is similar at the different sites (Figure 1.1). Seawater, percolating through permeable portions of the crust in the axial zone, descends to depths of several kilometers where it is heated by magmatic intrusions. Complex two-way reactions with the basalt matrix result in the precipitation of magnesium and sulfate from the seawater, and the dissolving of calcium, silicon, and metals such as copper, iron, manganese and zinc from the basalt. Focused by the local permeability structure, the acidic, metal-enriched solution ascends towards the seafloor, where it discharges at flow rates of up to 5 m/sec and temperatures of up to 360°C. Mixing with the alkaline seawater, cations from the solution combine with sulfate to form sulfides of zinc, copper and iron. If the hydrothermal solution is more dense than the surrounding seawater, it pools to form ponded deposits such as those of the Red Sea. More commonly, the solution vents in dark buoyant plumes of suspended particles which emanate from tall chimneys up to 10 meters high formed of precipitated sulfides and anhydrite. A single such "black smoker" chimney with a typical flow rate of 10 liters

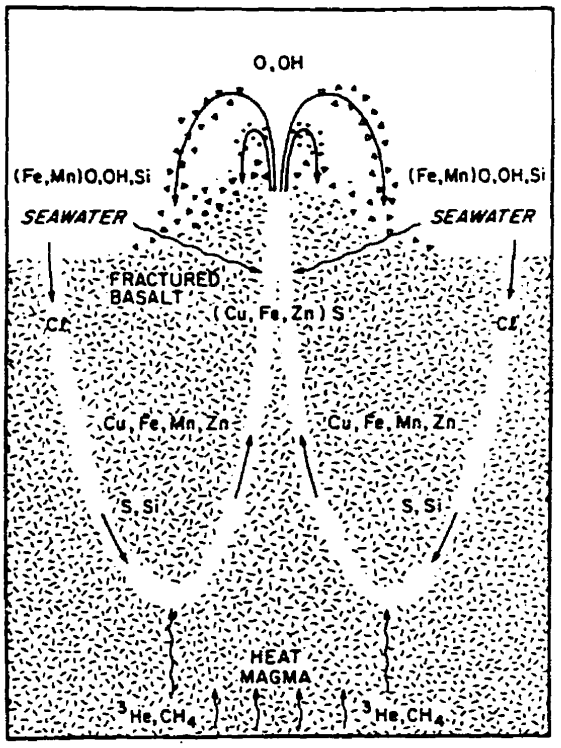

Figure 1.1: Hydrothermal mineralization process.

per second may vent 100 kg of metal per day (Hekinian, 1984), and has a convective heat flux equivalent to the conductive heat flow along a ridge segment about 5 km long extending out to a distance of 30 km on each side (Macdonald, 1982).

The accumulation of hydrothermal mounds is an inefficient process. While some of the plume particles rain down on the seafloor around the vent site, the majority are carried off by ocean currents and eventually settle as metalliferous sediment ubiquitous in the ocean basins. Hydrothermal mounds evolve primarily through the growth and collapse of chimneys and by mineral precipitation within the resulting breccia when seawater, entrained into the porous structure, mixes with upwelling hydrothermal fluids. The diluted hydrothermal fluids which are vented under these circumstances are of intermediate to low temperature, and are known as "white smokers" and "shimmering waters" respectively. A mature hydrothermal mound will typically display a full spectrum of hydrothermal vent solutions, with a spatial distribution reflecting the zonation of fluid mixing within the mound.

The structure of hydrothermal mounds observed in the geologic record and on the seafloor bears witness to this formative process (Lydon, 1984; 1988; Tivey *et al.*, 1995; Humphris

et al., 1995). The massive sulfide lens of such deposits is typically composed of 60% or more sulfide minerals, of which pyrite is by far the most common while chalcopyrite, pyrrhotite and sphalerite occur as subsidiary minerals. The lens is covered by a hard crust composed of partially oxidized fine grained sedimented sulfides which have settled from the plume and amorphous silicates which precipitate from the ubiquitous low temperature diffuse flow. In contrast, the interior of the lens is composed of a coarse pyrite breccia of chimney fragments, cemented in a loose matrix of pyrite and anhydrite which precipitated within the mound. Anhydrite is more abundant in active mounds than in relicts, as its retrograde solubility makes it dissolve in the waning stages of hydrothermal activity. A decrease in the ratio of chalcopyrite to sphalerite, or copper to zinc, is frequently observed with distance from the central feeder pipe, due to the remobilization of zinc by seawater entrainment within the mound. Where the sulfide lens has spilled onto the seafloor there is a sharp transition to basalt. Under most of the mound, however, there is a gradual transition to the stockwork zone through which the hydrothermal fluids ascend. Deep structural levels exposed by erosion in ophiolite-hosted land deposits show pipe-like bodies 100-200 m in diameter in which the basalts have been intensely altered and leached by rising hydrothermal fluids (Cann and Edmond, 1988). These alteration pipes appear to link 1-2 km below the ancient ocean floor in what are inferred to be hydrothermal reaction zones. Within these zones, copper, zinc and manganese are significantly depleted and fluid inclusions in the rock show sealing temperatures of 350-400°C, and approximately seawater salinity. The reaction zones lie close to the top of the ophiolite plutonic complex, suggesting that the circulation was driven by heat from the magma chamber.

1.3 Factors Affecting Conductivity

Electrical conduction in surface rocks is primarily electrolytic, occurring by ion transport in pore fluids and not significantly through the mineral matrix itself. The reason for this hinges on the concept of connectivity: while many rocks contain conductive minerals, the degree to which these influence the overall conductivity of the matrix depends on the extent to which continuous pathways for current flow exist between their grains. With the same bulk mineral content, dry rocks containing no pore fluids therefore exhibit conductivities ranging over orders of magnitude depending on the rock texture (Parkhomenko, 1967). Generally, the connectivity of fluid pathways for electrolytic conduction through the pores is far higher than that of electronic pathways in the rock matrix. This is

particularly true for fluid-saturated rocks in the shallow seafloor.

The parameters governing electrolytic conduction are related through Archie's Law (Archie, 1942), an empirical formula which provides a reasonable approximation for the conductivity of many surface rocks:

$$\sigma_f = \frac{\phi^m S^n \sigma_s}{A} \ (S/m), \tag{1.1}$$

where σ_f is the rock's overall formation conductivity, ϕ is the porosity, S is the fraction of the pores filled with fluid, and σ_s is the conductivity of the pore fluid. The saturation exponent n is a constant which is ≈ 2.0 for water saturation of more than 30% of the pore space. The exponent m is called the cementation factor. Its value characterizes the rock texture, ranging from 1.3 for unconsolidated sand to 2.5 for well-cemented granular rocks. A is a constant generally in the range $0.5 \leq A \leq 2.5$. In marine sedimentary rocks, $0.6 \leq A \leq 1.3$ (Parkhomenko, 1967).

For high porosity sedimentary rocks in the shallow seafloor, one may generally assume that $S = 1$ and that pore fluid is seawater. The conductivity of seawater is controlled almost entirely by salinity and temperature, which respectively determine the number of ions available for charge transport and the viscosity of the fluid through which they travel. The salinity of seawater falls in the range 32-38 parts per thousand, and to first order may be considered constant. To a reasonable approximation, the temperature dependence of seawater conductivity is given by the following relationship from Becker *et al.* (1983):

$$\sigma_s = 3 + T/10 \ (S/m) \tag{1.2}$$

where T is the temperature in °C. At the typical deep ocean temperature of 2°C, this gives $\sigma_s = 3.2$ S/m, the fairly uniform seawater conductivity observed below the thermocline (Chave and Cox, 1982).

While the relationships stated above are valid for the electrical conductivity of a broad range of rocks found on the shallow seafloor, their applicability in the unusual conditions of a hydrothermal environment deserves some examination. Reported conductivity ranges for land samples of the major constituents of hydrothermal mounds are shown in Table 1.1. As massive sulfide deposits may be 80% pyrite with significant amounts of chalcopyrite, the assumption implicit in Archie's Law that electronic conduction through

		Conductivity (S/m)	
Mineral	Formula	Range	Average
Pyrite	FeS_2	$0.7 - 3.4 \times 10^4$	3
Chalcopyrite	$CuFeS_2$	$3 - 8.3 \times 10^4$	250
Sphalerite	ZnS	$10^{-7} - 0.7$	0.001
Anhydrite	$CaSO_4$		10^{-9}
Quartz	SiO_2	$5 \times 10^{-15} - 2.5 \times 10^{-11}$	
Wet Fractured Basalt			0.1

Table 1.1: Conductivities of major constituents of hydrothermal mounds (Telford, 1976).

the rock matrix is negligible must be questioned. Francis (1985) reports a conductivity of 29 S/m for an air-dried pyrite sample from a seafloor hydrothermal mound, but the *in situ* bulk sulfide conductivities that he measured had the much lower values of 2-5 S/m, implying a lack of connectivity in the sulfide matrix. Pyrite ore samples on land exhibit conductivities as high as 7 S/m (Telford, 1976), but generally less than 1 S/m (Parasnis, 1956). Although inconclusive, these results suggest that despite high mineral grade, connectivity within the matrix of massive sulfide deposits is generally insufficient for electronic conduction to play a major role. This should be particularly true of active hydrothermal mounds in which chimney clasts are only loosely cemented by a matrix which includes significant amounts of anhydrite.

The salinity of hydrothermal fluids may vary considerably from that of seawater. Rona (1988) reports salinities ranging from 21 parts per thousand to 70 parts per thousand for fluids venting from hydrothermal mounds, and up to 320 parts per thousand for the Red Sea hydrothermal brines. Where such data is available, the pore fluid conductivity is more appropriately calculated from the following semi-empirical formula (Cheesman, 1989; Accerboni and Mosetti, 1967):

$$\sigma_s = \left[A + B\frac{T^{1+k}}{1+T^{\lambda}}\right]\frac{S}{1+S^h}e^{-\epsilon S}e^{-\zeta(S-S_0)(T-T_0)} \ (S/m), \tag{1.3}$$

where $A = .21923$ S/m, $B = .012842$ S/m, $k = .0320$, $\lambda = .00290$, $h = .1243$, $\epsilon = .000978$, $T_0 = 20°C$, $\zeta = .0000165$ $(°C)^{-1}$, and $S_0 = 35$ is the base salinity of seawater in parts per thousand. T is in °C, and S is the salinity in parts per thousand. For example, if we

assume black smoker fluids with a salinity of 70 parts per thousand ($S = 70$) at 360°C, this gives a pore fluid conductivity of 60 S/m, a third higher than the value of 39 S/m which is calculated from Equation 1.2 without regard to salinity.

1.4 Marine Controlled-Source EM Methods

Recent interest in the evaluation of marine resources has stimulated research into electrical surveying methods sensitive to seafloor conductivity. As most features of engineering and economic interest as well as many of scientific significance are found in the upper few hundred meters of the oceanic crust, the impetus towards techniques capable of resolving structures in this range is particularly strong. Marine magnetotelluric measurements are insensitive to features at depths of less than about 30 km, as the presence of an overlaying layer of conductive seawater limits the bandwidth of natural source fields on the seafloor. In the usual case of a resistive seafloor, conventional resistivity methods are insensitive to basement conductivity as current flows between source and receiver primarily through the seawater. Controlled-source methods are therefore being developed to fulfill this function.

These methods use time-varying electric or magnetic dipole sources to induce currents in the crust. Sources are stationed on or near the seafloor to avoid the bandwidth-limiting effects of seawater. Signals recorded at an electric or magnetic field receiver stationed some distance away bear the imprint of the conductivity structure through which they have traveled. The essential characteristics of this structure may therefore be recovered by fitting the signal with appropriate models. To first order, the depth of investigation is determined by the source-receiver separation. The maximum depth of investigation that can be achieved depends on the source dipole moment, the electromagnetic skin depth of the signal in the crustal rocks, and ambient and instrumental noise levels in the signal bandwidth. As natural noise levels at frequencies above 0.05 Hz on the seafloor beneath several kilometers of ocean are much lower than would be observed on land (Chave, 1988), very weak source signals can be detected at considerable range. Measurements at transmitter-receiver separations of up to 65 km have been achieved (Cox *et al.*, 1986). sensitive to structure at depths of up to 30-40 km in the sea-bed. Controlled-source and magnetotelluric methods therefore complement each other neatly in their respective depths of investigation.

Controlled-source methods were initially developed in the frequency domain. There are

four possible source types that can be used: vertical and horizontal electric dipoles, consisting of insulated, current carrying wire with bared ends, and vertical and horizontal magnetic dipoles, consisting of closed loops of insulated, current carrying wire. The theory of the frequency responses of the various source-receiver permutations is described by Bannister (1968), Coggon and Morrison (1970), Edwards, Law and DeLaurier (1981), Chave and Cox (1982), and Kaufman and Keller (1983). Their results may be generalized through the approach of Chave and Cox, by comparison of the modal components of the inductive equations of the various source types in a one-dimensional Earth. The vertical magnetic dipole generates only a poloidal current mode, consisting of horizontal current systems circulating about a vertical axis. The vertical electric dipole generates only a toroidal current mode, consisting of currents flowing in loops about a circular horizontal axis. The horizontal electric and coaxial magnetic dipoles produce both poloidal and toroidal current modes, and are therefore preferable as general purpose mapping tools.

A few experimental frequency domain systems have been developed. Vertical electric dipole systems with horizontal magnetic field receivers were developed at the University of Toronto and have been used for measuring sediment thicknesses (Nobes, 1984; Edwards *et al.*, 1985), for deep crustal soundings (Nobes *et al.*, 1986), for mapping sulfide deposits (Wolfgram, 1985; Wolfgram *et al.*, 1986; Nobes *et al.*, 1992), and for mapping permafrost zones (Edwards *et al.*, 1988). A horizontal electric dipole-dipole system transmitting frequencies in the range 0.25 Hz to 2.25 Hz has been developed at Scripps Institution of Oceanography and used for deep crustal soundings (Young and Cox, 1981; Webb *et al.*, 1985; Cox *et al.*, 1986). A similar system has been developed at Cambridge University and used in experiments on the East Pacific Rise (Evans *et al.*, 1991; 1994; Unsworth, 1994).

The rationale for broadband time-domain measurements was set forth by Edwards and Chave (1986), who demonstrated that the shape of the step response of the in-line electric dipole-dipole system is diagnostic of seafloor conductivity. The transient responses of other systems were investigated by Cheesman, Edwards and Chave (1987), who identified one other configuration suitable as a general purpose surveying tool: the coaxial magnetic dipole-dipole. The transient responses of these systems are characterized by two arrivals separated in time. As the time of electrical diffusion through a medium is directly proportional to the conductivity of the medium, the first arrival is caused by that part of the signal which has traveled through the more resistive of the adjoining half-spaces, generally the seafloor. The signal which travels through the more conductive of the adjoining half-spaces arrives later. The position in time of the earlier arrival is

therefore a direct measure of the seafloor conductivity. Interpretation is based on the shape of the transient response, rather than on absolute amplitude. As the shape is a function of a volume of material, it is influenced to a lesser extent by topographic effects than are measurements which depend on amplitude in their interpretation, such as resistivity or frequency domain amplitude measurements. Furthermore, travel time is proportional to the square of the transmitter-receiver separation, while amplitude is proportional to its inverse cube. Travel-time measurements are therefore less sensitive to errors in transmitter-receiver separation than are amplitude-based measurements, a significant advantage in view of the severe difficulties of seafloor positioning in a rugged ridge environment.

A prototype transient electric dipole-dipole system developed at the University of Toronto was tested in the Strait of Georgia, British Columbia (Everett *et al.*, 1988). The system used a land-based transmitter with electrodes extended into the water, and towed receiver electrodes. The recorded signal was amplified on the seafloor and then transmitted to the ship where digitization took place. While initial results were promising, this approach was not pursued following damage to the equipment. A towed version of the coaxial magnetic dipole-dipole system has been developed at the University of Toronto and the Pacific Geoscience Center for mapping sediment thicknesses and porosities in shallow water (Cheesman, 1989; Cheesman *et al.*, 1990; 1991; 1993). This system is now capable of real-time mapping of near surface conductivity, and has been used commercially. A deep-water version has been developed jointly with Scripps Institution of Oceanography and used in an experiment to correlate sediment conductivity and heat flow (Webb *et al.*, 1993; Webb and Edwards, 1995).

The transient electric dipole-dipole system described in Chapter 4 is the first of its kind developed for short-baseline applications. It works on the same principles as the system described by Everett *et al.* (1988), but the instruments operate autonomously on the seafloor and are suitable for small-scale submersible-based surveys.

1.5 Outline of Thesis

The thesis is organized linearly as an experimental report. Chapter 2 describes the survey target. The tectonic setting, regional geology, morphology and mineralogy of the TAG active hydrothermal mound are reviewed, and results of other geophysical surveys at TAG are briefly summarized.

The theory underlying transient electric dipole-dipole measurements of seafloor conductivities is reviewed in Chapter 3. Results of sensitivity analysis for the two fundamental configurations of electric dipole-dipole measurements over a range of seafloor conductivities are also described, and effects of three-dimensional regions of anomalous conductivity on transient response are qualitatively examined.

The instruments developed for the survey represent the single most valuable contribution of this thesis. These are accordingly described in some detail in Chapter 4. The description is aimed at a level such that an experimentalist familiar with electronics and interfacing could reproduce the basic functionality of the instruments, if not every detail of their design.

In Chapter 5 the TAG survey itself is described, starting with parameter selection, proceeding to pre-dive instrument tests, and then giving an account of the survey dive. Discussion of data reduction including problems of navigation, the rationale for rejection of certain measurements, and data decimation follows.

Interpretation of the data is described in Chapter 6. Modeling methodology is outlined and the results are discussed in the context of mound geology.

Some general conclusions from the TAG survey are summarized in Chapter 7, in which brief descriptions are also given of more recent experiments. Conclusions from these are included in Chapter 7 due to their relevance for future surveys. Finally, the original contributions of the thesis are summarized and a few suggestions are made for future work.

The Appendices contain supplementary material. The chopper amplifiers which were used in the TAG survey and have now been discarded are described for the sake of completeness in Appendix A. Data collected with the more recent version of the amplifiers is provided for comparison in Appendix B. Results of the data reduction are given in Appendix C. Model responses of the best-fitting uniform seafloor models are plotted against the data in Appendix D, while those for the best-fitting layer over a half-space models are plotted against the data in Appendix E. The software which runs the TEM instruments is included in Appendix F.

Chapter 2

The TAG Hydrothermal Mound

2.1 Introduction

The active mound in the Trans-Atlantic Geotraverse (TAG) hydrothermal field was the first high-temperature venting site discovered on a slow-spreading ridge segment. The hydrothermal field was found in 1972 when low-temperature springs were detected through conductivity-temperature-depth profiles (Rona, 1973; Rona *et al.*, 1975). The active mound was not discovered until over a decade later, using a deep-towed instrument sled which measured near-bottom temperatures and recorded images of the seafloor (Rona *et al.*, 1986). Containing an estimated 4 million tones of massive sulfides above the seafloor, this mound is one of the largest known, comparable in size to the average Cyprus deposit of 3 million tones (Humphris *et al.*, 1995).

The good weather and calm seas prevalent in the vicinity of TAG make it a favorable site for data collection in limited time. Despite its considerable distance from land, the TAG mound has consequently become one of the most studied seafloor mineral deposits in the world. In 1993 it was selected as a target for ODP drilling, and an extensive multinational research program was organized leading up to and following this event, of which the survey described in Chapter 5 was a part. For a detailed review of the state of knowledge of the TAG mound prior to 1993, the reader is referred to Rona (1993). Subsequent studies are compiled in *Geophysical Research Letters*, Volume 23, Number 23, 1996.

2.2 Tectonic Setting

The TAG hydrothermal field is located on a 40 km long segment of the Mid-Atlantic Ridge, bounded by non-transform discontinuities to the north at 26°17′ N and to the south at 25°55′ N (Sempere *et al.*, 1990). Seafloor spreading on this segment is asymmetric, with half spreading rates of 13 mm/yr to the east and 11 mm/yr to the west over the last 10^7 years. (McGregor *et al.*, 1977). The ridge morphology of the TAG segment exhibits the deep rift valley and discontinuous neovolcanic zone which characterize slow-spreading ridges (Macdonald, 1982). Discontinuities and asymmetry in the structural morphology and age distribution across the valley suggest that the spreading axis jumped by up to 10 km westward within the past ten million years (Figure 2.1). As a result, the relict neovolcanic zone in which the TAG mound is located is currently being rafted eastward and undergoing fracturing and faulting (Kleinrock and Humphris, 1996). Near the middle of the segment the east wall, rising 2000 m from a depth of nearly 4000 m through a series of steps formed by fault blocks, forms a broad salient that reduces the width of the valley floor from about 9 to 6 km.

At the base of this salient lies the TAG hydrothermal field, covering an area of at least 5 × 5 km of the valley floor and the base of the eastern valley wall (Figure 2.2). The field includes three main areas of past and present hydrothermal activity: (1) a zone of low-temperature venting on the eastern wall between water depths of 2300 m and 3100 m; (2) two former high-temperature vent areas known as the Mir zone and the Alvin zone containing several relict sulfide mounds on the lower east wall between water depths of 3400 and 3600 m; and (3) an actively venting high-temperature sulfide mound at the juncture between the rift-valley floor and the east wall at a water depth of 3670 m (Rona *et al.*, 1993). It is this actively venting mound which is the subject of our study.

2.3 The Active Mound

The active TAG mound is located at 26°08′ N, 44°49′ W, 3.7 km downslope to the west of the low-temperature field described above, 1.5-2 km to the east of the bathymetric axis of the rift valley, on oceanic crust estimated to be 100,000 years old from present seafloor-spreading rates (Rona *et al.*, 1993). The deposit partially overlaps with the north-west margin of a volcanic dome of fractured pillow lavas, and occurs at the intersection of axis-parallel normal faults and an axis-transverse transfer fault (Karson and Rona, 1990).

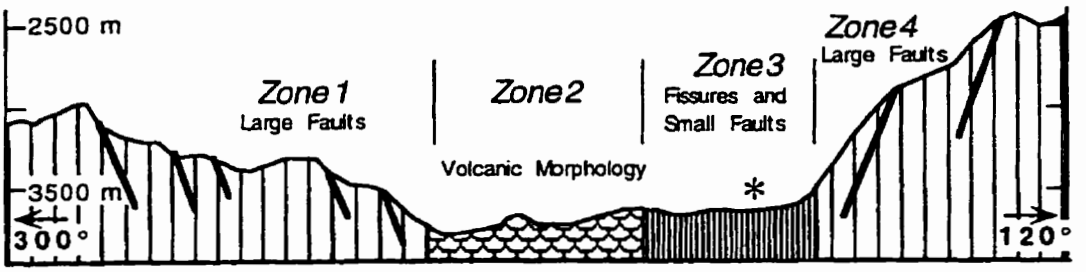

Figure 2.1: NW-SE (300° – 120°) cross-section of the Mid-Atlantic Ridge rift valley near the TAG active mound (*). Vertical exaggeration is 3x (Kleinrock and Humphris, 1996).

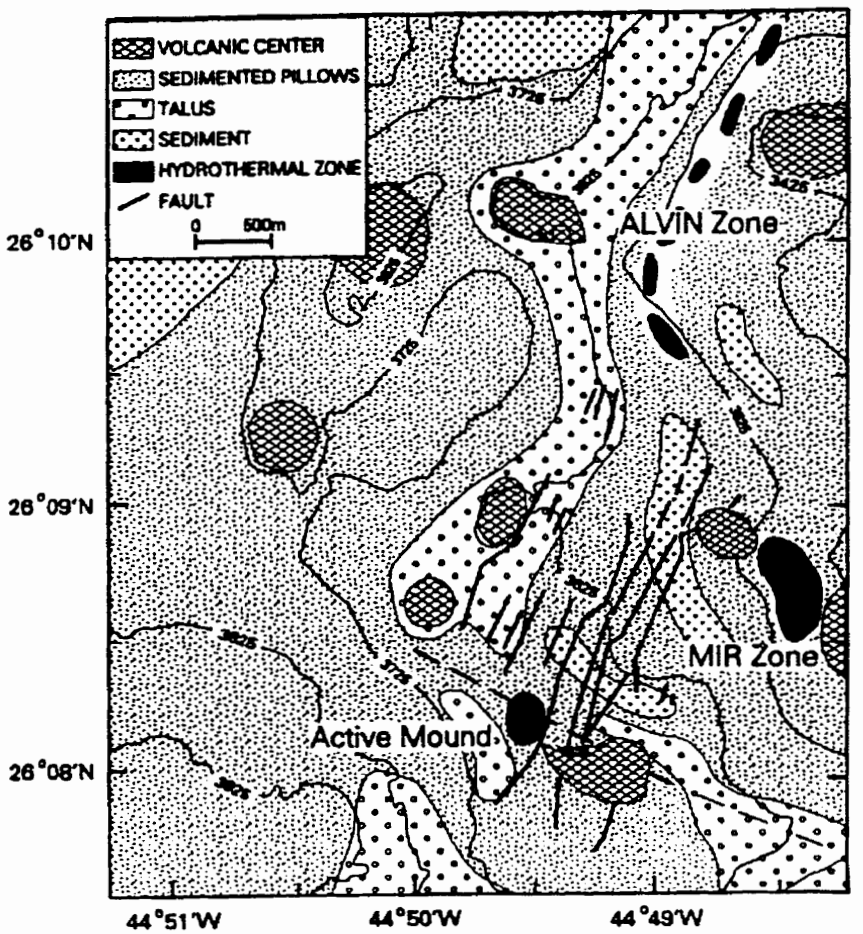

Figure 2.2: Geologic map of the TAG hydrothermal field (Rona *et al.*, 1993).

Carbonate and metalliferous sulfide-oxide sediments surround the mound, extending up to 100 m from its base. Radiometric dating of samples recovered by dredging and from submersible sampling suggest that the mound is approximately 40,000-50,000 years old. Activity has been intermittent over the past 20,000 years with a periodicity of 5000-6000 years, and the present constructional phase began about 50 years ago after a dormancy of about 5000 years (Lalou *et al.*, 1990; 1993).

Episodic activity is reflected in the morphology of the mound (Humphris and Kleinrock, 1996), which consists of two discrete, circular platforms, with one of smaller diameter asymmetrically superposed in the NNW portion of a broader, flatter platform (Figure 2.3). The top of the lower platform is $\sim$ 150 m in diameter, at depths of 3650-3655 m. That of the upper platform is $\sim$ 90 m in diameter, at depths of 3642-3650 m. On the northern side, walls of the two platforms combine to form a steep scarp rising 50 m at $\sim$ 45°. On the southern side, a 5 m scarp wall marks the transition from upper to lower platform, and the lower platform slopes gently to surrounding sediment covered pillow basalt.

The surface of the mound itself is composed primarily of massive sulfides with anhydrite frequently visible. High temperature (363°C) fluids vent from a cluster of chalcopyrite-anhydrite-rich black smoker chimneys, collectively known as the Black Smoker Complex (BSC), in the northwest quadrant of the mound. The BSC sits on top of a 15 m high, 30 m diameter cone, the surface of which is covered by a 3-6 cm thick plate-like layer of massive chalcopyrite and marcasite, with interspersed blocks of corroded massive anhydrite. Analysis of samples collected from this crust suggests that it is formed from fluid ponded beneath the conical edifice, presumably in a high-porosity, cavern-like space beneath the black smokers (Tivey *et al.*, 1995).

A complex of white smokers venting fluids from 260°C to 300°C is located in the southeast quadrant of the mound, which is known as the Kremlin area from the bulbous shape of its 1-2 m high chimneys. Sphalerite is the major chimney constituent, while minor amounts of chalcopyrite, pyrite, and amorphous silica are present. Chemical analysis suggests that white smoker fluids are derived from black smoker fluids by a combination of conductive cooling, mixing with entrained seawater, and precipitation of sulfides within the mound. These reactions cause dissolution of sphalerite within the mound and an order of magnitude enrichment of zinc in white-smoker fluids compared with black smoker fluids (Tivey *et al.*, 1995).

Conductive heat flow over the mound varies by over four orders of magnitude about a

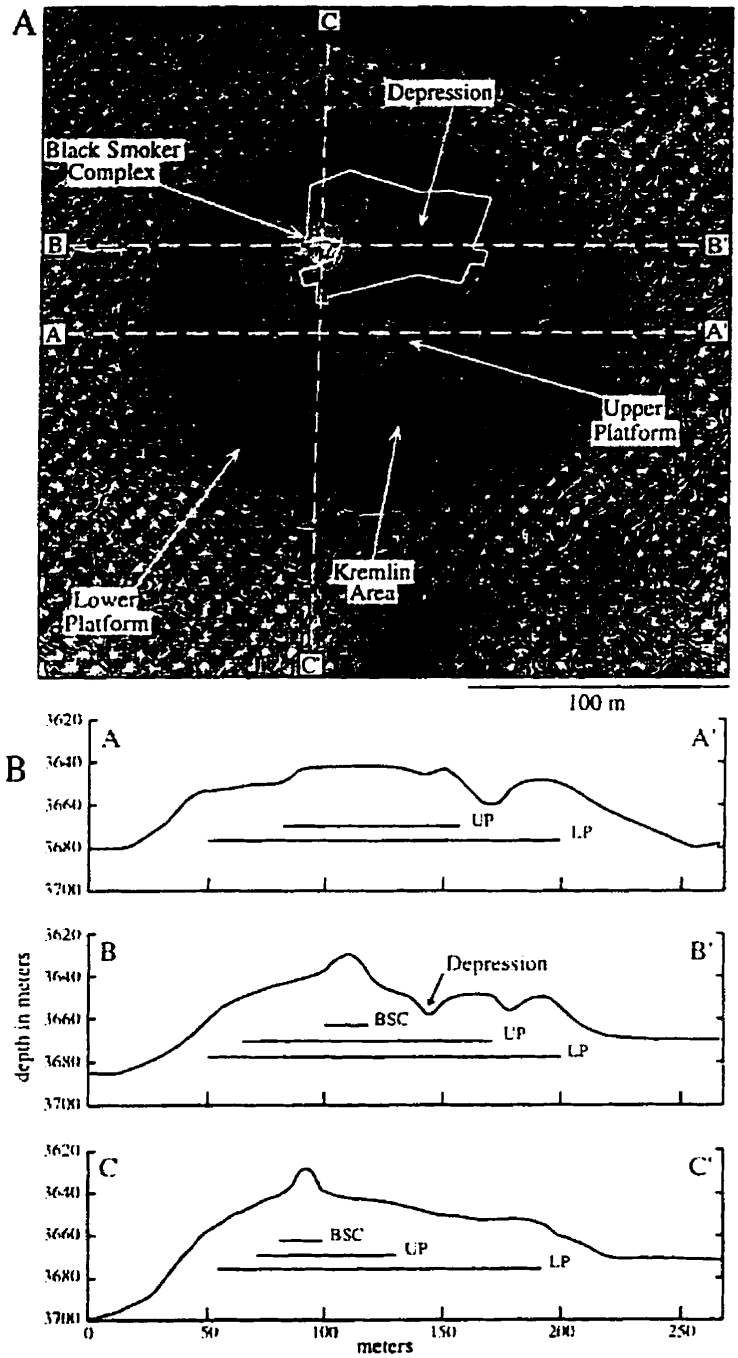

Figure 2.3: Bathymetry of the active mound, from Humphris and Kleinrock (1993).

mean of 7.5 Wm^{-2} (Becker *et al.*, 1996). Within 20 m of the BSC, heat flows are extremely variable (0.1 to >100 Wm^{-2}), suggesting structural heterogeneity and possibly temporal variability of local flow patterns. Heat flow in the Kremlin area is also quite variable (0.2 to 25 Wm^{-2}). High heat flows of 3.7 to >25 Wm^{-2} were measured on the sedimented terraces that slope down from the Kremlin area on the south and southeast side of the mound, implying an extension of sub-surface flow processes beyond the seafloor expression of the sulfide mound. The western portion of the mound is characterized by a belt of very low heat flow (< 0.02 Wm^{-2}) 20 to 50 m west of the BSC, which is interpreted as indicating a region of local entrainment of seawater.

Near-bottom magnetic data shows a distinct zone of reduced magnetization directly beneath the active mound, which is attributed to the highly altered upflow zone of the vent system. The low magnetization zone extends to the south of the mound, indicating a possible dip of the piping system in this direction (Tivey *et al.*, 1993).

A submersible-based gravity transect of the mound was made by Evans (1996). His modeling of the data suggests a bulk sulfide density of $\sim$ 3650 kg m^{-3} against a basaltic seafloor density of $\sim$ 2400 kg m^{-3}. Pyrite and chalcopyrite, which are the dominant sulfides, have densities of 4000 to 5000 kg m^{-3}, from which Evans estimates a mound bulk porosity of $\sim$ 24%. However this estimate does not take into account the presence of low-density pore-filling anhydrite. In Evans' model the mound is draped over the edge of a scarp in the basalt substrate, with sulfide thickness largest ($\sim$ 50 m) on the northern side of the mound, and decreasing sharply to the south to a steady value of about 10 m just south of the Kremlin area.

Resistivity measurements conducted by Von Herzen *et al.* (1996) gave apparent conductivities of the mound sulfides at shallow depth ($\sim$ 10 m) of 4.8 to 5.6 S/m, and of the nearby pillow basalts of 0.42 to 0.48 S/m. From these values, they estimate sulfide porosities of 25 to 45% depending on the value selected for the cementation factor in Archie's Law. As the variation of pore fluid conductivity with temperature is not taken into account in their calculation, however, the validity of this result is questionable.

Knowledge of the internal structure of the mound derives primarily from the 1994 ODP drilling (Humphris *et al.*, 1995). Despite low core recovery of $\sim$ 12%, the results provide valuable windows into the structural zonation within the mound. Breccias of various types dominate all the drill sections, supporting a model of mound growth through chimney collapse and cementation developed from analysis of land-based deposits. Abundant anhydrite was encountered in the north-east quadrant of the mound between depths of

$\sim$ 15 m below seafloor and 45 m below seafloor, indicating high temperatures of $> 150°C$ within the mound, and significant entrainment of cold seawater. The stratigraphy inferred from their results along with the drill station locations are shown in Figure 2.4.

(a)

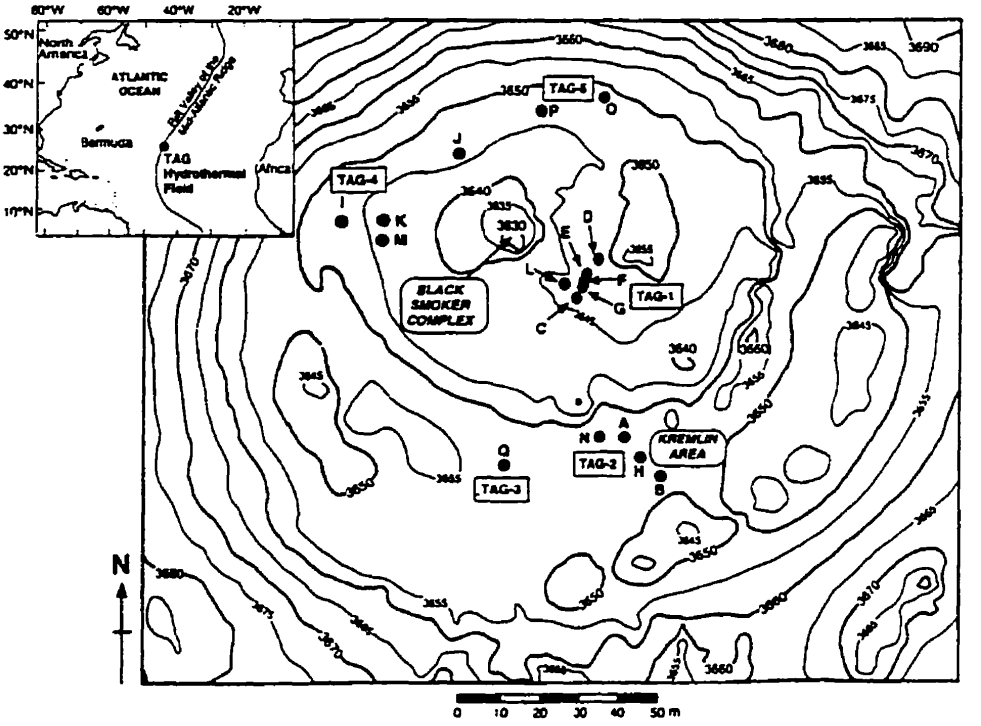

(b)

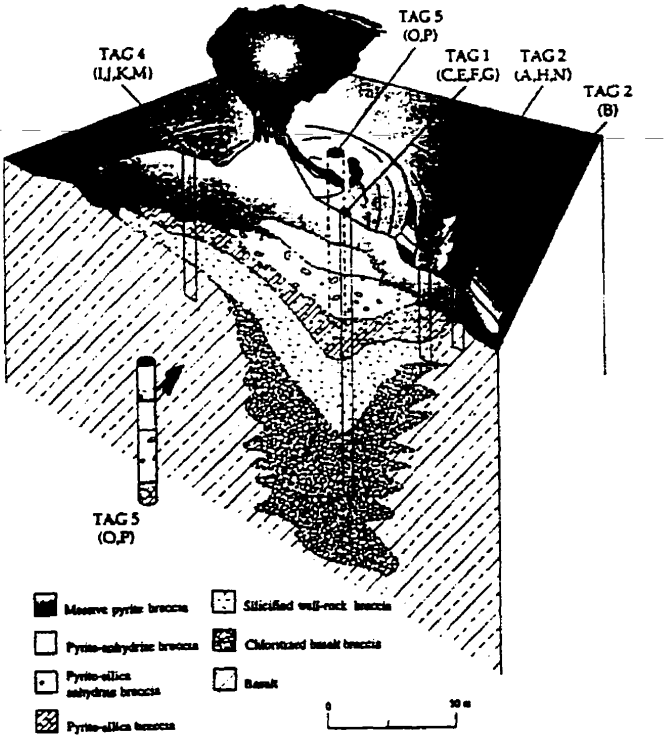

Figure 2.4: ODP drill results (Humphris *et al.*, 1995). (a) Location of drill holes on the TAG mound. (b) Composite of structure with depth inferred from drill cores.

Chapter 3

Theory

3.1 Introduction

The theory for the response of a one-dimensional layered seafloor to excitation by a time-varying electric dipole source is well developed. Sommerfeld (1926) derived expressions for the fields of an infinitesimal electric dipole energized by a harmonic current on the surface of a homogeneous Earth. Riordan and Sunde (1933) extended Sommerfeld's result to the case of a two-layered Earth. Bannister (1968) calculated the fields of an infinitely long harmonic horizontal electric dipole located within the upper layer, representing seawater, of a two-layer conducting Earth. Chave and Cox (1982) derived expressions for both vertical and horizontal harmonic current sources in a conductive ocean overlaying a layered one-dimensional Earth. Edwards and Chave (1986) calculated the response of a homogeneous seafloor to excitation by a transient horizontal electric dipole source. Cheesman *et al.* (1987) and Cheesman (1989) calculated the transient response of a layered laterally isotropic seafloor. Yu and Edwards (1992a; 1992b) incorporated the effects of lateral anisotropy within layers, and Yu (1994) developed an algorithm to compute the transient response of a tri-axially anisotropic layered seafloor.

The EM fields in a 1-D conductivity structure for an arbitrary source are most clearly described in modal form, in which the diffusion equations are separated into independent poloidal and toroidal magnetic (PM and TM) modes about the vertical axis. This presentation is useful as the characteristics of the two modes are quite different with regard to both their sensitivity to electrical structure and their behavior with a time-varying source. The PM mode is characterized by horizontal current systems, having no vertical electric field component. Its inductive nature makes it relatively insensitive

to intermediate horizontal resistive layers. The TM mode is characterized by currents flowing in loops about a circular horizontal axis, and contains no vertical magnetic field component. The presence of vertical currents in the TM mode makes it sensitive to both resistive and conductive intermediate layers. Chave (1984) examined the Fréchet kernels of a horizontal electric dipole on the seafloor, concluding that the TM mode possesses superior resolution ability, especially for low relative conductivity contrasts at depth. In the zero frequency limit, which corresponds to late time if the source is a step function in time domain, the TM mode equations reduce to those of a DC resistivity array, while the PM mode vanishes.

The formulation given below follows Cheesman (1989) and Edwards (1997). As propagation of electromagnetic fields through conductive seawater and rocks is primarily diffusive, the magnetic effects of displacement currents within the earth are neglected. Expressions are given for the two fundamental geometries of the horizontal electric dipole-dipole system: the in-line and the broadside configurations. All other possible geometries may be expressed as linear combinations of these two.

3.2 The Transient HED Response of a Layered Seafloor

We define a model of an N layered seafloor covered by a sea of finite thickness. The seafloor layers are described by thicknesses $d_1, d_2, ..., d_{N-1}$ and conductivities $\sigma_1, \sigma_2, ..., \sigma_N$ respectively. The sea layer is assigned an electrical conductivity σ_0 and a depth d_0. The magnetic permeability is assigned its free space value μ_0 everywhere. The transmitter and receiver are placed on the seafloor, separated by a distance ρ.

Assuming zero initial conditions, the Laplace transform $E(s)$ of the electric field at the receiver may be expressed as

$$E(s) = \frac{j(s)}{2\pi} \left[F(s) + G(s) \right], \tag{3.1}$$

where s is the Laplace variable, $j(s)$ is the Laplace transform of the source current dipole moment and the functions F and G are the Hankel transforms of the toroidal and poloidal modes respectively. If the source is a current I which is switched on at time $t = 0$ and held constant in a transmitting electric dipole of length Δl, the source term in Laplace space is

$$j(s) = \frac{I\Delta l}{s}. \tag{3.2}$$

The definitions of F and G depend on the transmitter-receiver geometry. For the in-line configuration, the Hankel transforms are defined as

$$F(s) = -\int_0^\infty \frac{Y_0 Y_1}{Y_0 + Y_1} \lambda J_1'(\lambda\rho)\, d\lambda, \tag{3.3}$$

and

$$G(s) = -(s/\rho)\int_0^\infty \frac{Q_0 Q_1}{Q_0 + Q_1} J_1(\lambda\rho)\, d\lambda, \tag{3.4}$$

where J_1 is a Bessel function and λ is wavelength. The corresponding forms for the broadside electric dipole-dipole configuration are

$$F(s) = (1/\rho)\int_0^\infty \frac{Y_0 Y_1}{Y_0 + Y_1} J_1(\lambda\rho)\, d\lambda, \tag{3.5}$$

and

$$G(s) = s\int_0^\infty \frac{Q_0 Q_1}{Q_0 + Q_1} \lambda J_1'(\lambda\rho)\, d\lambda. \tag{3.6}$$

The coefficients Y_0, Y_1, Q_0 and Q_1 are the impedances and inductances for the material above and below the plane of the electric dipole-dipole system. The coefficients Y_0 and Q_0 of the sea layer and air above it are given by

$$Y_0 = \frac{\theta_0}{\sigma_0}\left[\frac{\sigma_0 u_a + s\epsilon_0\theta_0 \tanh(\theta_0 d_0)}{s\epsilon_0\theta_0 + \sigma_0 u_a \tanh(\theta_0 d_0)}\right]. \tag{3.7}$$

and

$$Q_0 = \frac{\mu_0}{\theta_0}\left[\frac{\theta_0 + u_a \tanh(\theta_0 d_0)}{u_a + \theta_0 \tanh(\theta_0 d_0)}\right]. \tag{3.8}$$

where $\theta_0^2 = \lambda^2 + s\mu\sigma_0$ is the electromagnetic wavenumber in the sea water, and $u_a^2 \approx \lambda^2$ is the electromagnetic wavenumber in the air.

The parameters Y_1 and Q_1 represent the seafloor contributions to the toroidal and poloidal modes respectively. For a layered earth model, these are evaluated by the following recursive relationships:

$$Y_i = \frac{\theta_i}{\sigma_i}\left[\frac{\sigma_i Y_{i+1} + \theta_i \tanh(\theta_i d_i)}{\theta_i + \sigma_i Y_{i+1}\tanh(\theta_i d_i)}\right], \tag{3.9}$$

and

$$Q_i = \frac{\mu_0}{\theta_i}\left[\frac{\theta_i Q_{i+1} + \mu_0 \tanh(\theta_i d_i)}{\mu_0 + \theta_i Q_{i+1}\tanh(\theta_i d_i)}\right]. \tag{3.10}$$

The wavenumbers θ_i are defined by $\theta_i^2 = \lambda^2 + s\mu\sigma_i$. The recursion proceeds upwards from the basement half-space, for which $Y_N = \theta_N/\sigma_N$ and $Q_N = \mu_0/\theta_N$.

The Hankel transforms in the above equations may be inverted numerically using the quadrature integration with continued Padé fraction expansion algorithm described by Chave (1983). The Laplace transforms are inverted within the kernel computations of the Hankel transform using the Gaver-Stehfest algorithm, described by Stehfest (1970), Knight and Raiche (1982), Villinger (1984), and Edwards and Cheesman (1987). While comparison by Davis and Martin (1979) of a number of different methods for numerically inverting the Laplace transform revealed that the Gaver-Stehfest algorithm is neither the most accurate nor the most generally applicable, this method offers compensatory advantages of speed and simplicity due to the need to compute the transform function only for real values of the Laplace variable. The method is applicable only to temporal functions that are smooth, continuous, and have no rapid oscillations. That these conditions are satisfied in the above equations is guaranteed by the diffusive nature of the electromagnetic field propagation. The Gaver-Stehfest algorithm approximates the temporal function $f(t)$ with $f_a(t)$ using the following relationship:

$$f_a(t) = (\log_e 2)/t \sum_{n=1}^{N_c} c_n F(s_n), \tag{3.11}$$

where N_c is even. The N_c discrete values of s are given by $s_n = n(\log_e 2)/t$. The coefficients c_n are determined as

$$c_n = (-1)^{n+N_c/2} \sum_{k=(n+1)/2}^{\min(n,N_c/2)} \frac{k^{n/2}(2k)!}{(N_c/2-k)!\,k!\,(k-1)!\,(n-k)!\,(2k-n)!}. \tag{3.12}$$

The optimal value for the number N_c varies with machine precision. With increasing N_c, the accuracy of F_a first increases linearly then decreases linearly. (Edwards and

Cheesman (1987) found that on an IBM-PC running Microsoft FORTRAN 3.1 in single precision mode the optimal N_c was about 8. Yu (1994) found that on the Sun SPARC station running SUN FORTRAN in double precision mode the optimal N_c is about 12.)

3.3 The Double Half-Space Model

In certain cases, the above expressions may be simplified. If the thickness of the sea layer is large compared to the transmitter-receiver separation, the terms Y_0 and Q_0 simplify to $Y_0 = \theta_0/\sigma_0$ and $Q_0 = \mu_0/\theta_0$. If the sea-bed can be assumed to be homogeneous on the scale of the transmitter-receiver separation, then the above expressions for Y_1 and Q_1 simplify to $Y_1 = \theta_1/\sigma_1$ and $Q_1 = \mu_0/\theta_1$. The combination of these assumptions gives the double half-space model, which is a reasonable approximation for many real situations, and is useful for illustrating the fundamental characteristics of the transient response.

For this model the integrals for the poloidal mode vanish in the late-time static limit. Rewriting the toroidal mode integrals for $s\mu\sigma_0$ and $s\mu\sigma_1$ small compared with λ^2, the in-line field may be evaluated as the inverse Laplace transform of

$$-\frac{I\Delta l}{2\pi s}\int_0^\infty \frac{1}{\sigma_0+\sigma_1}\lambda^2 J_1'(\lambda\rho)\,d\lambda, \tag{3.13}$$

or

$$\frac{I\Delta l}{\pi\sigma_0(1+\sigma_1/\sigma_0)\rho^3}. \tag{3.14}$$

The broadside field is the inverse Laplace transform of

$$\frac{I\Delta l}{2\pi\rho s}\int_0^\infty \frac{1}{\sigma_0+\sigma_1}\lambda J_1(\lambda\rho)\,d\lambda, \tag{3.15}$$

or

$$-\frac{I\Delta l}{2\pi\sigma_0(1+\sigma_1/\sigma_0)\rho^3}. \tag{3.16}$$

The above expressions show that for both configurations in the DC limit, the seafloor contribution to the fields is a function of the ratio of the seafloor conductivity to that of the seawater. While the static fields are sensitive to conductive bodies such as hydrothermal mounds, they are insensitive to the more common case of a resistive seafloor, as current flow between the transmitter and receiver takes place almost entirely through the seawater.

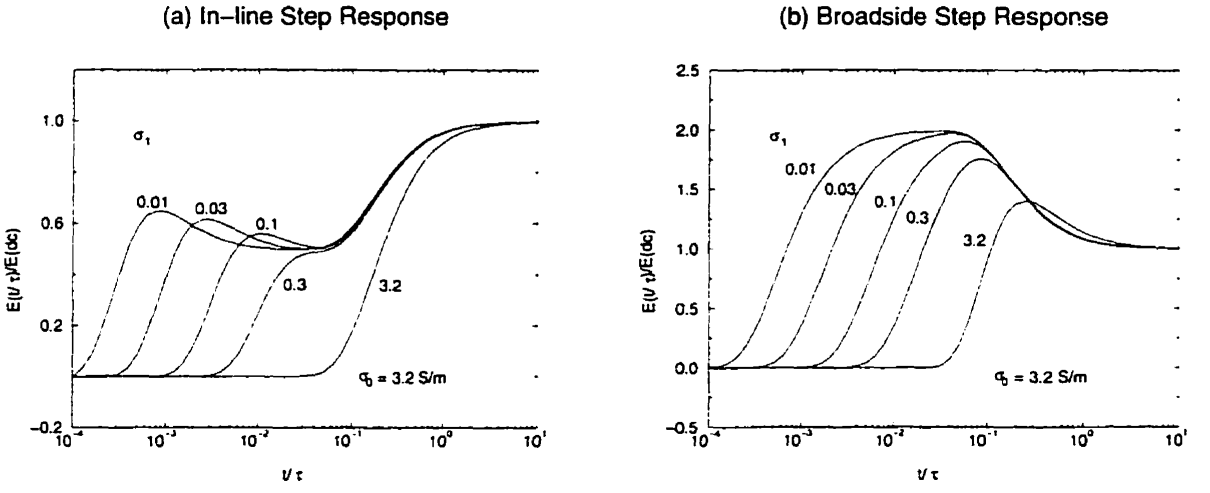

Figure 3.1: The step-on response of (a) the in-line and (b) the broadside configurations for the case of a resistive seafloor. The arrival time is normalized by the seawater diffusion constant $\tau = \mu\sigma_0\rho^2$ and the amplitude is normalized by the late time DC values of the respective array configurations. The seafloor conductivity may be interpreted from the position in time of the first peak in the in-line response, or that at which the field reaches two-thirds of its maximum value for the broadside response.

This is not true of the transient response as a whole. Figure 3.1 shows the step-on response of the double half-space model for the in-line and broadside configurations, plotted for a range of conductivity ratios between the seawater and the seafloor. The in-line response is characterized by two distinct steps which are separated in time by an amount proportional to the conductivity ratio. This results from the superposition of two arrivals corresponding to those parts of the field which have traveled through the seafloor and through the seawater respectively. The fields move diffusively through the two media, and the travel time of each component is directly proportional to the diffusion constant $\tau = \mu_0\sigma_i\rho^2$ of the medium through which it travels. The broadside response rises at early time to a value which asymptotically approaches twice the DC value as the conductivity ratio approaches infinity, then collapses to the late-time DC value. This pattern results from the Maxwell image of the transmitter that forms in the conductive ocean. Despite the overt difference from the in-line response, the initial rise for the broadside configuration also occurs at a time which, for a resistive seafloor, is proportional to the basement diffusion constant. Each configuration thus exhibits a response which is diagnostic of the bulk conductivity of the seafloor along the diffusion path.

Where the conductivity ratio is close to unity, the seafloor and seawater arrivals merge. Interpretation is based on the slope of the response curve (Figure 3.2). In the more

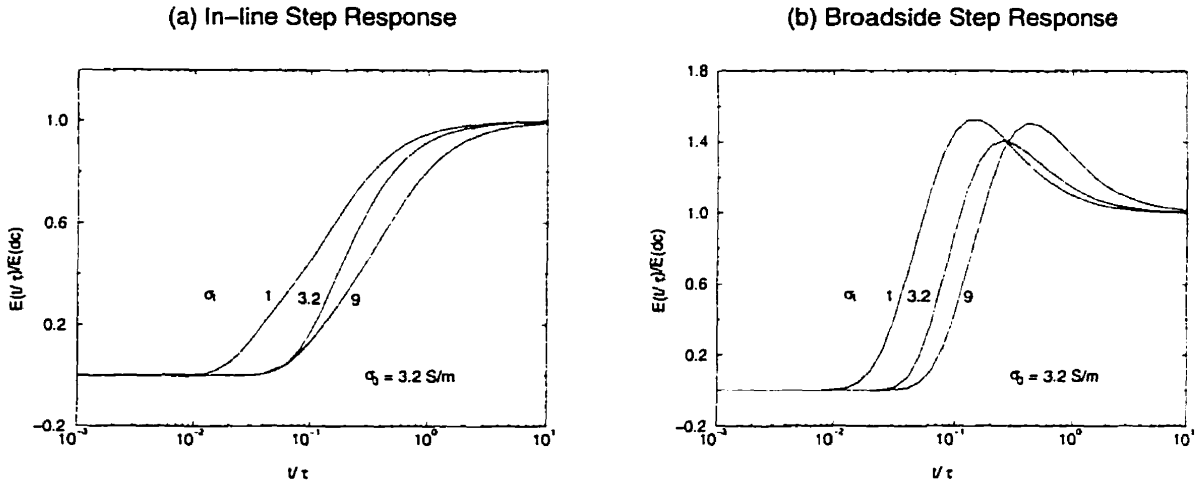

Figure 3.2: The step-on response of (a) the in-line and (b) the broadside configurations for a homogeneous sea-bed with a conductivity close to that of the seawater. The arrival time is normalized by the seawater diffusion constant $\tau = \mu\sigma_0\rho^2$ and the amplitude is normalized by the late time DC values of the respective array configurations. While distinct sea-bed and seawater arrivals are not observed, the seafloor conductivity may be recovered by fitting the arrival curve.

general case where the seafloor and seawater arrivals show distinct separation in time, a robust estimate of the sea-bed conductivity may be recovered directly by inspection of the transient response. In studying the in-line system Everett *et al.* (1988) found an approximate relation between the seafloor conductivity σ_1 and the time t^{il} at which the rate of change of the electric field with respect to log time reached its maximum:

$$t^{il} = \frac{\mu_0\sigma_1\rho^2}{8}. \tag{3.17}$$

This definition, however, cannot be applied to the broadside system due to the fundamentally different nature of its response. Yu (1994) studied both in-line and broadside configurations and found it more convenient to define a parameter which he called t_a. For the in-line system, this corresponds to the time at which the peak due to the seafloor arrival occurs. For the broadside system, it is the time at which the field reaches two-thirds of its maximum value. With this definition, he found that the relationship

$$t_a = \frac{\mu_0\sigma_1\rho^2}{3.2} \tag{3.18}$$

gave consistent values for the seafloor conductivity with either configuration.

The transient response is therefore most sensitive at early time to the more resistive of the adjoining half-spaces, and at late time to the more conductive. If the seafloor is more conductive than the seawater, as is generally true in the case of hydrothermal deposits, the pattern holds with the seafloor component simply becoming the later time response.

3.4 Sensitivity Analysis

A central question of experimental design or data interpretation is what the measurements reveal about the physical system producing them. This question was addressed by Backus and Gilbert (1968), who brought to the problem of non-linear functionals the formalism of the Fréchet kernel. As applied to the transient electric dipole-dipole system, the measured electric field response $E(x,0,t)$ of the Earth-water system to a transient excitation changes when any small change $\delta\sigma$ occurs in the seafloor conductivity $\sigma(z)$ over an interval δz at some depth z. The total change in the electric field is related to systematic small changes in the resistivity at all depths by the integral

$$\delta E(x,0,t) = \int_0^\infty F(log\,\sigma, x, 0, z, t)\delta(log\,\sigma)dz, \tag{3.19}$$

where $\delta(log\,\sigma)$ is the fractional change in conductivity at depth z, and F is the Fréchet kernel. For some situations, the Fréchet kernel may be derived analytically and, plotted as a function of z, is used as a sensitivity function to indicate the penetration depth of a measurement and to gain a qualitative feel for resolution ability under varying model conditions. Examples of analytic solutions for marine controlled electromagnetic sources include Chave (1984) and Edwards and Cheesman (1987).

The sensitivity function may alternatively be obtained numerically following the method of Gomez-Trevino and Edwards (1983). Using this approach, a thin layer of thickness δz is inserted systematically at successive depths z_i in a layered earth model, with its conductivity varied by a small fraction from that of its immediate environment. The sensitivity of the surface measurement as a function of the depth of the layer is then defined as

$$F(log\sigma, x, 0, z, t) = \frac{\delta E(x,0,z,t)}{\delta(log\,\sigma)\delta z}, \tag{3.20}$$

where $\delta E(x,0,z,t)$ is the change in the electric field datum $E(x,0,t)$ in response to the

conductivity perturbation at depth z.

The sensitivity function described above has the units $V.m^{-2}$, but it is convenient to form a dimensionless expression from it. Changes in the electric field can be expressed as a fraction of the late-time DC limit field of the model without the perturbation layer. For a suitable scale length by which to multiply the function, Edwards and Cheesman (1987) argue that the value chosen should be typical of the depth interval over which a conductivity change might be expected to influence the data. As a decrease in absolute resolution is generally anticipated as depth increases, they suggest that the function be scaled by multiplying by the depth z. By the same argument, it is appropriate to make the thickness of the layer of anomalous conductivity a fraction of the depth z rather than a constant value. It should be kept in mind however that this choice of scaling has the effect of enhancing the magnitude of the sensitivity function for large z, but not greatly.

The non-dimensional sensitivity $\times$ depth is therefore defined as

$$\frac{\delta E(x,0,z,t)/E(x,0,\infty)}{\delta(log\,\sigma)\delta(log\,z)}. \tag{3.21}$$

Normalized sensitivity $\times$ depth functions are plotted as a function of depth for the in-line configuration in Figure 3.3 and for the broadside configuration in Figure 3.4. Five percent values are used for the ratios $\delta(log\,\sigma)$ and $\delta(log\,z)$. The functions are plotted for seawater/seafloor conductivity ratios σ_0/σ_1 of 100, 10, 1 and 0.1 with the seawater conductivity σ_0 set to 3.2 S/m, at times corresponding to 0.0375, 0.075, 0.125 and 0.375 $\times\ \mu\sigma_1\rho^2$, the seafloor diffusion constant, as well as for the late-time DC limit. While the results plotted are for the typical transmitter-receiver separation of 100 m, the results may be generalized to arbitrary separation by normalizing depth by transmitter-receiver separation, and normalizing time by the seafloor diffusion constant to give the dimensionless times described above.

These figures illustrate how the characteristics of the transient response change with respect to time for a given seafloor conductivity, and with respect to the seafloor conductivity itself. As time increases, the peak of the sensitivity function for both in-line and broadside configurations moves to greater depth within the half-space. As the conductivity of the seafloor increases, peak sensitivity to a given depth occurs at later time. Both of these effects reflect the diffusive moveout of the electromagnetic fields induced in the half-space, which travel with a diffusion time directly proportional to the seafloor conductivity to excite progressively greater depths in the model.

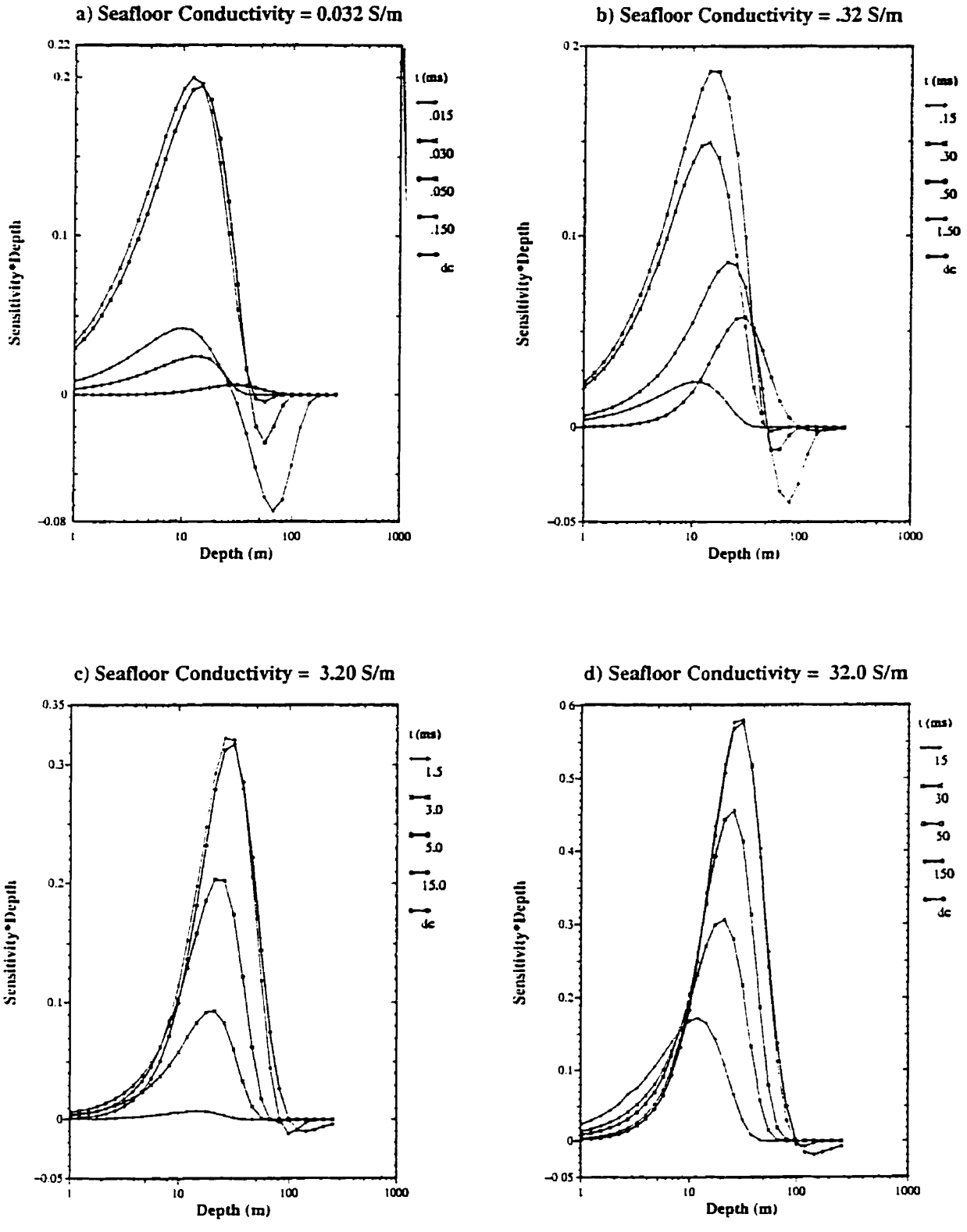

Figure 3.3: Normalized sensitivity × depth for in-line configuration. Plotted at 0.0375, 0.075, 0.125 and 0.375 $\times\tau_1$ for seawater/seafloor conductivity ratios of 100, 10, 1, 0.1. The transmitter-receiver separation is 100 m.

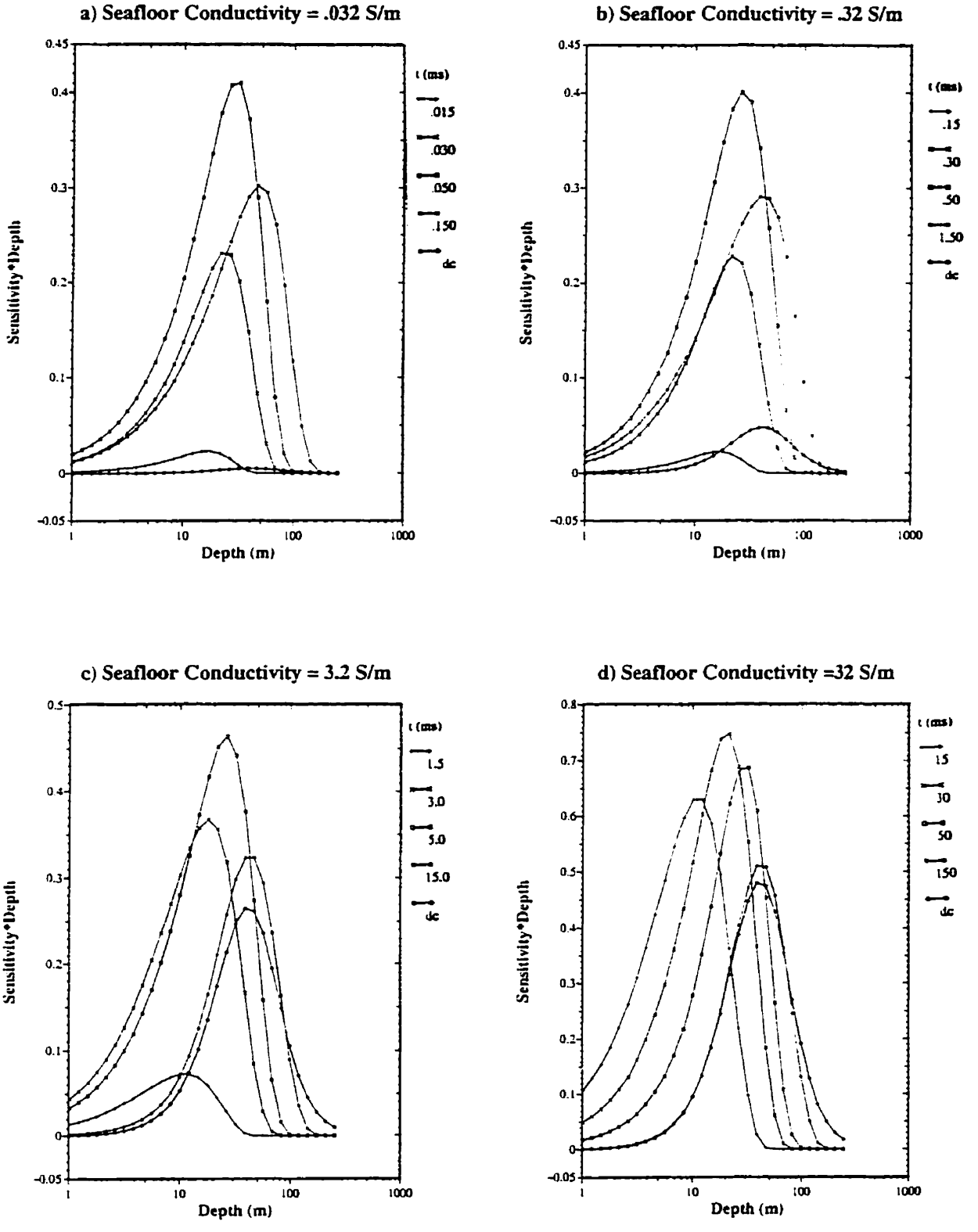

Figure 3.4: Normalized sensitivity × depth for broadside configuration. Plotted at 0.0375, 0.075, 0.125 and 0.375 $\times\tau_1$ for seawater/seafloor conductivity ratios of 100, 10, 1, 0.1. The transmitter-receiver separation is 100 m.

Panel (a) in Figure 3.3 shows that for a resistive seafloor, the sensitivity function is positive at early time, peaking at a depth of about one-fifth of the transmitter-receiver separation. At intermediate time the response function is characterized by a change of sign with depth. The resulting field cancellation at a seafloor receiver accounts for the dip that is observed following the initial rise to half-maximum in the step response. At late time, the EM system is insensitive to a resistive seafloor, as current flows between the transmitter and the receiver almost entirely through the overlaying conductive seawater. In panel (b) of Figure 3.3 it can be seen that as seafloor conductivity increases, the negative excursion of the sensitivity function is reduced, and the DC sensitivity increases. Panel (c) of Figure 3.3 shows the case of a whole space in which the seafloor conductivity is equal to that of the seawater. The sensitivity to structure at all depths increases monotonically with time, reaching its maximum in the DC limit. Panel (d) in Figure 3.3 is the case of a conductive seafloor. The change with time of the sensitivity function is qualitatively similar to that observed in panel (c), but sensitivity is greater at all times.

From Figure 3.4 it can be seen that the characteristics of the broadside sensitivity function are somewhat different. At early as well as late time, sensitivity increases with increasing seafloor conductivity. The sensitivity kernels are generally more closely matched in amplitude at different points in time than those of the in-line configuration, particularly in the case of the conductive seafloor. This suggests that the broadside configuration, which has previously received little attention, may be preferable for sounding a conductive seafloor. The ideal resolving kernel would be a delta function of constant amplitude moving to progressively greater depth with time, allowing a one-to-one correlation of the transient response in time with structure at depth. While such resolving kernels may be obtained from either the in-line or broadside configurations by superposition of the sensitivity functions at various transmitter-receiver separations and times, for individual measurements the resolving kernels of the broadside configuration over a conductive seafloor shown in panel (d) of Figure 3.4 offer the best approximation to this ideal.

An alternative way of parsing this information is shown in Figures 3.5 and 3.6, in which the sensitivity $\times$ depth function is plotted as a function of time for selected depths in the model. Once again, the results have been plotted for a transmitter-receiver separation of 100 m but may be generalized for arbitrary separations by normalizing time by the seafloor diffusion constant, and depth by separation. In Figure 3.5 (a) it is apparent that for the in-line configuration in the case of a resistive seafloor, sensitivity to a given depth shows a narrow peak in time, being positive for shallow structure and negative for deeper structure. As seafloor conductivity increases, slower moveout of the diffusive field and an

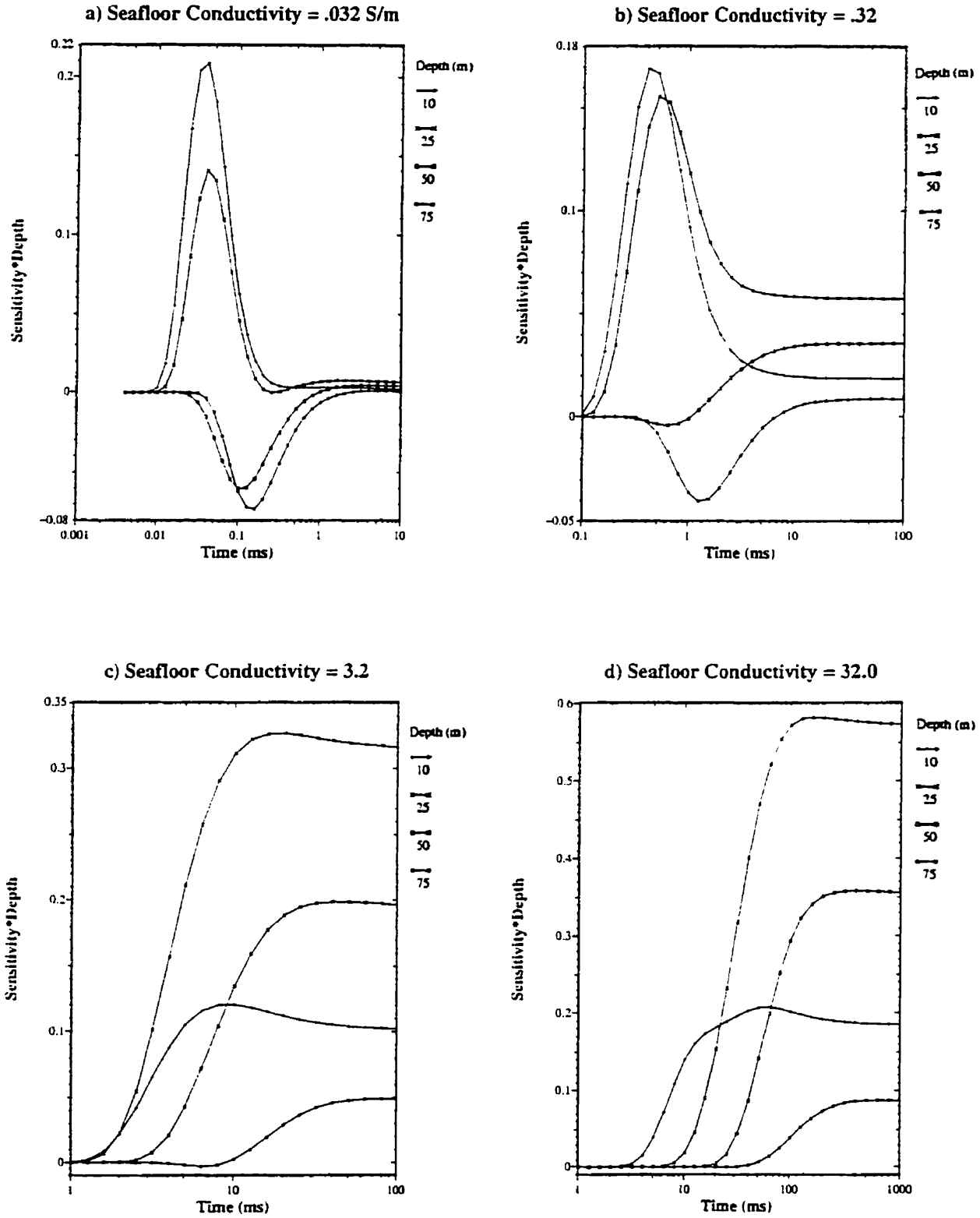

Figure 3.5: Sensitivity × depth vs time at depths of 10, 25, 50 and 75 percent of the transmitter-receiver separation for the in-line configuration with seawater/seafloor conductivity ratios of 100, 10, 1, 0.1. The transmitter-receiver separation is 100 m.

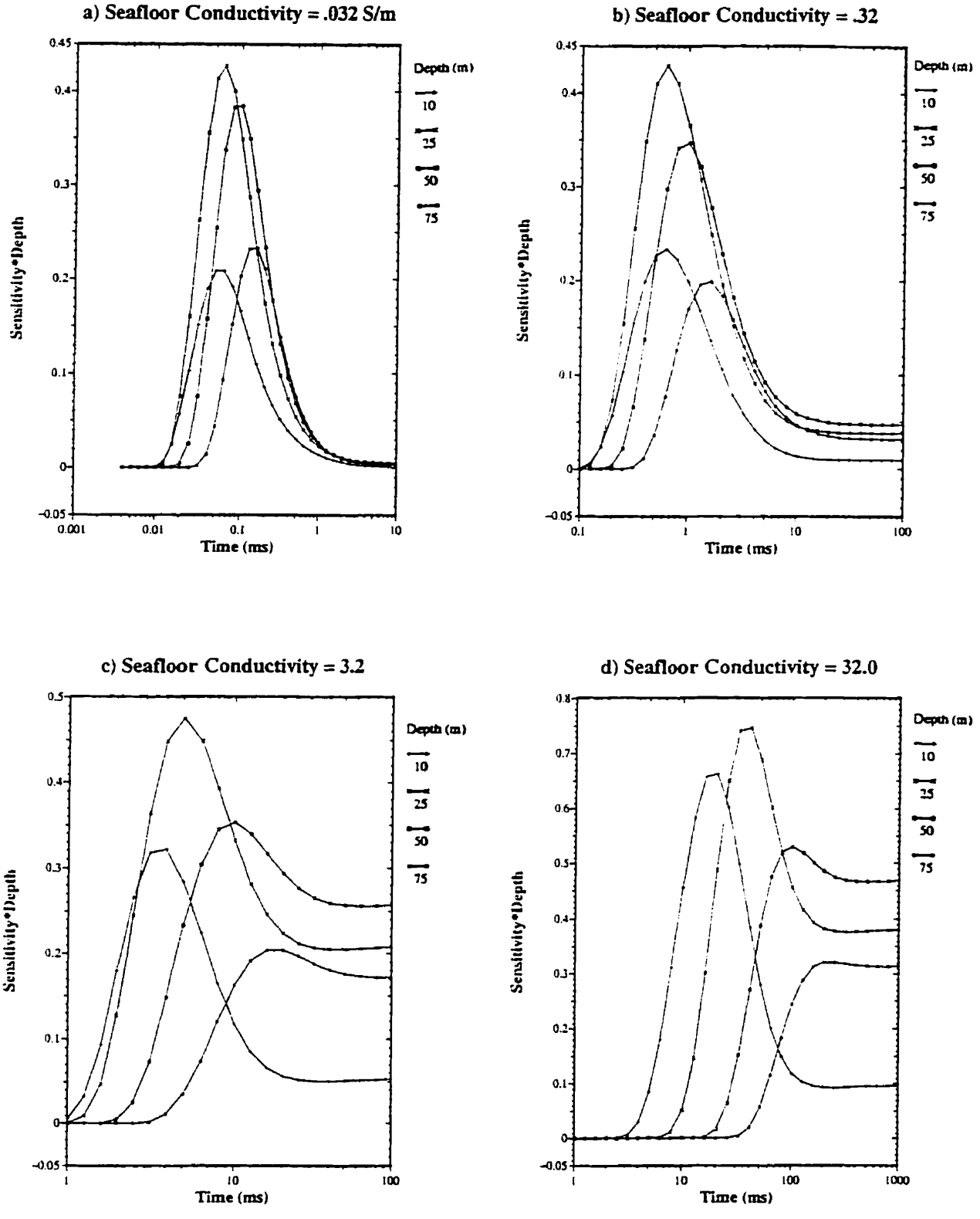

Figure 3.6: Sensitivity × depth vs time at depths of 10, 25, 50 and 75 percent of the transmitter-receiver separation for the broadside configuration with seawater/seafloor conductivity ratios of 100, 10, 1, 0.1. The transmitter-receiver separation is 100 m.

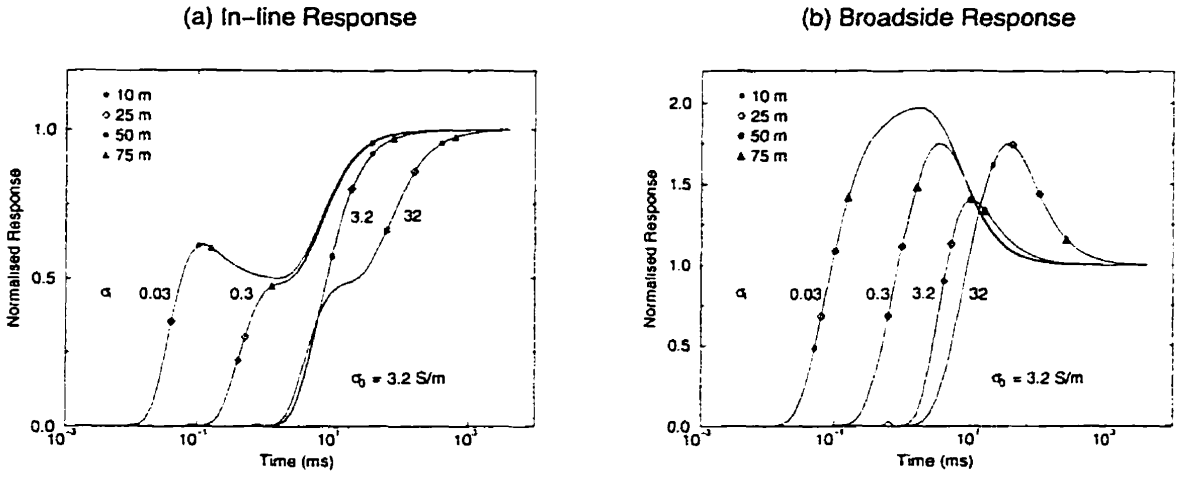

Figure 3.7: Loci of peak sensitivities to depths of 10, 25, 50 and 75 percent of the transmitter-receiver separation for (a) the in-line and (b) the broadside configuration with seawater to seafloor conductivity ratios of 100, 10, 1, 0.1. The transmitter-receiver separation is 100 m.

increase in late-time current flow through the seafloor combine so that measurements are sensitive to a given depth over a broader range of time, and overall sensitivity increases. From Figure 3.6 it can be seen that this is less true of the broadside component. Even over a highly conductive seafloor (panel (d)), sensitivity to structure at depths of up to half of the transmitter-receiver separation passes through a distinct maximum and falls off at late time.

The loci in time at which the sensitivity functions of Figures 3.5 and 3.6 peak are plotted on the step responses of the in-line and broadside configurations in Figure 3.7.

3.5 3-D Effects

The theory and sensitivity analysis described above is based on a one-dimensional model of the seafloor, while hydrothermal mounds are evidently three-dimensional. Model studies conducted by Evans and Everett (1994) and Yu and Edwards (1996) addressed the issue of how to interpret transient data collected on three-dimensional mound-like structures. Their proposed method of interpretation is based purely on differencing of travel-time measurement, and thus avoids dealing with amplitude distribution in the transient signal. As they point out however, large data sets are required to implement this method of interpretation. Their analysis did not address the issue of how to interpret sparse measurements which are inadequate for travel-time algorithms. In such cases differenc-

ing techniques cannot generally be used and the signature of three-dimensional features must be sought in the distribution of relative amplitudes within a single transient measurement.

Yu's program models a mound as an axisymmetric body in an isotropic seafloor beneath a conductive ocean, and is limited to transmitter sites which are off the mound by a distance roughly equal to the mound radius. While not generally suitable for modeling the case of a receiver stationed on a mound and a transmitter either on the mound or at the mound's periphery, it may be applied to give qualitative insights into the effects on the transient response of conductive or resistive regions occurring within the mound between transmitter and receiver. An example of a conductive region is a black smoker complex and its feeder network of high-temperature fluids; an example of a resistive region is a zone of anhydrite accumulation. Yu's program is applied to this problem by making the mound itself the isotropic seafloor, and representing a region of anomalous conductivity as the axisymmetric body in the model.

Figure 3.8 shows in-line and broadside step responses computed using Yu's program for cases of conductive and resistive regions between transmitter and receiver. The mound is assigned a conductivity of 3 S/m, equal to that of seawater, and a typical instrument separation of 100 m is used. In order to approximate the geometry of a high temperature fluid network, the region of anomalous conductivity is modeled as a semi-infinite vertical cylinder with a diameter of 50 m centered between transmitter and receiver. The cylinder is assigned conductivities of 1/10 and 10 times that of the surrounding whole-space for the resistive and conductive cases respectively.

The effect of such regions on the transient response of either configuration is dominated by inductive effects at early time and galvanic effects at late time. The diffusion of a transient field is opposed by secondary fields induced in the medium through which it travels according to Lenz's law. The strength of these secondary fields is proportional to the medium's conductivity. Diffusion therefore progresses more quickly through a resistive medium than through a conductive one. Accordingly, the presence of a resistive region between transmitter and receiver provides a fast path through which the source field travels, moving the observed first arrival to earlier time. Conversely, a conductive region between a transmitter and receiver will delay the first arrival. These effects are evident in at early time in Figure 3.8 in the delay of the first arrival for the response of the model containing the conductive cylinder, and the acceleration of the first arrival for the model containing the resistive cylinder. At late time (low frequency) galvanic

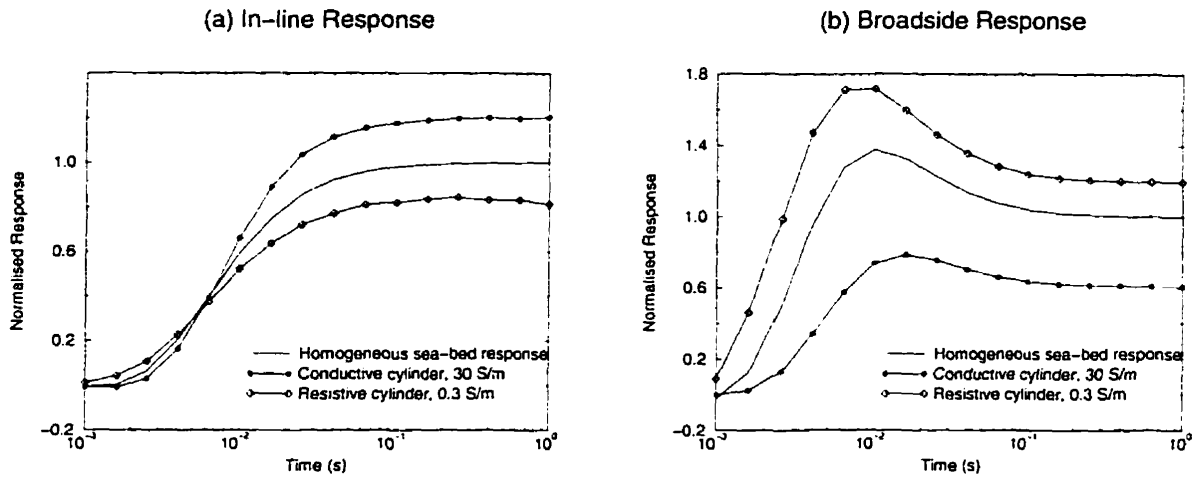

Figure 3.8: The effect of conductive or resistive zones between transmitter and receiver on (a) the in-line response, and (b) the broadside response. Transmitter-receiver separation is 100 m and mound and seawater conductivities are set to 3 S/m. The anomaly is a semi-infinite vertical cylinder of radius 25 m centered between transmitter and receiver, which is assigned a conductivity of 0.3 S/m for the resistive case and 30 S/m for the conductive case. Amplitudes are normalized by the whole-space late-time value.

effects dominate. A resistive region impedes the flow of current, which is diverted around it, whereas a conductive region will collect current and channel it. It is simple to show geometrically that secondary fields created by galvanic effects will enhance the primary field of the in-line configuration if the anomaly is conductive, and oppose it if the anomaly is resistive. Conversely, secondary fields of a conductive region will oppose the primary field of the broadside configuration, and those of a resistive region will enhance it. The relative amplitudes of the late-time fields in Figure 3.8 illustrate these effects. For the model containing a conductive cylinder the in-line response at late time shows a greater amplitude than that of a homogeneous sea-bed, whereas the opposite is true for the model containing a resistive cylinder. These relative amplitudes are reversed in the broadside response.

From an experimental perspective, a question of some importance is whether the presence of two- or three-dimensional regions of anomalous conductivity can be identified unambiguously when data is inverted, or whether their effects can be aliased with an inappropriate model. Figure 3.9 shows results of fitting the synthetic data from the cylinder model for in-line and broadside responses independently using a two-layered seafloor model. Free parameters in the inversion were the conductivities of the two layers and the thickness of the top layer. Evidently the models containing cylindrical anomalies cannot be distinguished from layered Earth models on the basis of individual in-line or

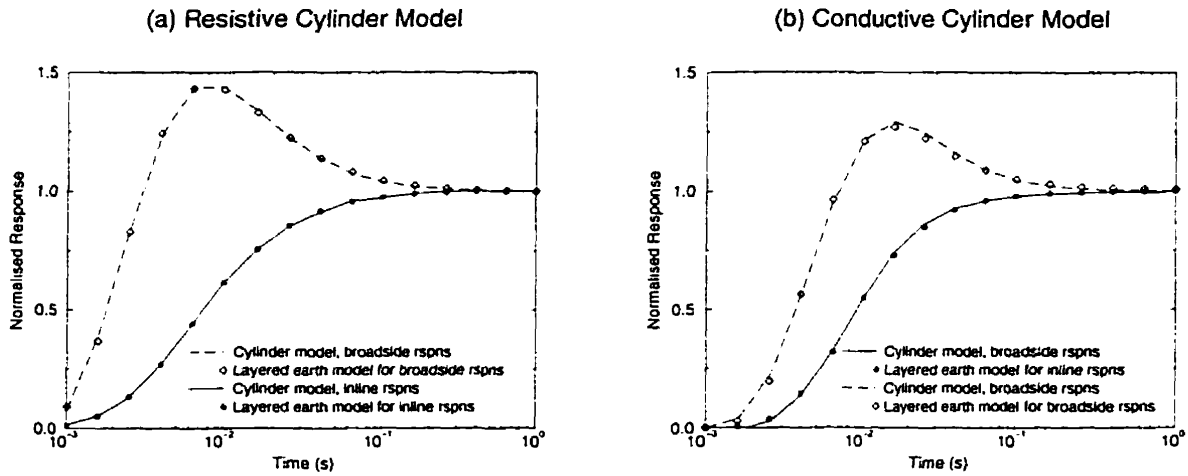

Figure 3.9: Two-layered earth fits to the synthetic responses of Figure 3.8. The conductivity of the upper layer, its thickness and the conductivity of the lower layer in each model are respectively as follows: (a) in-line (1.7 S/m, 8 m, 5.7 S/m); broadside (4.8 S/m, 27 m, 1.6 S/m); (b) in-line (1.4 S/m, 23 m, 5.9 S/m); broadside (4.6 S/m, 54 m, 0.4 S/m).

broadside measurements.

This does not reflect the general case of measurements made on the seafloor, however, which are seldom exclusively in-line or broadside but rather a linear combination of the two. Fitting a model to such measurements is equivalent to simultaneously fitting in-line and broadside responses, with a relative weighting that varies with transmitter-receiver geometry. A one-dimensional model which aliases effects of higher-dimensional structures for both components simultaneously does not generally exist. Figures 3.10 (a) and (b) show results of fitting equally weighted linear combinations of the broadside and in-line responses from the cylinder model with a layered Earth model. The fits are poor, and the distributions of fit residuals take on opposite signs for resistive and conductive cylinders. The reason is apparent from Figures 3.10 (c) and (d), in which the components of the synthetic data and the layered Earth models are shown separately. In Figure 3.10 (c) a more conductive seafloor would provide a better fit of the late-time in-line response, whereas a more resistive seafloor would provide a better fit of the broadside response. In Figure 3.10 (d) this pattern is reversed. The model to which the inversion converges represents a compromise between these conflicting requirements.

This suggests that the presence of three-dimensional structures can be differentiated from a layered Earth model when broadside and in-line responses are inverted simultaneously and that the nature of the region, whether conductive or resistive, may be inferred from

the distribution of residuals within a single combined measurement. While absolute imaging of such regions on the basis of individual measurements is obviously out of the question, the degree to which their characteristics can be quantitatively constrained merits further investigation.

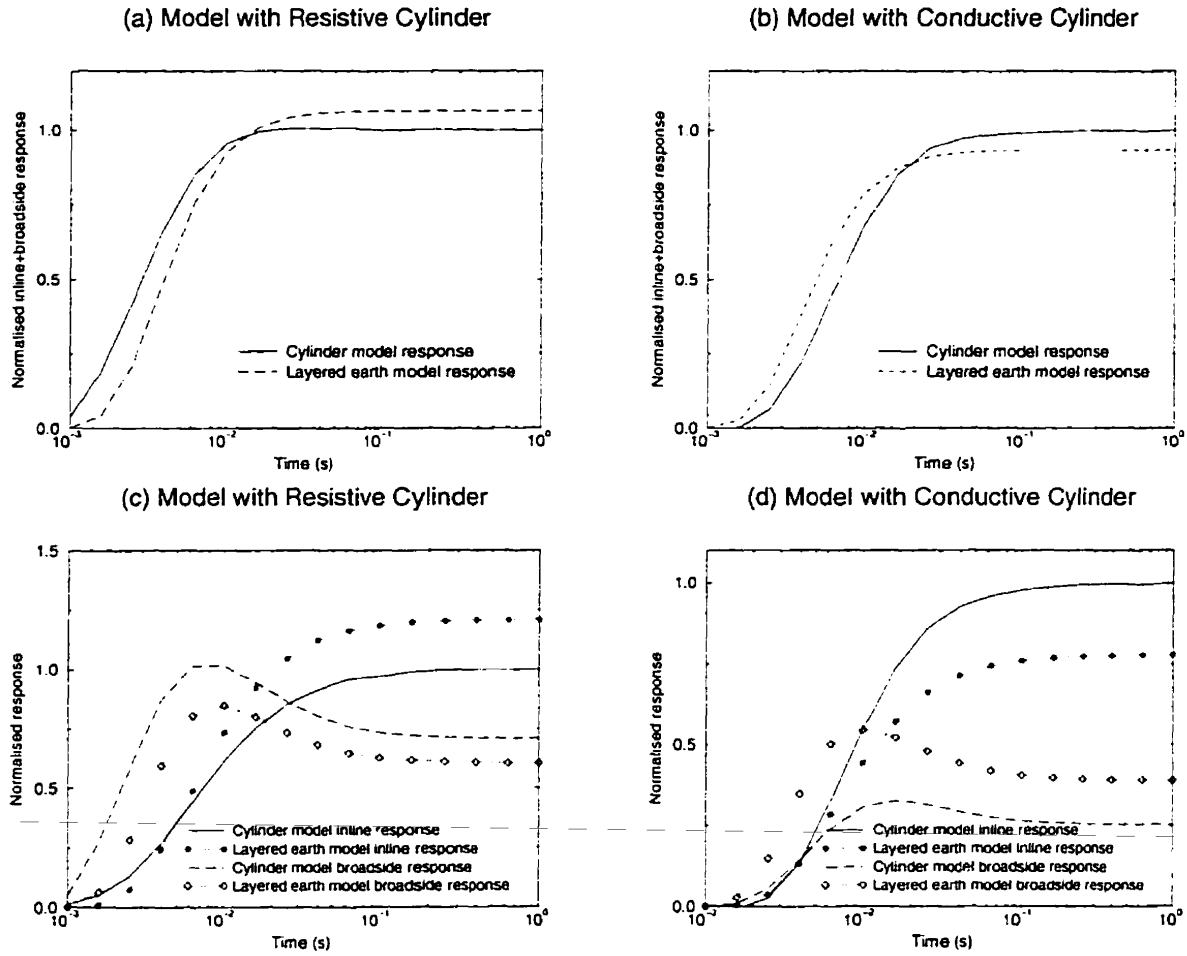

Figure 3.10: Fitting an equally weighted linear combination of in-line+broadside responses of Figure 3.8 using a two-layered Earth model. The conductivity of the upper layer, its thickness and the conductivity of the lower layer in each model are respectively: (a) 2.9 S/m, 13 m, 2.06 S/m; (b) 3.4 S/m, 13 m, 1.7 S/m. In (a) and (b) amplitudes are normalized by the late-time value of the combined response from the cylinder model. In (c) and (d) amplitudes are normalized by the late-time value of the in-line response from the cylinder model.

Chapter 4

Instrumentation

4.1 Introduction

In this work, marine transient electric dipole-dipole instruments have been developed that implement the theory outlined in Chapter 3. Each instrument is a self-contained unit with transmitter/receiver capability running autonomously under battery power and microprocessor control. The instruments are typically used in pairs, one transmitting while the other receives, both following a synchronized pre-programmed logging schedule. When transmitting, an instrument acts as a dipole current source, injecting into its surroundings a 3 A bipolar square wave identical to that used in classical time-domain induced-polarization surveys, but with a shorter period. When receiving, an instrument acts as a recording voltmeter, measuring time variations of the two components of the horizontal electric field on the seafloor and stacking them synchronously with the transmitter signal.

While the instruments may be conceptually divided into transmitter and receiver applications, there is overlap in the hardware through which these are implemented as control, logging and time-keeping functions are shared. The significant units of which each instrument is composed are as follows:

- Electric field sensors (electrodes)
- Two differential amplifiers
- Two-channel transmitter
- Oscillator board

- Data logger
- Battery pack

The electrodes are described in Section 4.2. The electronic modules are described individually in Section 4.3, and the manner in which they are interfaced is summarized in Section 4.4. The function (transmitter or receiver), logging parameters (transmitter period, stack depth, sample rate) and scheduling of an instrument during a survey are determined by software, allowing considerable flexibility in experiment design. The logging program is described in Section 4.5.

4.2 Electrodes

While measurement of the ambient electric field requires electrical contact with seawater, direct contact of metal with seawater is a strong electrochemical source of noise, creating an EMF which is variable from metal to metal but is always near one Volt (Filloux, 1973). In a thorough comparison of different electrode types, Petiau and Dupis (1980) concluded that Ag-AgCl non-polarizable electrolytic electrodes have the best overall characteristics with regard to noise, temperature stability and polarization with time, although Pb-$PbCl_2$ electrodes are a viable alternative. Ag-AgCl electrodes were adapted to marine measurements by Filloux (1973), and his design was further refined by researchers at Scripps Institution of Oceanography (Webb *et al.*, 1985).

The Ag-AgCl electrodes that are used on the receiver are identical to those used by Webb *et al.* (1985). Encased in 20 cm long tubes of porous polyethylene, they are filled with a mixture of diatomaceous earth and silver chloride mixed in a ratio of 6:1 by volume which surrounds a silver-coated plastic rod anodized with silver chloride. A connector cable is soldered to one end of the central silver rod, and the joint potted in a plastic cap using epoxy. Figure 4.1 shows the internal structure of such an electrode.

Dissolution of silver from the central rod is reduced by the powdered silver chloride, and water motion across the central rod which would cause noise due to streaming potentials is restricted by the porous plastic casing and diatomaceous earth. The impedance of these electrodes is about 1 Ω almost independent of frequency. DC potential between a pair of electrodes is typically below 1 mV (Webb *et al.*, 1984).

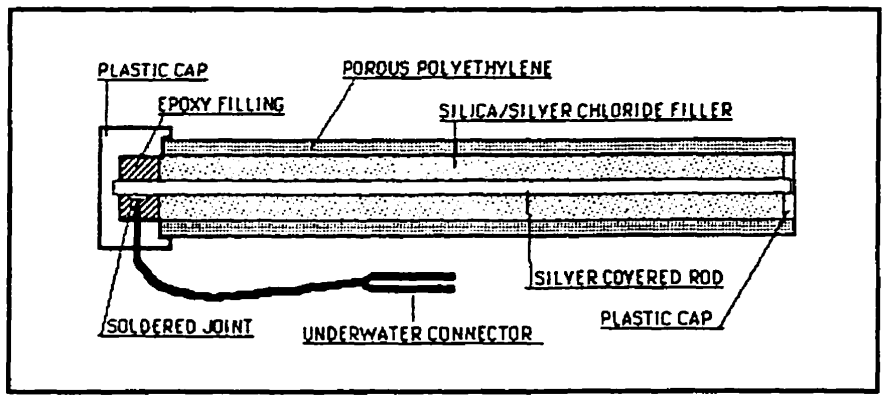

Figure 4.1: Diagram of an Ag-AgCl electrode (from Webb *et al.*, 1985).

4.3 Electronics

Amplifiers

Transformer-coupled FET amplifiers designed for low input impedance were used in the TAG experiment. On input to the circuit, the signal was chopped at 30 kHz with 4 low-resistance FETS to shift it into the passband of an audio transformer. The chopping signal was generated by a timer channel from the data logger (see description of the data logger's time-processing unit below). Following the main amplification stage, the signal was demodulated and then passed through a voltage controlled amplifier of variable gain. The gain of this backstage amplifier was determined by the averaged voltage of a variable duty cycle square wave running at 50 kHz on another of the data logger's timer channels.

The chopper amplifiers proved poorly suited to our purpose. They were unstable, noisy, and difficult to calibrate and test at sea. Their gain and frequency characteristics could not be determined with any consistency. Instrumentation differential amplifiers were therefore developed in 1994 which have proven far more reliable. The second-generation amplifiers are documented here to reflect the current state of the instruments, while the chopper amplifiers are described in Appendix A. Some examples of data collected on the seafloor with the new amplifiers are provided in Appendix B to demonstrate the quality of measurements that can currently be made.

The purpose of the amplifiers is to take small time-varying potential differences between the electrodes and amplify them to levels which can be digitized. The following considerations are critical on the amplifier inputs: (1) Electrodes must be the only connection to seawater, and all electronics (including grounds) must be isolated from the instrument case or ground currents circulating through the case will overwhelm the amplifiers; (2)

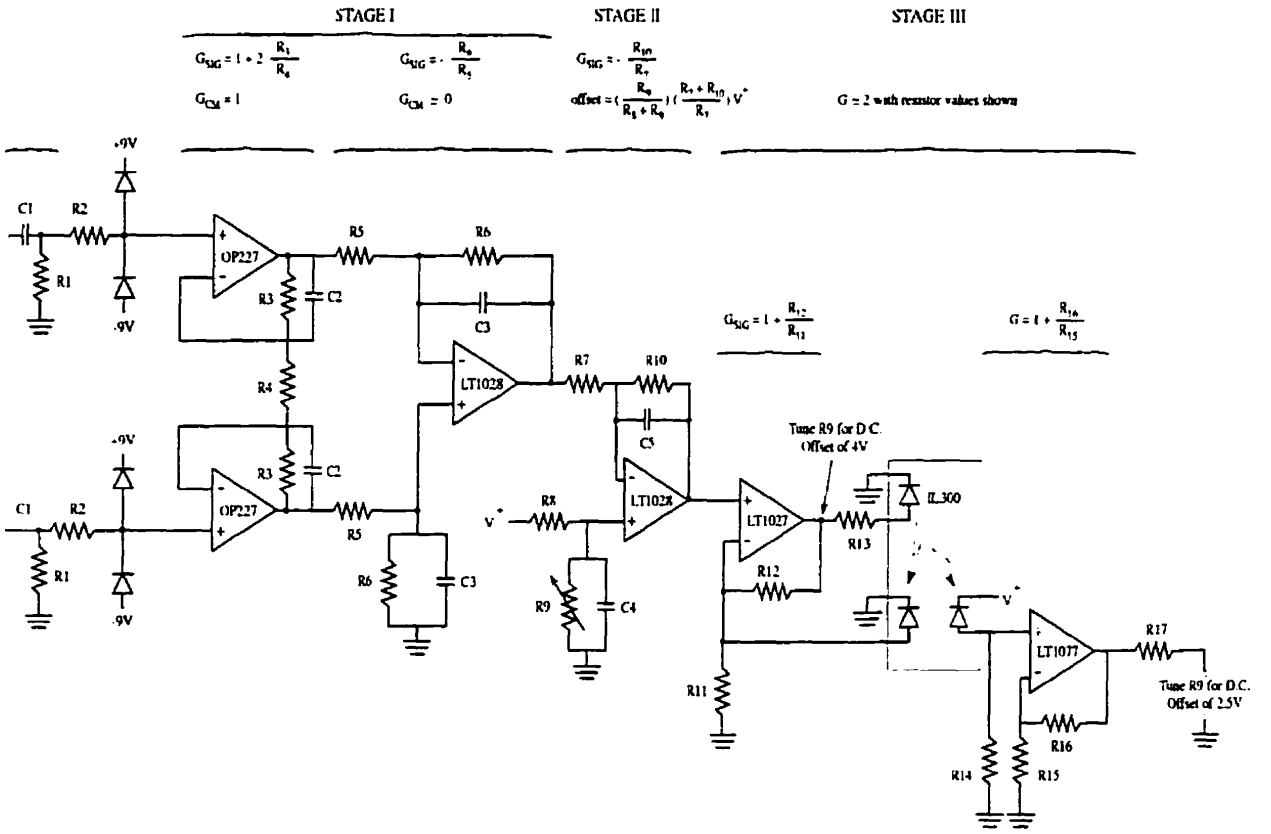

C1*	R1	R2	R3	C2	R4	R5	R6	C3	R7	R8*	C4	R9	R10*	C5*	R11	R12	R13	R14	R15	R16	R17
330μF	750Ω	750Ω	5kΩ	22μF	500Ω	5kΩ	50kΩ	100pF	2.2kΩ	470kΩ	0.1μF	0→1kΩ	273kΩ	100pF	10kΩ	10kΩ	820Ω	62kΩ	24kΩ	24kΩ	750Ω

Figure 4.2: Schematic of the second generation electric field amplifiers. Values marked with a star are regularly changed to adjust gain and bandwidth for a given experiment.

No DC connection can exist between electrodes as current flowing through them could force dissolution of their silver plating; (3) The low impedance ($\sim$ 3 Ω) of the seawater, electrode and cable source permits the amplifier inputs to also be of low impedance so that voltage noise is low; (4) Capacitive coupling on the input is necessary in order to block quasi-DC offset which develops between electrodes.

A schematic of the differential amplifiers used on the receiver channels is shown in Figure 4.2. While their basic configuration has not changed since they were built, gain and frequency response are routinely modified to match experimental requirements and values given here are for illustrative purposes only.

Input to the amplifier is differential and capacitor coupled. As the RC circuits on each side are joined through ground, the 330 μF tantalum capacitors and 750 Ω resistors that are typically used in this stage create a highpass filter with a 0.3 Hz 3dB point.

The first stage is a standard instrumentation amplifier, designed to amplify small differential signals with high common mode rejection. Assuming that the feedback resistors are well matched, common mode rejection of this stage is determined primarily by matching of the twinned input operational amplifiers. The Linear Technology OP227 dual-matched low-noise precision operational amplifiers used have a minimum common mode rejection ratio match of 110 dB. Differential gain of this twinned amplifier configuration is set to 21 using one percent resistors, and common mode gain is unity. The output drives a conventional differential amplifier circuit with a gain of 10, which generates a single-sided signal and removes the remaining common mode component. Feedback capacitor C3 stabilizes the feedback loop and is typically 100 pF for a 30 kHz bandwidth. As noise introduced in early stages will be amplified through the high gain stage that follows, Linear Technology's LT1028 ultra-low-noise precision high-speed operational amplifier with a minimum common mode rejection ratio of 126 dB is used.

The second stage, an inverting amplifier and level shifter, is where the main amplification and anti-aliasing filtering occurs. With the values shown in Figure 4.2, gain of this stage is 124 and its bandwidth 5 kHz. The DC offset of its output, and ultimately of the entire amplifier, is adjusted using R9. Due to its low-noise characteristics, an LT1028 is used in this stage also.

The final stage optoisolates the amplifier's front end from the data logger connection. As amplification from this point on is small, noise control in this part of the circuit is relaxed. An LT1027 low-noise high speed precision operational amplifier is used in noninverting configuration with a gain of 2 to drive a Siemens IL300 optocoupler, selected for its linearity and wide bandwidth. Optocoupler output is buffered by a backstage amplifier using an LT1077 single supply precision operational amplifier in a noninverting configuration with a gain of 2.

Gain of the optoisolation circuitry is not readily calculated theoretically due to large variations from sample to sample in optocoupler losses. It is about 2. Overall gain of the amplifier with the values shown in Figure 4.2 is $\sim$ 50000, and its bandwidth 5 kHz. To center amplifier signals in the digitization range of the data logger, the DC level of the output is adjusted to 2.5 V using trimpot R9.

Power for the amplifiers is provided by 9 V alkaline cells, which are mounted on the circuit board using velcro tape. Two 9 V batteries in parallel are used for each positive and negative supply voltages of the front stage. A separate 9 V cell powers the single supply backstage amplifier following the optoisolator.

Active amplifier components and resistors exhibit 1/f pink noise at low frequencies. Over the frequency range of interest the overriding instrumental noise is white Johnston noise from the resistors. It is therefore desirable for noise considerations to keep resistances in the early amplifier stages as low as possible. However, lowering the resistance in these stages increases the drain of the batteries which power the amplifier. The resistor values selected are a compromise between these two considerations.

Transmitter

The transmitter shown in Figure 4.3 acts as a bipolar switch, gating current from 9 V battery stacks according to optoisolated control signals from the data logger. These controls consist of a transmitter polarity signal running at the transmitter's base frequency and an on/off signal running at twice the base frequency, which in combination produce a bipolar square wave. With a step-on rise time of 5 microseconds, source signal bandwidth is considerably greater than that which can reach a remote receiver.

Under normal operating conditions, load resistance from cables, electrodes and seawater is only $\sim 2\ \Omega$. The battery packs, operating on a 25% duty cycle for logging periods of order 30 seconds, are therefore operating near short-circuit conditions and their internal resistance of $\sim 1\ \Omega$ is comparable to that of the load. Current output under these conditions is ± 3 A, and can be observed to decrease slightly over the time-span of an experiment due to battery drainage. As integrated power consumption is relatively low, however, this is a minor consideration.

Transmitter current is monitored with the circuitry shown in the lower right hand corner of Figure 4.3. The output of this monitor is calibrated to 0.25 V/A after optoisolation. Transmitter current is logged during each transmission sequence, providing a record of the source signal throughout an experiment.

Oscillator board

A precise time reference through which operations on remote instruments are synchronized is provided by MTI250-058 oscillators made by Milliren Technologies. Regulating crystal temperature with an internal thermostat and electric heater, these achieve a

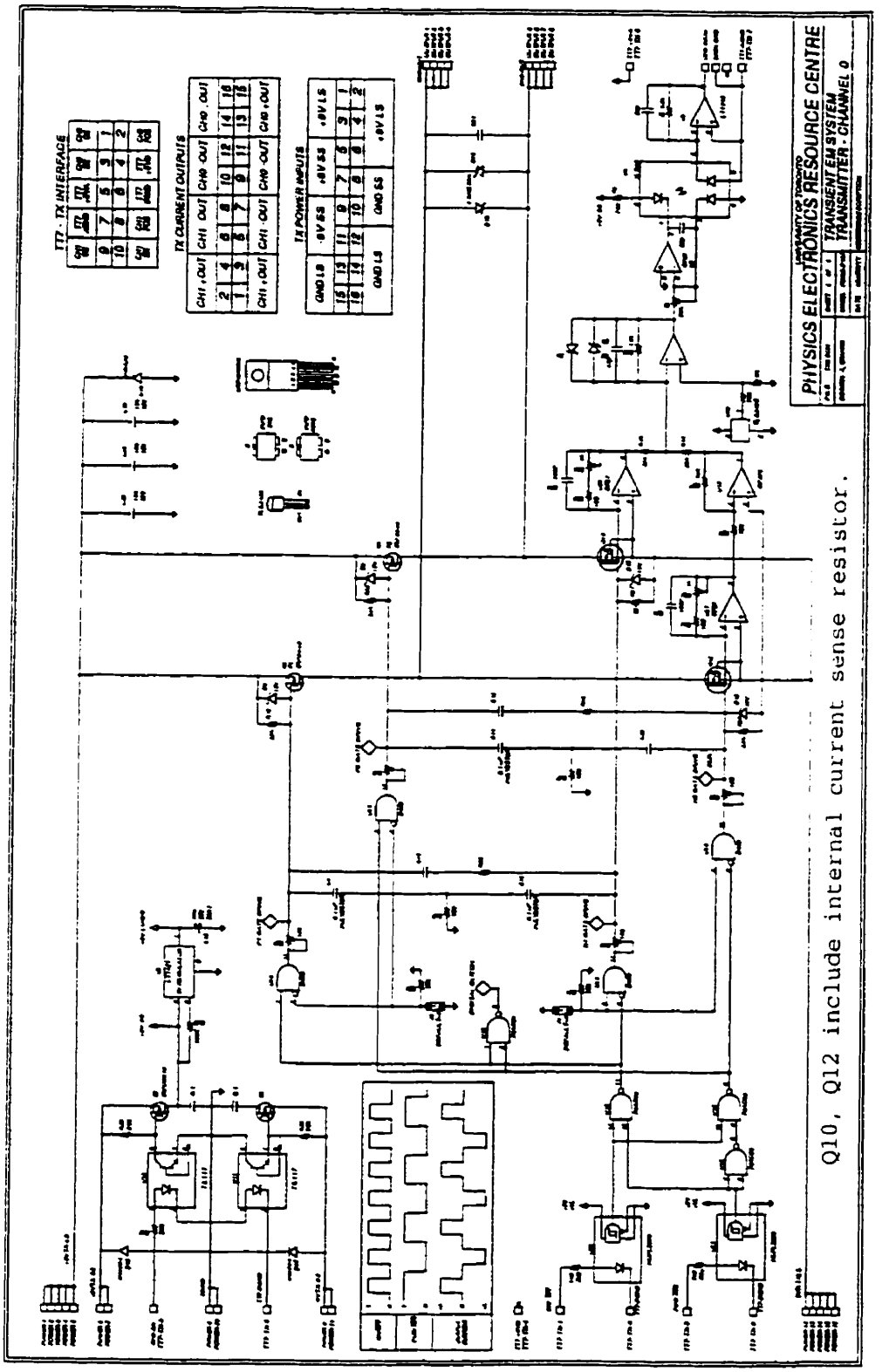

Figure 4.3: Schematic of one transmitter channel.

stated frequency stability of 1.5 parts in 100 million. Their base frequency of 5 MHz is tunable using external circuitry by 20 parts in 100 million. Power requirements are 5.0 Watts during a 7 minute warmup time and approximately 1.7 Watts thereafter, making this component by far the largest power consumer in the TEM instruments.

The oscillator output runs through a cascade of 48 binary counters with associated LEDs which may be stopped and reset through external circuitry (Figure 4.4). As a precaution, the LEDs are connected in an inverse mode. They are on when the corresponding counter bit is zero and off when the counter bit is one. Dead LEDs may therefore be observed when the counters are zeroed. The counters serve two purposes: they act as accumulators for the total oscillator cycle count and provide a range of high precision clock frequencies for various time-keeping tasks. Bits 2 and 6 of the series are jumper selectable for input to the data logger's time-processing unit, and bits 17 to 32 are available for a logging synchronization signal. The application of these signals is explained in Section 4.4.

The oscillator board also includes circuitry for a drop-weight release system used when the instruments are deployed with a buoyancy control unit and must return to the surface autonomously. Delay time to release is set by dip switches on bits 32 to 39 of the binary divider series. An independent PXO-600 based timer circuit with its own batteries forms a parallel timer. These two hardwired circuits provide double backup for a software-initiated release signal from the data logger.

Data Loggers

Each instrument is controlled by a Tattletale Model 7 (TT7) manufactured by Onset Computers. These are compact, general purpose data loggers suited to low power applications. Built around Motorola 68332 single chip microcomputers, they include onboard power supplies, time keeping functions, data logging hardware and both serial and parallel communication facilities. A peripheral hard disc may optionally be attached.

An unusual feature of the MC68332 is its time-processing unit, the functions of which are used extensively in the operation of the TEM instruments. Once initialized, this special purpose slave processor runs independently of the CPU, controlling two counters and sixteen digital I/O channels (Figure 4.5 (a)). One of the counters is driven by the system clock while the other may optionally be gated to receive input from an external oscillator (Figure 4.5 (b)). The counter frequencies are independently scaled by software-accessible binary dividers, providing considerable flexibility in time management (Figure 4.5 (c)). The I/O channels can be programmed to perform a variety of

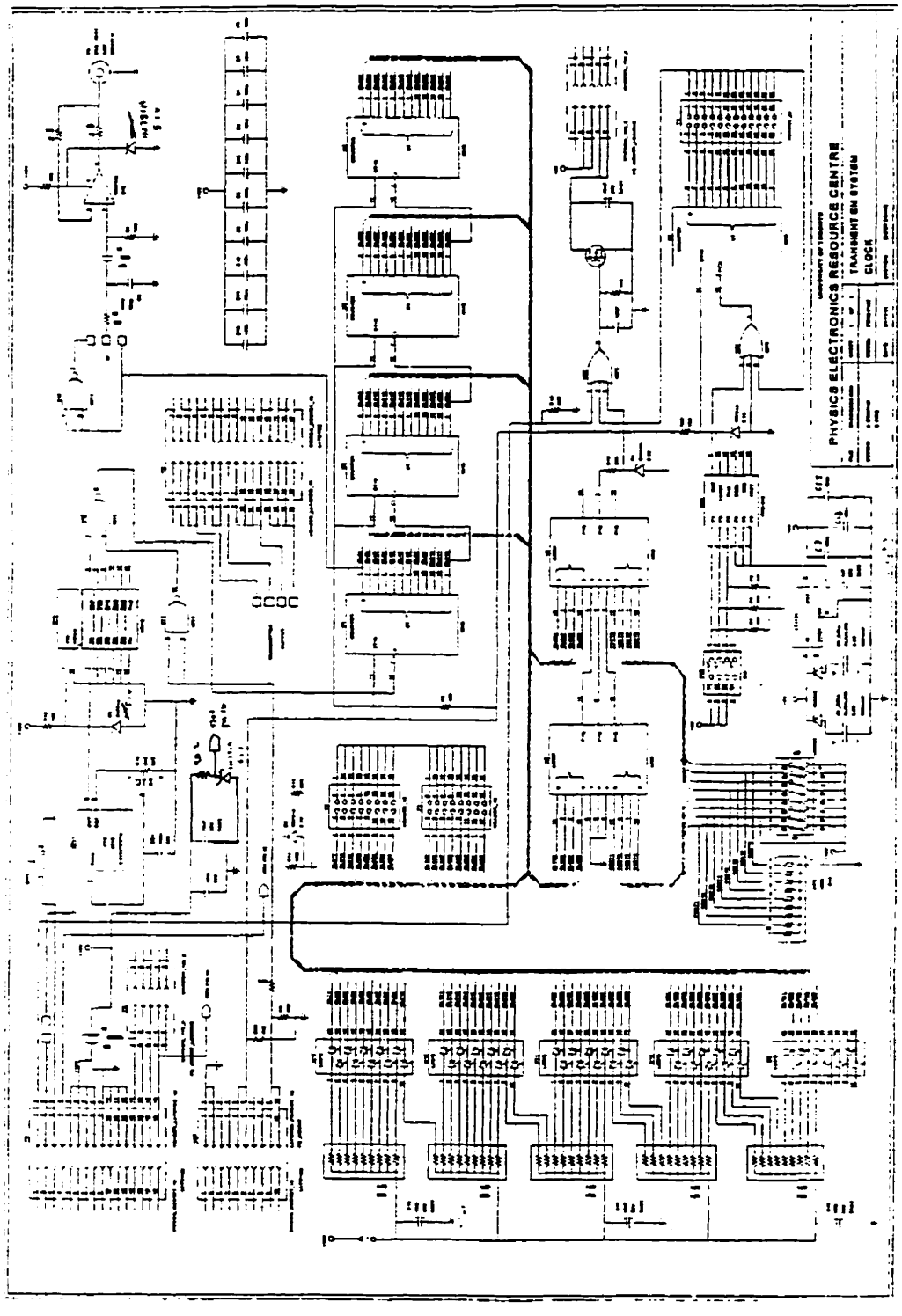

Figure 4.4: Schematic of the oscillator board which provides an accurate time reference through which the operations of remote instruments are synchronized.

time-based tasks. Functions used on the TEM instruments are pulse-width modulation, which generates a square wave with CPU controllable period and duty cycle, and synchronized pulse-width modulation, in which two or more linked channels concurrently generate pulse-width modulated waveforms with a specified phase shift between them.

Signal digitization is performed through a Siemens SDA 1812D: a 12 bit, 0 to 5 V successive approximation converter with built-in sample and hold and a four-channel multiplexer. Conversions may be initiated directly by software request, or by programming the time-processing unit to generate a pulse-width modulated track and hold signal which automatically triggers conversions with precise sampling intervals. The latter approach permits logging rates of up to 100 kHz. Operation at this rate requires that output impedance of the driving circuit be less than 3 kΩ in order for the sampling capacitor to be charged to an accuracy of 1/2 LSB within the 2.5 microsecond sample time.

A variety of chores useful to low power applications are performed by an independently clocked ICM7170 real-time clock (RTC) from Harris. In addition to acting as a time reference with a separate battery backup, its programmable alarm interrupt permits the MC68332 to be shut down to a low power sleep state during idle periods.

Of the 2.25 MB of RAM storage available on the TT7, 256 KB are fast static RAM used for run time variables and for volatile program storage, and 2 MB are pseudo-static RAM used for data storage and buffering to the hard disc. System and application software are generally stored in 512 KB of flash EEPROM which may be reprogrammed with an external voltage. Configuration information is stored in a 512 byte block of serial EEPROM requiring no special programming voltages, of which 384 bytes are free for the preservation of application variables when power is disconnected.

The TT7 runs on 7-15 V DC input. One onboard power supply converts this to power for the board's digital circuitry, another to power for the ADC and real-time clock. There is a separate power connection and power supply for the optional peripheral hard disc which may be run at 18 V. Aside from hard disc operations, overall power consumption depends primarily on the system frequency. The 68332 may be run at software controllable rates from 16 MHz down to a 160 kHz "sleep" state which is used to minimize power consumption during idle time. Power consumption is 30 mW + 30 mW/MHz (500 mW max.) when active, and 12 mW in sleep state.

A peripheral 2.5 inch IDE-compatible hard disc is mated to the TT7 through a buffered sixteen bit parallel I/O port. Due to rapid advances in hard disc technology over the

(a)

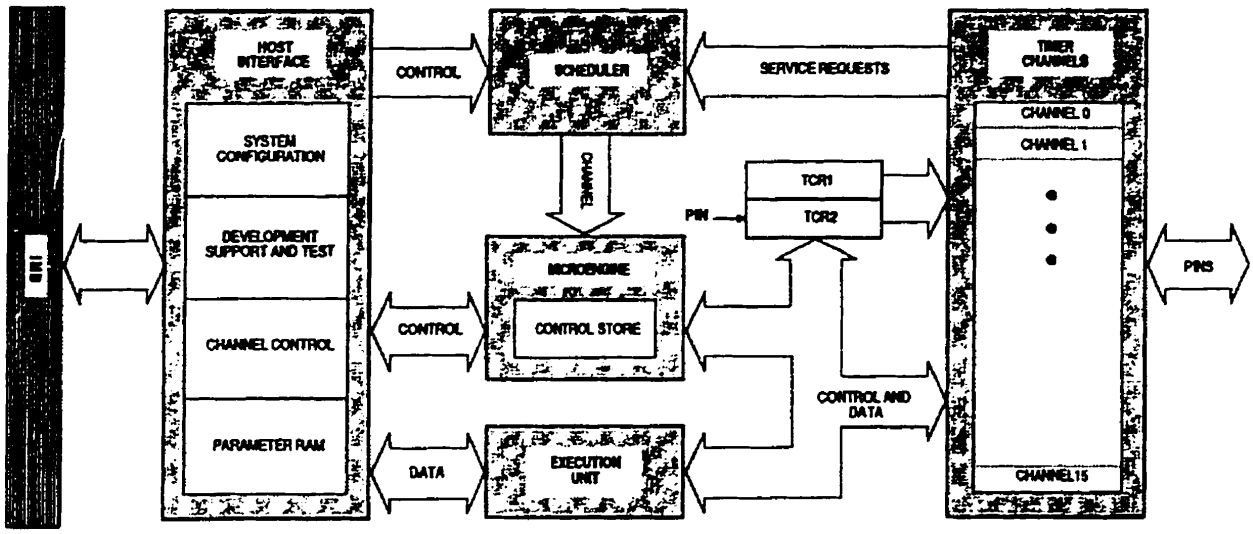

(b)

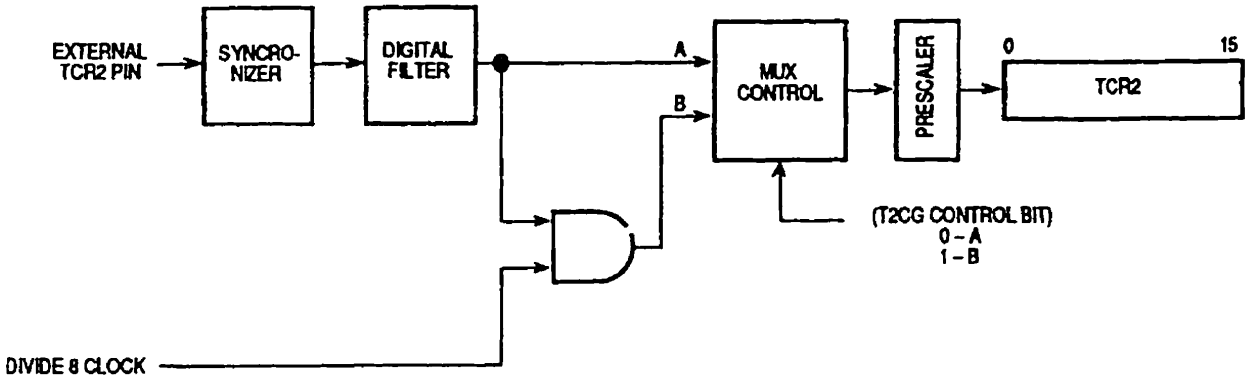

(c)

TCR2 Prescaler	Divide By	Internal Clock Divided By	External Clock Divided By
00	1	8	1
01	2	16	2
10	4	32	4
11	8	64	8

Figure 4.5: The MC68332 time-processing unit. (a) Block diagram of internal functions; (b) External clock input to the TCR2 counter; (c) Control register options for the TCR2 prescaler.

past few years, several models of disc drive are used on the instruments corresponding to their purchase dates. These include a 40 MB Connor CP-2044, an 80 MB Connor CP-2088, and several 120 MB Toshiba MK2124s. The power consumption of the hard discs has been found to vary considerably among the different models, but is at worst 4.3 W for several seconds during spin-up and 3.0 W during regular read/write operations.

While regular file functions are supported they are extremely inefficient (165 seconds to write 2 MB!). Instead, a blocked disk I/O system is used which optimizes transfers to and from the pseudo-static RAM. This requires that the drive directory be formatted to pre-allocate contiguous sectors for datafiles, which must be multiples of 32 KB. Disc access time using this approach is typically 11 seconds, consisting primarily of disc spinup time.

Communication with the TT7 takes place through an RS-232 serial connection, which may be run at rates from 1200 to 57600 baud. Program loading, interaction, and data off-loading take place through this link.

Battery Pack

The battery pack provides power for the transmitter, oscillator board and data logger. Alkaline cells were selected for this purpose from considerations of cost, energy density, internal resistance and low temperature performance. Their typical internal resistance of less than 1 Ω requires no recovery period between pulses to be maintained. The energy which can be extracted from the batteries drops significantly with temperature. The service hours obtained from batteries at a typical deep ocean temperature of 2°C is about 2/3 that obtained at room temperature under similar load conditions.

The battery pack uses Duracell C-cells which are custom packaged into bundles of three 6-cell-deep stacks (9 V) by Alexander Manufacturing of Canada. Seven such bundles are packed together into a cylindrical frame with a connector circuit board mounted on one end. Nine stacks are used in parallel for transmitter power. Eight stacks, connected as 4 parallel sets of 2 stacks in series, are used for the oscillator board. Four stacks, connected as 2 parallel sets of 2 stacks in series, are used for the data logger and hard disc. The 18 V output of these stacks is dropped to 15 V with a 3 V zenner diode arrangement for the data logger input, while the hard disc input uses the full 18 V.

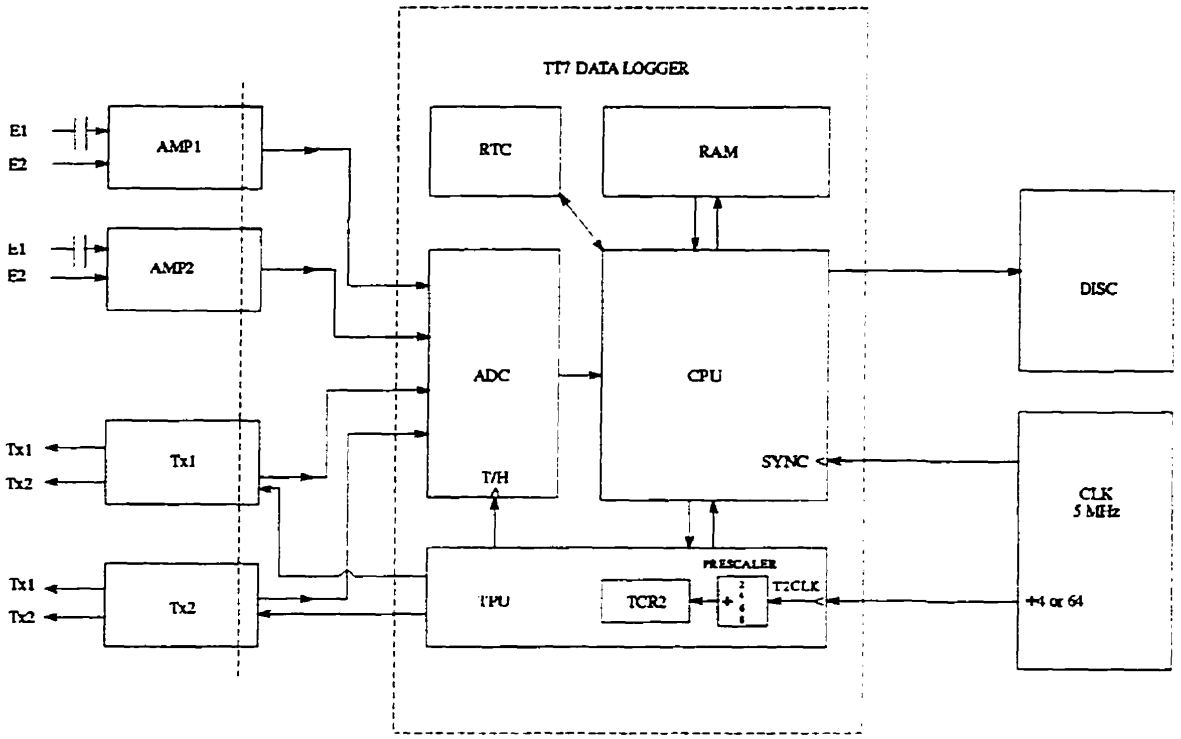

Figure 4.6: Block diagram of the electronic interfacing.

4.4 System Integration

Interfacing of the electronic modules is shown schematically in Figure 4.6. There are six different grounds: data logger digital ground to which the clock ground is tied; data logger analog ground to which the back stages of the two amplifiers and the transmitter current monitors are tied; a ground for each of the two transmitter channels; and a ground for each of the two amplifiers.

Transmitter current monitor and electric field amplifier outputs are sampled on the four channels of the data logger's ADC. Outputs are on a 5 V scale, diode-clamped to protect the data logger. Power for each transmitter channel is independently switched by the CPU using digital I/O bits to load and latch control signals through a serial to parallel shift register. Power for the present generation of amplifiers is left on at all times.

Two clock signals from the oscillator board are interfaced to the MC68332 on the data logger. One of these is a low frequency synchronization signal, generally jumpered for

a 6.7 second period, connected to the IRQ6 pin on the CPU. The IRQ6 interrupt is masked and signal state is determined by polling. The second clock signal drives the sixteen bit TCR2 counter on the MC68332 time-processing unit (Figure 4.5 (b)). Frequencies of either 1.25 MHz or 78125 Hz are jumper selected on the oscillator board for this purpose, and are scaled on input to the time-processing unit by a factor of 1, 2, 4 or 8 determined by a software-accessible write-once variable in the time-processing unit's system-configuration register (Figure 4.5 (a) and (c)). TCR2 frequencies ranging from 1.25 MHz down to 9765 Hz are therefore available. The value selected for a given experiment is a compromise between time resolution and the overflow period of the 16 bit counter.

Running with the accuracy of the oscillator board's oven crystal, the TCR2 counter acts as a time base for transmitting and logging functions. Timer channel transitions occur when TCR2 counts match CPU-determined values, and are therefore under software control. Two timer channels linked in synchronized pulse-width modulation mode generate transmitter polarity and on/off signals with a strict phase relation for each transmitter channel (Figure 4.11). A timer channel emulating the remote transmitter's polarity control signal acts as a time reference for data stacking during receive cycles. Whether transmitting or receiving, ADC sampling is initiated by a track-and-hold signal generated on a timer channel running in pulse-width modulated mode.

As the time-processing unit uses internal scheduling, it is unable to run many channels concurrently at high frequencies on a strict time base. For accurate timing it is therefore essential not to overload its capacity. Provided that this condition is met, the time-processing unit allows transmitter signal generation and data logging to be placed under software control, occurring synchronously on an accurate time base while leaving the CPU free to collect and store data.

4.5 Software

Control software for the instruments is written on a Macintosh Classic II computer in the C programming language with inline assembler for time-critical logging operations. A general flowchart of the control program is shown in Figure 4.7. Burnt into the flash EEPROM, the program executes automatically when the data logger is powered.

As disc I/O on the data loggers is expensive in terms of power and is cumbersome, logging and system configuration parameters are stored in the data logger's serial EEPROM

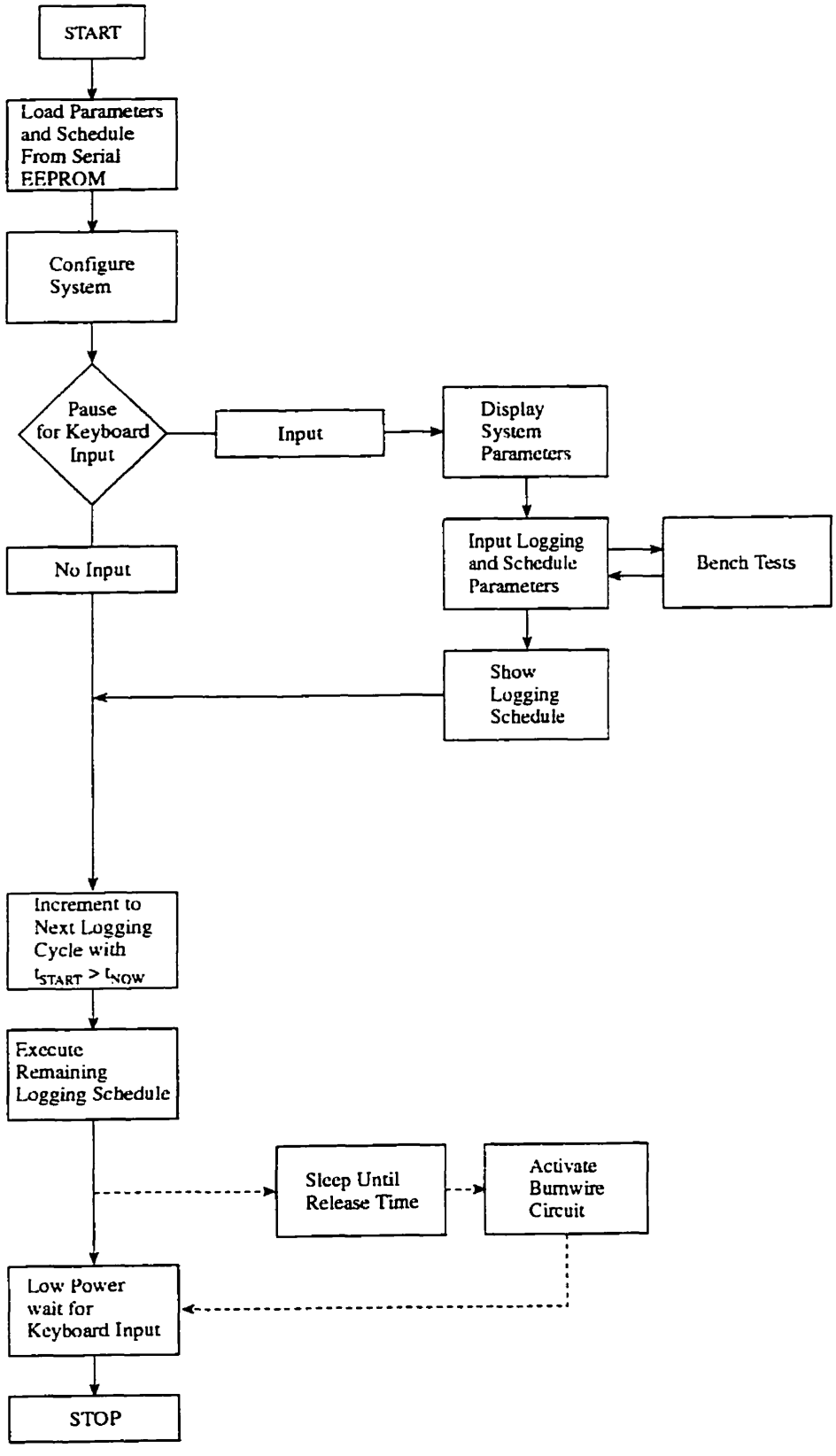

Figure 4.7: Main flowchart of the TEM program.

between power resets. The program begins by loading these parameters and using them to configure the system (Figure 4.8). As insurance against accidental resets during rough deployments, a timed polling of the serial port for keyboard input is then performed. If the polling times out without receiving keyboard input, it is assumed that the reset was accidental. The program then proceeds directly to the logging schedule, indexes itself by comparing the RTC time with successive cycle start times, and continues as usual.

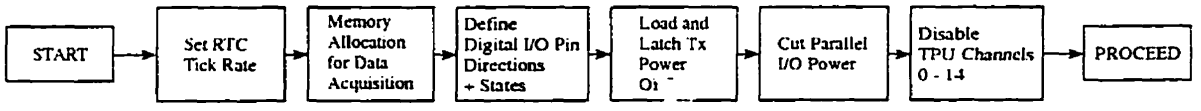

Figure 4.8: System initialization procedures.

In general keyboard input is received and the program proceeds to user I/O menus, a flowchart of which is given in Figure 4.9. As instrument deployment often occurs under adverse conditions, some simple measures are then taken to minimize user errors: a prompt to download the date/time from the Macintosh ensures that the RTCs on all instruments are roughly synchronized on "Mac-time"; the logging-synchronization signal is timed to confirm that it is being properly received and is identical on each instrument; and the time-processing unit's TCR2 frequency and system frequency are displayed as a check on software controlled divider values.

A menu is then displayed in which the following logging parameters can be set interactively: transmitter base frequency, ADC logging rate, number of transmitter cycles to stack, number of logging cycles, logging cycle offset, logging cycles per disc access, first cycle start time, and drop-weight release time. These parameters are written to serial EEPROM where they are preserved when power is disconnected, allowing advance configuration of the instruments and also the protection scheme against accidental resets described above. An optional branch is provided to a testing menu which is used for hardware debugging and to check the functionality of each electronics module prior to deployment. The logging schedule is then printed out and its execution begins.

A flowchart of the logging algorithm is shown in Figure 4.10. Data from each cycle are logged to contiguous memory blocks which must be the same size as pre-formatted datafiles on the hard drive. After pointer allocation, a header containing parameter information is written to the block, and the instrument is configured for the upcoming logging cycle. Allocation of timer channels is the only significant difference in configuration for transmit and receive cycles, which have been designed to mirror each other as closely as

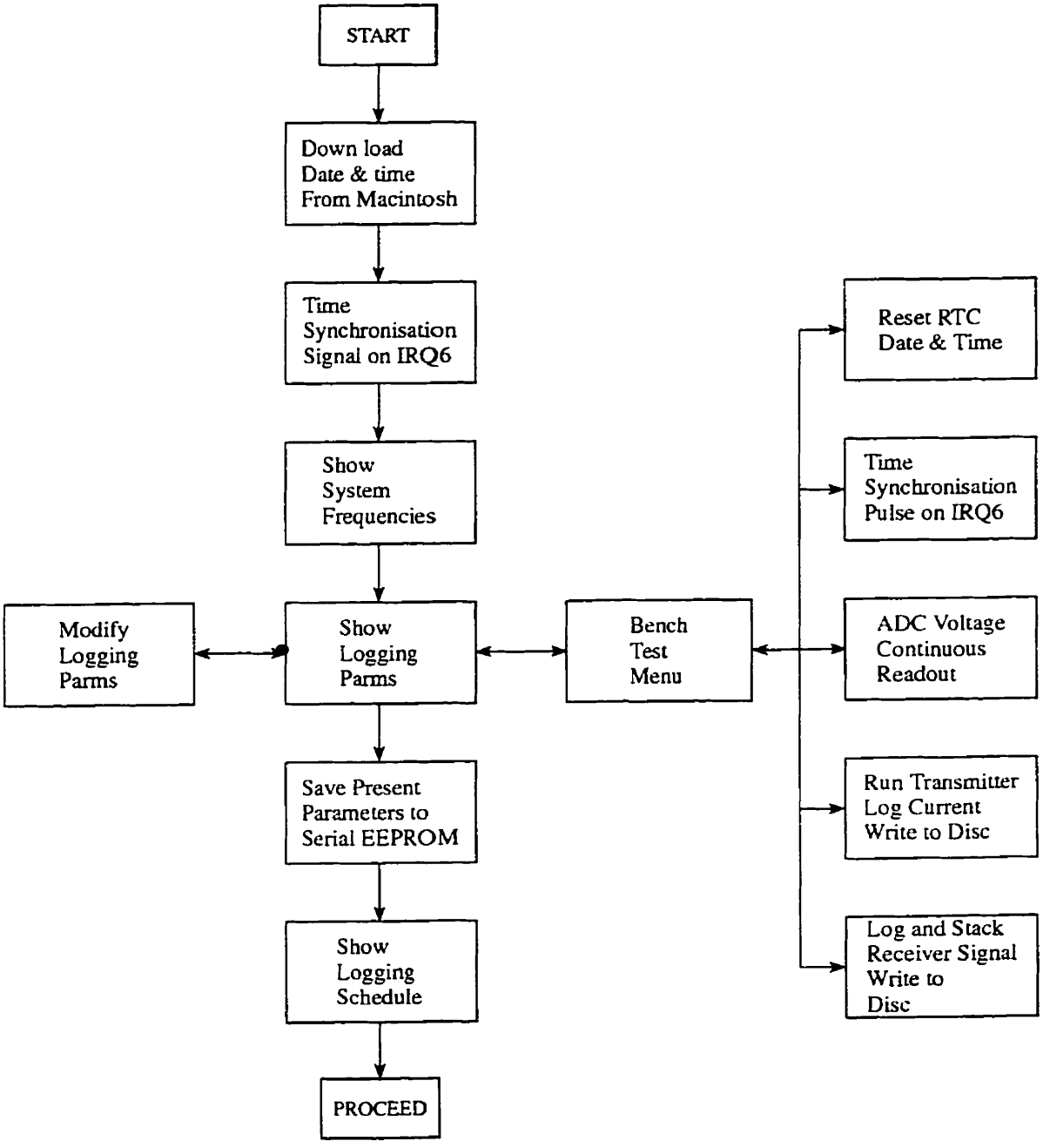

Figure 4.9: User I/O menus in the TEM program.

possible due to timing considerations.

The data logger is then placed in a low power sleep state until a programmed RTC interrupt signals the beginning of a logging cycle. After disabling unnecessary system functions which would interfere with high speed logging, the program waits for a positive transition on the logging-synchronization signal which coordinates transmit and receive functions on remote instruments. Appropriate timer channels are then started and logging begins. The transmitter current monitor output is logged during transmit cycles, while the seafloor electric field is logged during receive cycles. Data from successive transmitter periods are stacked to long-integer locations in the PSRAM. Stack resets are initiated by step-on transitions of a transmitter polarity timer channel. In transmitting cycles, this timer channel is actually driving the transmitter, whereas in receive cycles it is emulating the actions of a remote instrument. When the stack count is satisfied, a final cycle of raw data is written as short-integer variables in a contiguous memory range. A timing diagram of the logging process is shown in Figure 4.11.

The timer channels are then disabled, system functions are re-enabled, and information on the logging results is appended to the header in RAM. If no disc access is scheduled, the inner loop is repeated from pointer allocation on. If a disc access is scheduled, the disc is powered, PSRAM blocks are written to the pre-formatted data files, the disc is powered down, the PSRAM is cleared, and logging resumes from the inner loop. While electrically noisy, the disc is therefore never powered when an instrument is recording.

When the instruments are deployed with bottom assemblies and are to return to the surface autonomously, drop-weights must be released using a burnwire circuit once the logging schedule is finished. In this case, the logger will go to sleep until the scheduled release time, and then activate the drop-weight release circuit. Should the software fail, two levels of redundancy for the release are provided by timing circuits on the oscillator board.

The program finishes by monitoring the serial port for keyboard input. When this is received, signalling that it is back on the ship, a message confirming successful termination is printed and the program stops.

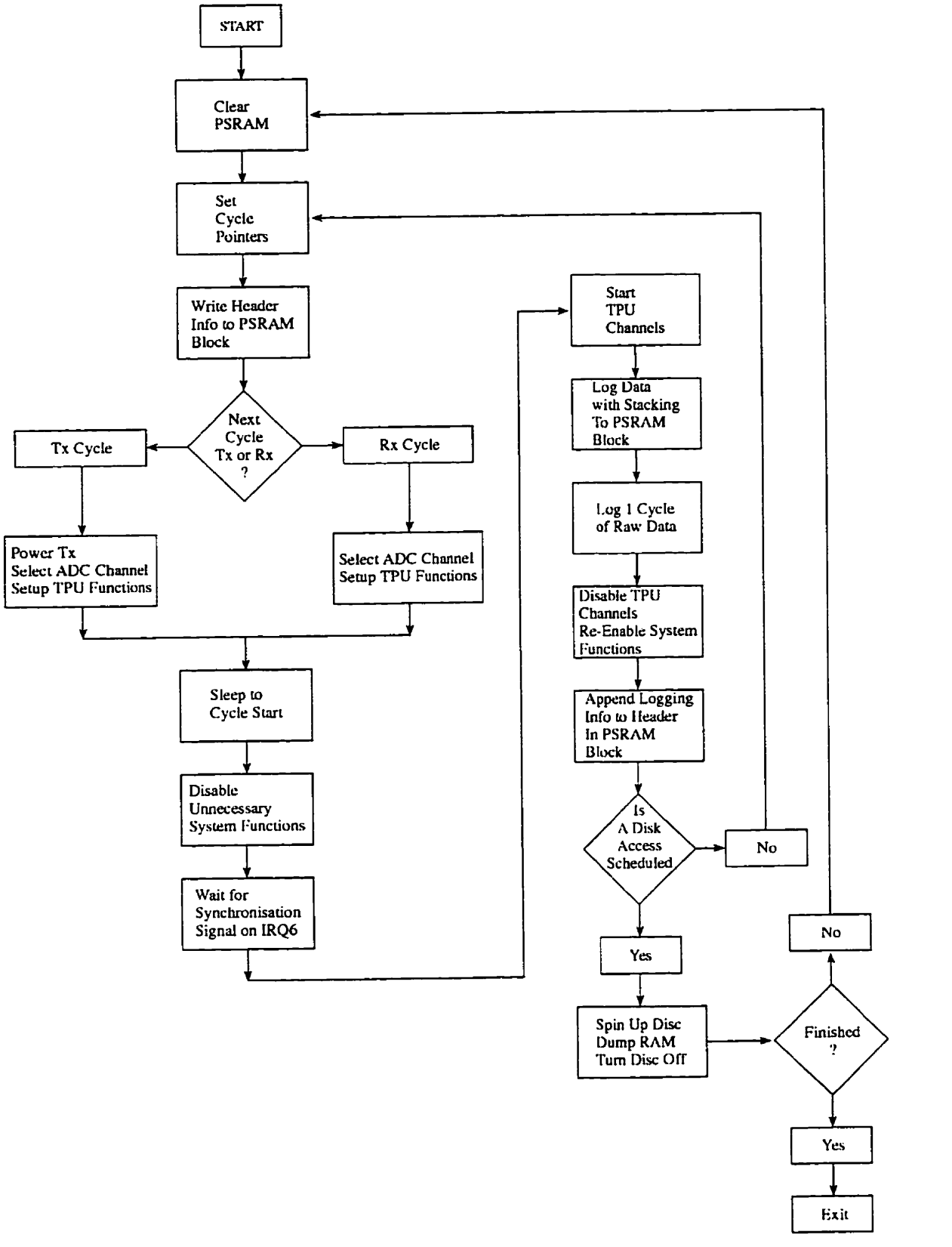

Figure 4.10: Flowchart of the logging routine.

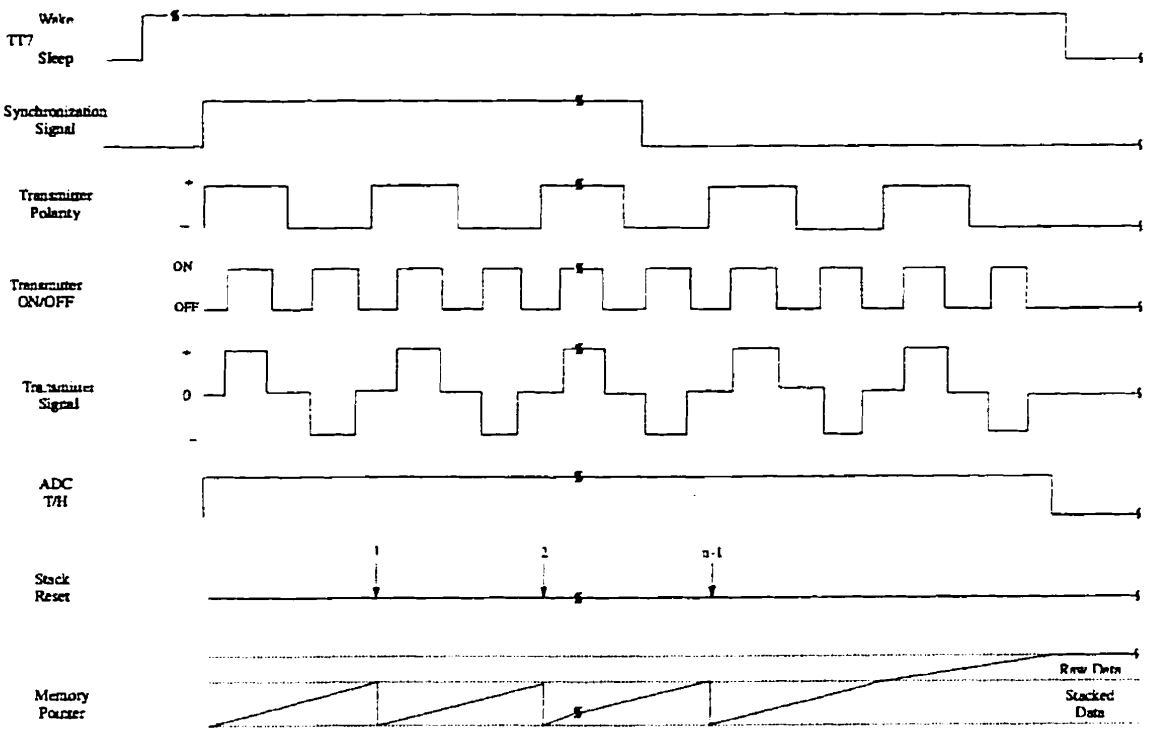

Figure 4.11: Timing diagram of a logging cycle.

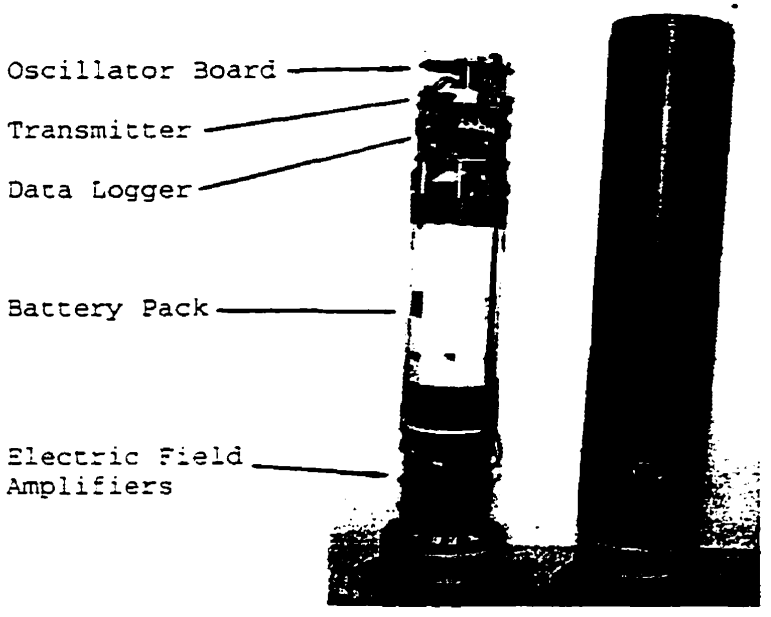

Figure 4.12: An assembled instrument and its pressure case.

4.6 Assembly

The electronics and battery pack were designed to assemble as a cylindrical unit, 75 cm long and 15 cm in diameter (Figure 4.12). In order to minimize noise pickup, the electric-field amplifiers are mounted on the far side of the battery pack from the other electronic modules. The assembly fits snugly into a tubular 6061 T6 aluminum alloy pressure case which is hard-anodized to resist corrosion and associated current flow in the case. Endplates made of the same material seal the pressure case with 'O' ring contacts, being held in place by threaded polypropylene clamping rings. Watertight electrical bulkhead connectors on the endplates provide connection to transmitter and receiver cables and an optional drop-weight system. The pressure case in turn locks into a protective plastic shell, on which PVC rods are mounted to extend transmitter and receiver electrodes. Strips of braided copper grounding cable ~1 m long are used for the transmitter electrodes, and the Ag-AgCl electrodes described in Section 4.2 are used to detect the electric field. The pressure cases have been tested to an ocean depth equivalent of 7 km.

Chapter 5

The TAG Survey

5.1 Introduction

In the planning stages of the TAG survey we had been informed that Alvin could not be used to carry instruments to the seafloor due to the danger of pressure cases imploding during descent. The survey strategy accordingly developed consisted of equipping four instruments with buoyancy control units and strobe lights, and dropping them from the surface ship onto the mound with the arms of the transmitter/receiver dipoles folded up vertically. Alvin was to visually locate the instruments on the seafloor by their strobe-lights, move them into a square formation, and unfold the dipole arms. Each instrument would transmit and receive in turn following a programmed logging schedule. At the end of the experiment, the instruments would release drop-weights permitting them to float to the surface where they would be picked up by the ship.

This stategy was attempted in the first deployment with disastrous results. Three instruments were deployed, the fourth being inoperative due to problems with a circuit board. One of the deployed instruments disappeared, apparently into the central black smoker complex, and the dipole arms on one of the remaining two instruments became tangled and snapped off when Alvin tried to unfold them. At the end of the experiment, the drop-weights on both instruments jammed in the tubes in which they were chambered, probably due to thermal contraction of the latter. The instruments were therefore marooned on the seafloor for 2 days until dive time could be spared for Alvin to rescue them by cutting off the drop-weights with cable-cutters.

Following this fiasco, a new deployment strategy seemed to be in order. As it had been demonstrated that the pressure cases could withstand the journey to the seafloor, the

Alvin pilots expressed a willingness to ferry the instruments to the mound in Alvin's sample basket. It was therefore decided to configure one instrument as a two-component receiver, and the second as a single component transmitter. Alvin would carry the instruments to the seafloor, where it would deploy the receiver near the center of the mound and then carry the transmitter through a survey path designed to circle the receiver at a range of $\sim$ 75 m, skirting the mound's periphery. Logging cycles would occur at intervals of a few minutes, providing measurements of the axial variations of the mound's conductivity.

The survey described below was the result of this approach.

5.2 Parameter Selection

Parameters were selected for the experiment assuming a transmitter-receiver separation of 75 m, the radius of the TAG mound. Seafloor conductivity was estimated to be between 0.1 and 10 S/m, the range from fractured basalt to *in situ* sulfide. As ambient noise on the seafloor within the signal bandwidth was expected to be very small, amplifier gain was determined from signal amplitude considerations only. Using equation 3.14 with $I = 3$ A, $\Delta l = 4$ m, $\sigma_0 = 3$ S/m, $\sigma_1 = 10$ S/m and $\rho = 75$ m gave a DC electric field strength of 1 μV/m at the receiver, or a potential difference of 4 μV over the 4 m length of the receiver dipole. As the signal was bipolar, the full peak-to-peak amplitude was 8 μV. A gain of 106 dB was chosen, bringing signal strength to 1/3 of the full ADC range, allowing a narrow margin of safety for smaller instrument separations or unexpected ambient noise. A duty cycle (% high time) of 30% was accordingly used on the 50 kHz pulse-width modulated signal regulating backstage amplifier gain, as described in Appendix A.

A transmitter repetition rate of 15 Hz was selected as a compromise between the desirability of measuring late-time arrivals and the undesirability of excessively long measurement durations. Consequently, each of the bipolar signal's four transitions, representing a complete transient measurement, had a period of 0.0167 seconds. This value was 6 times the seawater diffusion time of $\mu\sigma_0\rho^2/8$ at the planned transmitter-receiver separation of 75 m, and 190 and 2 times the respective seafloor diffusion times for seafloor conductivity of 0.1 and 10 S/m. Stack depth was set to 512 transmitter cycles, increasing the ratio of signal to random noise by a factor of 23. With a 15 Hz transmitter rate, this resulted in 34 second logging periods.

A cutoff frequency for the anti-aliasing filter was selected from signal rise time. For a

diffusion constant of 0.0007, corresponding to a seafloor conductivity of 0.1 S/m and an instrument separation of 75 m, the rise-time of the signal approximated by Equation 3.17 is 90 μs, and its bandwidth accordingly $\sim$ 2 kHz. A 10 kHz bandwidth was selected allowing for measurements at closer range. The low frequency cutoff would ideally have been chosen to fall below the signal's fundamental frequency. This, however, required larger blocking capacitors on the amplifier inputs than we could obtain before the cruise. Using the largest capacitors available, the low-frequency corner of the amplifier passband was measured to be about 50 Hz.

An ADC logging rate of 30 kHz was chosen to satisfy Nyquist sampling criteria with due regard to data volume and available frequencies from the data logger's time-processing unit. A frequency of 625 kHz for the time-processing unit's TCR2 counter was accordingly selected as a value slow enough that the desired transmitter period was less than that of one turnover of the 16 bit counter, yet fast enough to permit logging at the desired rate. Datafile and memory block sizes were set to 32 KB, that being the smallest datafile size available and greater than the data volume from one logging cycle of (4 byte stacked data + 2 byte raw data $\times$ number of samples per transmitter period + 1024 byte header block.)

5.3 Pre-Dive Tests

Prior to the experiment, the amplifiers were tested by running a 1 kHz, 121 mV_{pp} square wave from a function generator through a step-down transformer and a voltage divider to give a 25 μV_{pp} signal on the input. The amplifier output was monitored on an oscilloscope to measure the gain. This was varied by changing the duty cycle (100$\times$ratio of high- to low-time) on the 50 kHz pulse-width modulated signal from the data logger's time-processing unit which was averaged to determine the gain of the voltage controlled amplifier (see Appendix A). Gain was plotted as a function of duty cycle and confirmed to approximate the specification of 74 dB + 0.46 dB $\times$ (100 - duty cycle). As amplitude is used only as a rough check in our interpretation, this level of gain measurement was considered sufficient.

The transmitter was tested from the bench test menu (Figure 4.9) with a 4Ω power resistor load. Voltage across this load was observed on an oscilloscope to swing $\pm$ 7.4 V, giving a current of 1.85 A. With a fresh 9.45 V battery stack, this placed the internal resistance of the transmitter at 1.1Ω. The transmitter current was logged with a 512

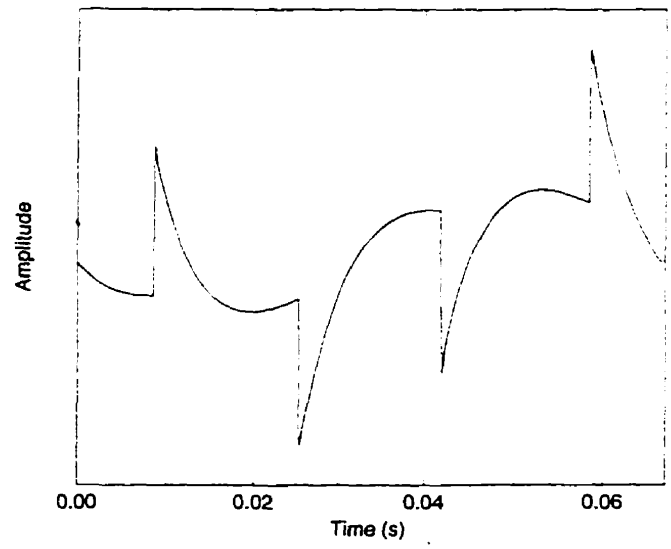

Figure 5.1: Record of transmitter current convolved with receiver response recorded during pre-dive simulation.

deep stack to calibrate the transmitter current monitor. The data showed voltage steps of $\pm$ 0.48 V, or 0.26 V/A.

Leads were then connected across 2Ω of the transmitter's resistor load, through a 74 dB attenuator, and into the receiver inputs, such that the receiver could log the transmitter's signal. The instruments were programmed with a shortened dive simulation, including multiple logging cycles and disc accesses with logging parameters identical to those used during the experiment, with the exception of amplifier gain which was set to 5000. The oscillator counters were synchronized, and the dive simulation run. When the simulation was finished, the transmitter current monitor data and receiver data were offloaded to the host computer. The receiver data provided a record of the convolution of the transmitter signal with the receiver's response, which was retained for use in modeling (Figure 5.1).

5.4 The TAG Survey

The first phase of the TAG experiment was deployment of a transponder net for seafloor navigation two weeks prior to the survey proper. Such nets are used as follows:

1. Transponders are dropped from the surface on bathymetric highs bracketing the survey area.

2. The ship's absolute position is determined by differential GPS to an accuracy of $\sim$ 5 to 10 m.

3. Transponder position on the seafloor is determined relative to the ship from travel times of acoustic handshake signals between ship and transponder at multiple ship positions.

4. Submersible position on the seafloor is determined relative to transponder pairs by measuring travel times of acoustic handshake signals with each transponder, and using these to triangulate position on a plane. Depth is determined from pressure gauge measurements.

The TAG EM survey was conducted on May 14, 1993. Preparation of the instruments began at 0200 local time in the laboratory of the Atlantis II, with the instruments running off a power supply. Through software, one instrument was configured as a single-component transmitter and another as a two-component receiver logging on alternating channels. The logging schedule was set to run continuously for 5 hrs starting at the estimated bottom arrival time of 1030, determined as Alvin launch time of 0800 added to the 2.5 hrs descent time. Logging cycles were programmed at 5 and 5+1 minute intervals, with data transfers from RAM to disk occurring once an hour. The parameters were set as described above, and the matching battery voltages on all instruments were carefully measured and recorded.

During this time, electrode assembly was proceeding on the deck (Figure 5.2). Receiver electrodes were connected to their cables with watertight joints. The cables were color coded according to the channel and polarity of their connections to the amplifiers, so that they could be distinguished in video images of the dive. The electrodes for one receiver component were taped to opposite ends of a 4 m long PVC beam; the electrodes from the second component were left loose. The single transmitter dipole was assembled by soldering and taping meter long lengths of braided copper grounding wire to the transmitter cables, and then coiling and taping them around opposing ends of another 4 m long PVC beam. The transmitter and receiver beams were then fastened to the outer casing of their respective instruments using gear clamps.

At 0500, the instruments were switched to battery power. The oscillators were allowed an hour to stabilize. Their outputs were then monitored on an oscilloscope and the

Figure 5.2: The instruments on the deck of Atlantis II immediately prior to deployment. Ag-AgCl receiver electrodes can be seen taped to the far ends of the receiver dipole. Electrodes for the second receiver component are mounted on the instrument casing in preparation for seafloor deployment. The buckets contain salt water, in which the electrodes must be stored when not in use to prevent their electrolyte from drying out.

frequencies tuned until no drift was visible between the two oscillators over a 10 minute period. Meanwhile, the O-rings and O-ring surfaces on the pressure cases were cleaned with methyl-alcohol and greased with Dow Jones Compound 4 (it is important *not* to use vacuum grease for this purpose as it crystallizes at high pressure). The host computer was coarsely synchronized to GPS time, and this time was downloaded to each instrument. At 0600, the oscillator counters on the two instruments were synchronized by zeroing them simultaneously. The instruments were immediately sealed in their pressure housings and carried to the deck where they were assembled with their protective casing and the external frame. A short length of heavy rope was shackled to the receiver frame to act as a handle. The transmitter and receiver cables were connected using watertight connectors, and the instruments mounted in Alvin's sample basket with the receiver on the outside such that the PVC beams were projecting at right angles to Alvin's longitudinal axis. One electrode of the free receiver component was taped to the receiver beam next to the pressure housing; the cable connecting the second free receiver electrode was coiled in "figure 8s" against the frame and weakly fastened in place with elastics. The rope handle on the receiver was twisted in Alvin's manipulator claws, both to secure the receiver during deployment and descent and in preparation for deployment on the seafloor.

Alvin was launched on schedule at 0800 in calm seas with a moderate ground swell (Figure 5.3). The pilot for the dive was Dudley Foster, and Rob Evans and Keir Becker were scientific observers. Alvin dropped at $\sim$ 0.5 m/s for almost 2.5 hrs before reaching the mound. After a 10 minute reconnaissance, a receiver site was selected in a small depression amid sulfide rubble on the upper platform 30 m south of the black smoker complex at a water depth of 3656 m, slightly north of ODP marker B (Figure 5.4). Using Alvin's manipulator claws, the receiver was placed on the seafloor and the coiled electrode was extended about 6 m perpendicular to the orientation of the rigid dipole. Receiver deployment was completed at 1057, having taken 20 minutes.

Alvin, carrying the transmitter, then proceeded northwards to begin the EM survey. The scientific observers had been provided with copies of the logging schedule, and throughout the survey care was taken to keep Alvin close to the bottom and moving slowly while measurements were taken. Circling the black smoker complex on the western side, Alvin passed over shimmering waters before reaching the drop off at the northern scarp wall. The EM survey was then interrupted to deploy ODP marker C. Resuming the survey, Alvin descended the northern wall to a depth of 3675 m and began a counterclockwise survey path designed to circle the receiver at a radius of 70-80 m.

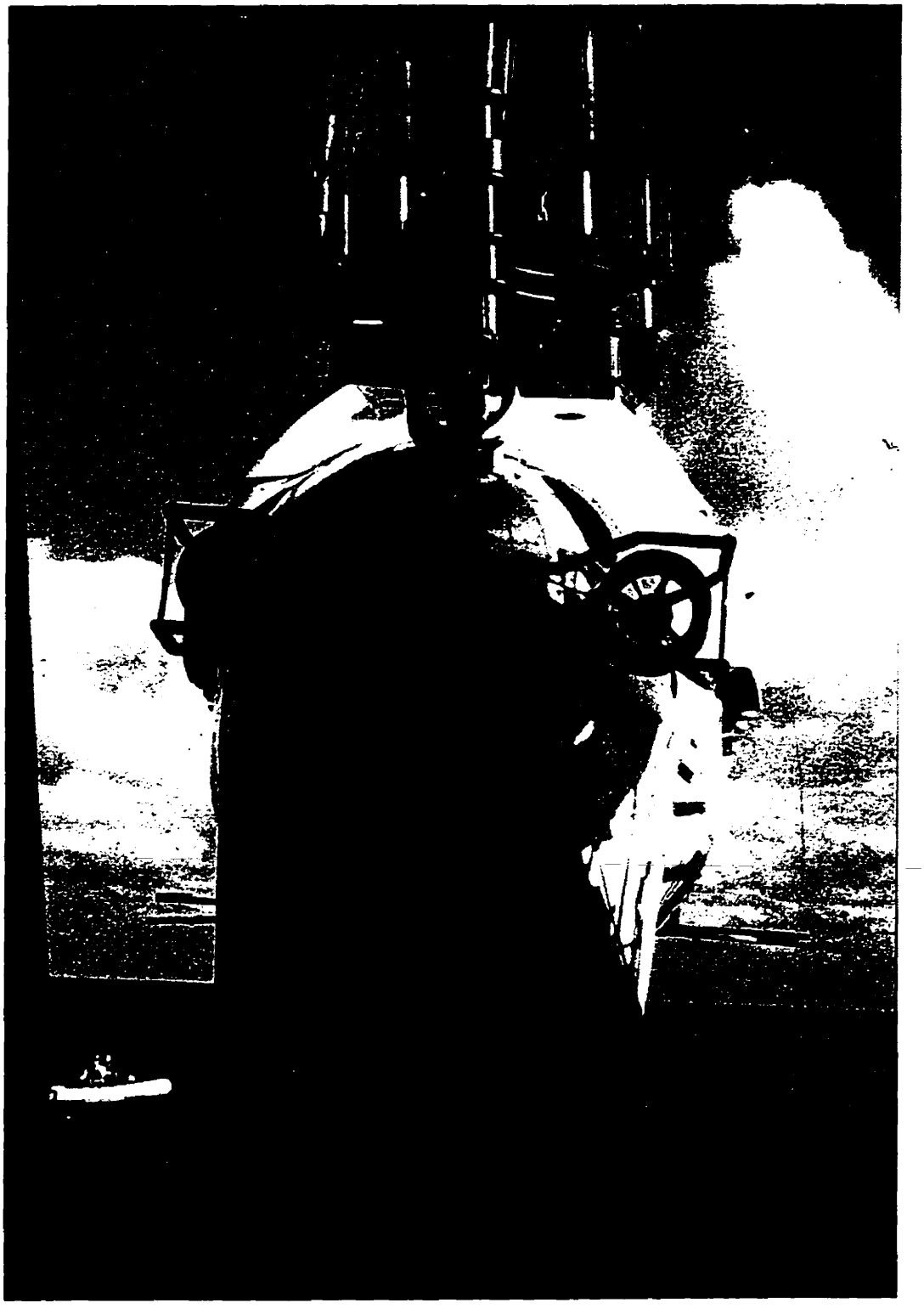

Figure 5.3: Alvin being launched with the TEM instruments. Transmitter and receiver electrodes can be seen projecting on PVC beams.

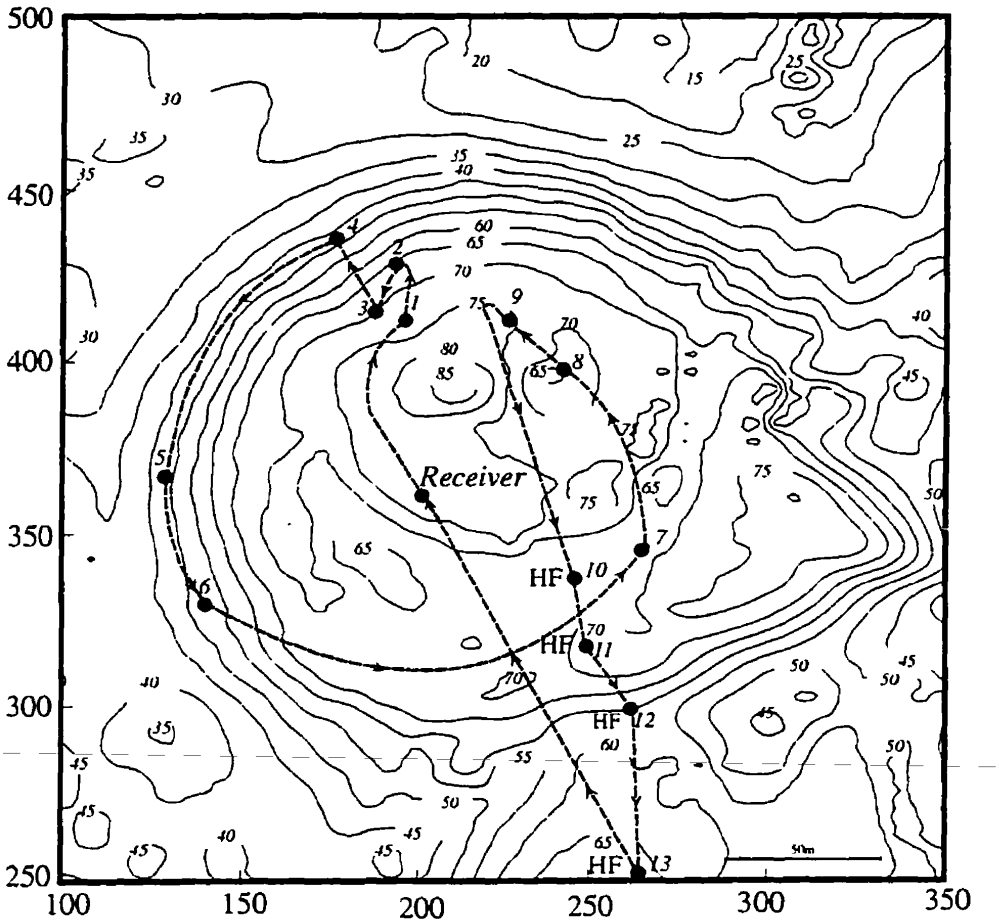

Figure 5.4: Bathymetric map of TAG showing the survey path. Numbers 1 to 13 are sites from which interpretable data were collected. Sites marked HF denote stations where conductivity data were collected during heat flow measurements. North is upwards.

Throughout the NW sector, Alvin's path hugged the sulfide talus of the scarp wall at a depth of $\sim$ 3675 m. Entering the SW sector, the surface bathymetry rose and Alvin continued at a depth of $\sim$ 3665 m as it crossed several small valleys before emerging on the lower platform. The geology of the SW sector was notable for the abundance of carbonates in both block and sediment form among the sulfides. In the SE quadrant, the survey path crossed the Kremlin area where rough level sulfides were interspersed with extinct chimneys. Proceeding northward, Alvin returned to the upper platform where shimmering waters and a white smoker were observed due east of the receiver position, and then crossed the depression in the NE quadrant, which was full of rough sulfides. Emerging from this depression, a small ridge trending 40° was crossed where inactive chimneys were observed about 10 m to the NE. The survey circle was completed at 1206 when Alvin reached the drop-off wall north of the black smoker complex, slightly over an hour after deploying the receiver.

This ended the planned EM survey. The remaining dive time was allocated to heat flow measurements. As the transmitter was still running and did not interfere with these, it was kept in the sample basket and additional EM data were obtained at the heat flow sites. These lay in a line that transected the mound east of the black smoker complex, trending $\sim$ 160°. Between stations Alvin moved too fast for EM measurements, but at each station Alvin rested on the seafloor for 20-30 minutes at a time, providing multiple EM soundings at each site.

EM data were collected at five sites during the heat flow transect. The first such site was about 40 m NE of the black smoker complex, in a region of patchy sediment over sulfide rock. The next three were in the Kremlin area in the SE quadrant of the mound. One was amid weathered sulfides with a transition to carbonates close by, a second was amid carbonates, and a third was on a $\sim$ 5 m wide terrace amid sulfide debris and carbonates. The last site was off the SE side of the mound amid carbonates with occasional sediment-covered pillow lavas.

The heat flow transect was finished at 1425, and Alvin returned to the receiver. In a 5 minute operation, the receiver was recovered by its rope handle and placed in the sample basket. Alvin left the bottom at 1446, carrying the instruments back to the surface. During the ascent, the loose receiver electrode floated out of the sample basket and broke off. As soon as Alvin was back on the ship, the instruments were dismantled and taken back to the laboratory where the oscillator cycle counters on the two instruments were stopped simultaneously at 1715 and the cycle counts recorded. Battery power

to the instruments was disconnected and final battery voltages recorded. The data were transferred to the host computer with the instruments running off a power supply. Copies of Alvin's navigational log, videotapes, and dive reports from the scientific observers were retained for analysis. So ended the first small-scale EM survey on the ocean floor!

5.5 Examples of Data

A few samples of unprocessed data are shown in Figure 5.5. The variation in waveforms is due to changes in relative weighting of in-line and broadside components with transmitter-receiver geometry. Noise in the measurements is due to the chopper amplifiers as discussed below, and has well determined frequency characteristics. Improvement in signal-to-noise ratio with stacking is apparent.

5.6 Data Reduction

Navigation

Navigation was the central problem of data reduction. Interpretation of TEM data is contingent on a knowledge of the transmitter-receiver separation and relative orientation, as error in these parameters translates to error in the interpreted seafloor conductivity. Accurate navigational information is essential.

Navigation on the seafloor was provided by an acoustic transponder net with four transponders. Such nets are typically claimed to fix absolute position to within about 50 m, and relative position to within a few meters (*e.g.* Kleinrock and Humphris, 1996). Partway through the dive series however, it became apparent that the seafloor positions established for the transponders were inaccurate. This was evident in sudden jumps of calculated position when changing reference transponder pairs. Although first-order corrections were subsequently made to the transponder coordinates, the net was not properly recalibrated as time could not be afforded for this lengthy process. Seafloor coordinates determined by Alvin's navigation program were therefore not accurate on the scale of the EM survey.

After the cruise the acoustic travel time data from the Alvin navigational log were reprocessed to improve the positional fixes. Locations were selected where all transponder signals were clearly received, and with the coordinates of one arbitrarily chosen transponder held fixed the coordinates of the other three were stepped through grids about their

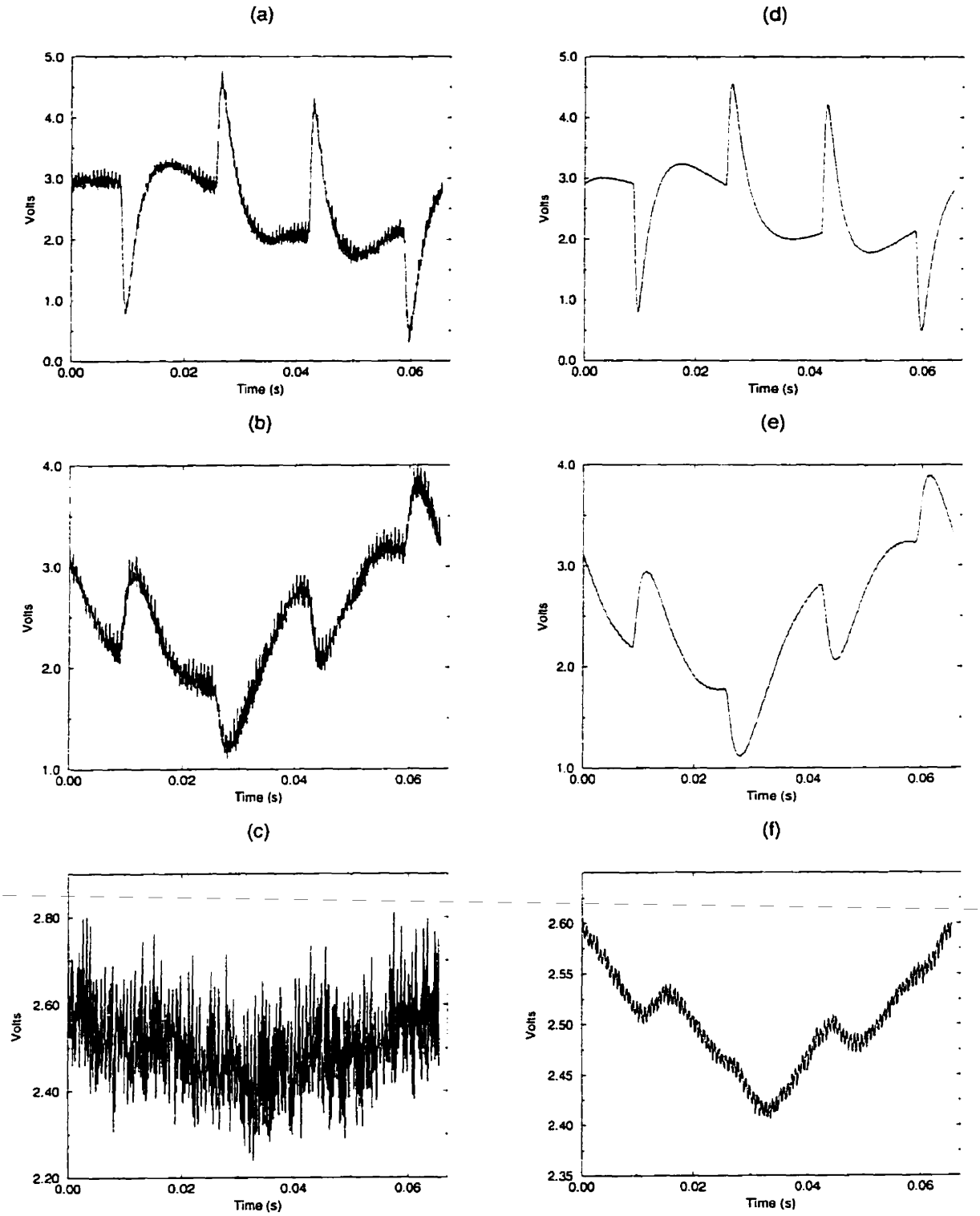

Figure 5.5: Data samples: panels (a) to (c) are samples of unstacked data, panels (d) to (f) are the corresponding 512 deep stacked data. Panels (a),(b),(d) and (e) are strong signals recorded at ranges of $\sim$ 50 m. Panels (c) and (f) were recorded at a range of 125 m, and the ratio of signal to noise from the chopper amplifiers is poor. The variation in waveforms is due to changes in relative weighting of in-line and broadside components with transmitter-receiver geometry.

estimated positions until relative coordinates were found which minimized the scatter of the submersible position calculated from each transponder pair.

The navigational data also contained discontinuities, as signals from individual transponders were frequently blocked or confused by echoes due to the rugged hydrothermal bathymetry. Transponder signals were therefore examined for consistency and continuity about each EM logging period, and one transponder pair was identified that provided relatively continuous and reliable coverage at each measurement site. This pair was used with the corrected transponder coordinates to calculate relative position throughout each transmitter cycle, and the center of Alvin's displacement vector during the logging interval taken as the relative transmitter coordinate. While using data from a single transponder pair improved the consistency of the positions, jumps of 4 to 5 m in calculated position still occured even when Alvin was stationary on the seafloor for long periods of time. This was therefore considered the threshold of noise in the positioning data.

To test the validity of the selected transponder data, Alvin's velocity was calculated over each logging period using positional fixes at the beginning and end of the cycle. The calculated direction was then compared to compass heading taken from the navigational file and found to be in good agreement.

The relative positions still had to be tied to absolute coordinates on the mound. Near the beginning of the EM survey, a logging cycle took place while Alvin was deploying ODP marker C, the position of which was determined accurately by later expeditions. This site was used as a reference point to pin the relative positions onto mound coordinates. A plot of the survey path was then rotated about this point until bathymetric observations made by analyzing the dive video and dive reports as well as depth data from the navigational log were in good agreement with a bathymetric map of the mound.

Orientation

Transmitter orientation was determined as perpendicular to Alvin's heading during logging cycles. To first order, receiver orientation was assumed perpendicular to Alvin's heading during deployment. As shifts of orientation could have occurred in the process of placing the receiver on the seafloor, however, values of $\pm 15^{\circ}$ about the nominal orientation were considered during data interpretation.

When Alvin was in motion some rotation of transmitter orientation during logging cycles was inevitable. Such rotations affect transmitter-receiver coupling by changing the ratio

of in-line to broadside field components at the receiver. Successive signal waveforms stacked together under these circumstances are not equivalent. While in theory such effects could be incorporated in modeling, the rate of rotation as a function of time could not be determined with sufficient accuracy to permit this approach. If Alvin's rotation exceeded 15° during the 34 second logging cycle, the measurement was therefore discarded. This criterion led to the rejection of 12 measurements.

Polarity Reversal

Two of the receiver files had a waveform polarity that was reversed from the expected values based on geometry. In one case, this occurred at a heat flow station where Alvin was resting on the seafloor and the geometry was constant over 4 logging cycles, yet only one of these shows the polarity reversal. For each measurement where this reversal was observed, a record in the file header of the RTC time when logging was finished confirms that the synchronization signal closely coincided with the relatively inaccurate RTC wakeup time. In each case, the receiver woke up on time to catch the synchronization pulse, while the transmitter missed it and therefore did not start transmitting until the next pulse 6.7 seconds later. A phase offset of 120 degrees was consequently introduced between the transmitted signal and the receiver stacking. As one of these anomalous measurements was at a site where three identical measurements existed, and the signal-to-noise ratio in the second was poor, both measurements were rejected.

Clock Drift

The transmitter and receiver oscillators stayed remarkably well synchronized on this dive, drifting by only 49.6 μs in 11 hours and 5 minutes, for a fractional drift of 1.26×10^{-9}! As the cumulative drift over the entire running time was only 1.5 samples, no time correction was made.

Noise and Filtering

The only noise of significance observed in the data is instrumental noise due to the chopper amplifiers. This is caused by instability in chopping/demodulating signals from the datalogger's time-processing unit due to overloading of its internal operation scheduler. The noise is constant, and its characteristics are recovered from measurements made when the signal-to-noise ratio was low. The amplitude spectrum of noise in raw and stacked data from such a measurement is shown in Figure 5.6. The frequency characteristics are well determined and fall above the signal bandwidth in almost every case (*c.f.* Appendix C). The power spectrum of each measurement's time series was therefore

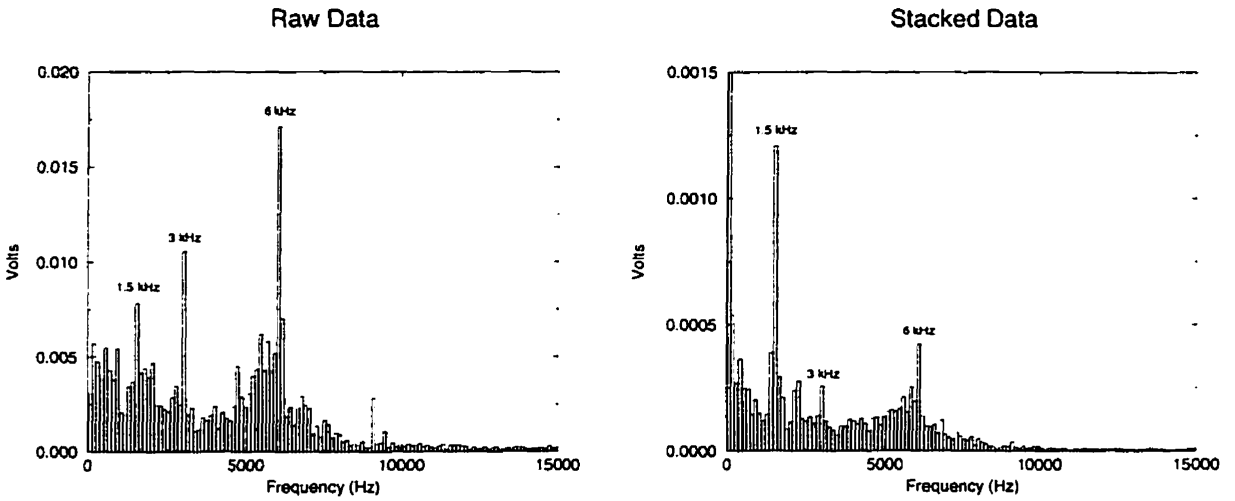

Figure 5.6: Distribution of noise due to the chopper amplifiers in raw and stacked data. The low-frequency component that can be seen in the stacked data is from the signal.

examined to estimate the signal bandwidth, and the data low-pass filtered accordingly using a cosine filter to remove noise.

Edge Selection and Data Decimation

Figure 5.7 shows a transmitter current record logged during the experiment. The first and third transitions, which occur when the current is turned on, show peaks of $\pm$ 5.4 A followed by decay to $\pm$ 4.2 A before the step-off. The initial current spike on the rising edge is due partly to the discharge of energy stored in the filter capacitors across the transmitter batteries (Figure 4.3). The following decay of transmitter current is due to polarization of the transmitter electrodes, and possibly of the battery electrodes, causing their resistance to increase with time. The second and fourth transitions, which occur when the current is turned off, are clean. Figure 5.7 also shows a sample signal logged at the receiver. The amplitude ratio of step-off to step-on transitions in the receiver signal is the same as that in the transmitter current record. This pattern is true of all the receiver data.

Any one of four steps recorded at the receiver represents a complete measurement. The clean step-off transitions, however, are easier to model. The second transition, indicated by the boxed region in Figure 5.7, was selected for fitting. This was accordingly extracted from the full data record, and logarithmically decimated to 20 pts.

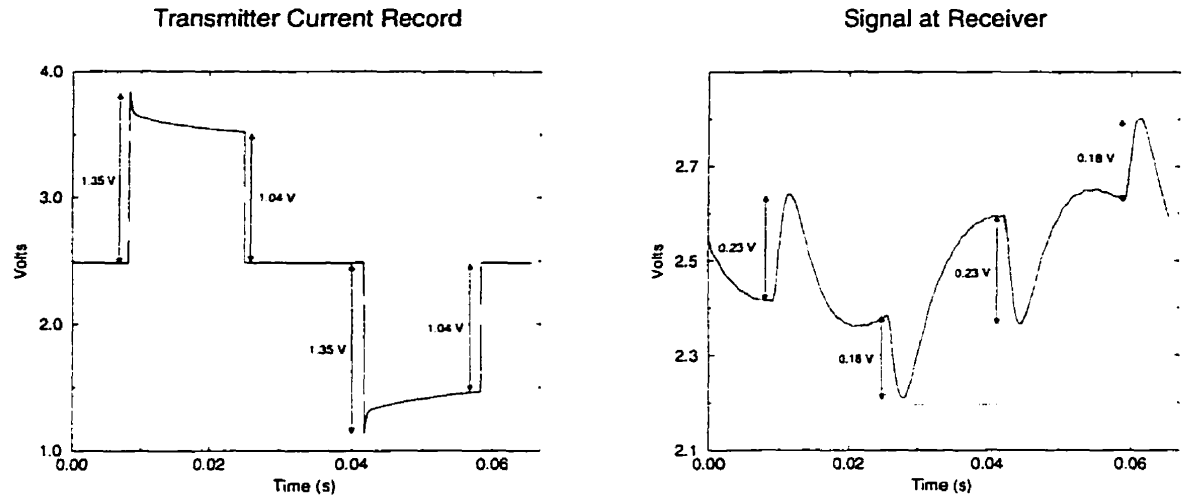

Figure 5.7: (a) Transmitter current record showing polarization effects on the source waveform. (b) The corresponding record at the receiver after filtering. Relative step size is identical at source and receiver. The second transition, identified by the boxed region, was selected for fitting.

5.7 Results

The survey, including the heat flow transect, lasted 3.5 hrs. The pull-out electrode for the free receiver component was damaged during seafloor deployment and no data were recorded on that channel. On the rigid receiver component 42 files were logged, of which 3 were offscale. Analysis of the navigational data resulted in 12 files being rejected as Alvin's bearing changed excessively during the transmission cycle, and 2 being rejected because of the polarity reversal described above. Multiple measurements were made at the heat flow sites as Alvin stayed stationary for 20-30 minutes at a time. Twenty-five interpretable measurements were thus collected at 13 sites. A summary of pre-processing results is given in Appendix C.

Chapter 6

Data Interpretation

6.1 Modeling of the Data

The data were first interpreted in terms of a double half-space model, in which seawater with a conductivity of 3.2 S/m formed the upper half-space, and a uniform seafloor of uniform conductivity the lower half-space. Free parameters in this model were the conductivity of the seafloor and a scaling variable used for small adjustments of amplitude after the model response had been normalized by the late-time amplitude of the measurement. The data were then reinterpreted using a two-layered seafloor model. Free parameters in this model were conductivity and thickness of the upper layer, conductivity of the basement layer, and the amplitude scaling variable. As no data existed on Alvin's height above the seafloor during logging cycles, a constant 3 m vertical offset of the transmitter was used in the model, based on observations made during the dive.

As discussed in Section 5.4, there was an estimated uncertainty of $\pm 15°$ in the receiver orientations inferred from Alvin's heading during deployment, and an error in position of about 5 m based on jumps in the transponder travel time data when Alvin was stationary on the seafloor as well as Alvin's motion during many of the logging cycles. Bottom speed when Alvin was in motion was about 0.2 m/s, resulting in a $\sim$7 m displacement during logging cycles. Furthermore there was clearly error associated with the transmitter orientation inferred from Alvin's bearing, due to both Alvin's rotation during logging cycles and bending of the transmitter dipole due to drag from the seawater during rotation. Based on the assumption that errors in position and transmitter orientation would average to zero, the entire data set was inverted in terms of the double half-space model for receiver orientations varying $\pm 15°$ in $5°$ steps about the nominal orientation with

range and transmitter orientation held fixed at their nominal values. The receiver orientation which minimized error of fit over the entire data set was retained, and individual measurements were processed with receiver orientation fixed at this value.

An attempt was then made to model the data using the double half-space model with range, polar angle and transmitter angle allowed to float within bounds of $\pm 10\%$, $\pm 15°$ and $\pm 15°$ respectively. While this approach generally resulted in better fits of the data than could be found with the navigational parameters fixed at their nominal values, the seafloor apparent conductivities in the two cases differed little, being primarily determined by the arrival time of the signal rather than its shape. For several stations, however, notably those located on the far side of the black smoker complex from the receiver, the navigational parameters would drift to their extreme limits, which were considered improbable. The location of these stations suggested that signals from these sites were distorted by the black smoker complex, and that the drift in navigational parameters reflected dimensional inadequacy of the model rather than error in position and transmitter orientation. This approach was consequently abandoned and navigational parameters were fixed at their nominal values in the final analysis.

Fitting of models to the data was accomplished using the Downhill Simplex method (Press *et al.*, 1992; Nelder and Mead, 1965) to search the parameter space. This is a non-derivative optimization method (zero order method) which minimizes an objective error function, defined in this case as the RMS error of fit between model response and filtered data at 20 logarithmically spaced points in time. The forward model response consisted of the transmitter current waveform convolved with the model's impulse response and the receiver transfer function. During each iteration, model in-line and broadside impulse responses were computed at logarithmically spaced points in time and projected onto the receiver orientation, giving a combined impulse response which was splined to the same sample interval as that at which the data were recorded. This was convolved in the time domain with the record of the transmitter signal logged through the receivers prior to the experiment (Figure 5.1), giving the model response. The part of the response corresponding to the second transition was then decimated logarithmically to 20 pts, its amplitude normalized by the late-time amplitude of the data, and then adjusted slightly with the scaling variable mentioned above. The RMS error of fit between model response and data determined the direction of the next step in parameter space according to the Downhill Simplex algorithm. The inversion was stopped when convergence conditions were achieved, namely that the fractional change in the RMS error between successive steps was below 0.001.

Once an acceptable model was found, it was necessary to know how well the data constrained the model. This depended on sensitivity of model parameters to the measurements, errors on observed parameters, and the level of fit. Noise in the stacked and filtered electric field measurements was considered negligible, but error in navigational parameters and inappropriateness of the one-dimensional model for fitting measurements influenced by three-dimensional structures were of concern. Due to the difficulty of propagating errors in all the navigational parameters to errors in the data, only error in range was considered. While the significance of this simplification varies between measurements with transmitter-receiver coupling, changes in angles have impact primarily on the goodness of fit, influencing model conductivity to a much lesser extent, as the latter is determined principally by arrival time. Error in conductivity, the parameter of interest, is most sensitive to error in range.

An error in range of 10% was used in the calculation, corresponding at shorter ranges to the 5 m jumps in navigational fixes observed when Alvin was stationary on the seafloor, and at longer ranges being more conservative. (In retrospect, a fixed error of 5 m at all positions might have been more appropriate). Range was accordingly perturbed by -5% with other model parameters fixed at the values reached by the inversion. As signal strength falls off with the inverse cube of range, the -5% perturbation guaranteed a more conservative error estimate than a +5% perturbation. The residuals of the forward model response at the perturbed position relative to the data were then used as a coarse estimate of the uncertainty in electric field data.

This estimated measurement error vector was then propagated to error in model parameters through eigensolution analysis as proposed by Vozoff and Jupp (1975) and further described by, for example, Edwards, Bailey and Garland (1981), Nobes (1984), Cheesman (1989), and Edwards (1997). A Jacobian matrix of datum sensitivities to small variations in model parameters was calculated numerically using a 5% forward perturbation of the logarithms of model parameters. Each element of the Jacobian matrix was then normalized by the corresponding element of the electric field error vector, rescaling the units of the datum so that its standard error was unity. Following eigenvalue decomposition of the Jacobian, standard errors in the eigenparameters were converted to coarse upper bounds for the errors in the model parameters as described by Cheesman (1989).

Sensitivity kernels were then computed for the final models using the method described in Section 3.4. To properly reflect the effect of signal strength on measurement quality and hence resolving ability, the sensitivity$\times$ depth function in this case was not normalized

by the DC field, and was therefore defined as

$$\frac{\delta E(x,0,z,t)}{\delta(log\,\sigma)\delta(log\,z)}. \tag{6.1}$$

Double half-space modeling results are summarized in Table 6.1, and are shown on a map of the mound in Figure 6.1. Layered seafloor modeling results are summarized in Table 6.2. In-line and broadside weights in Table 6.1 indicate the contribution of a unit transmitter dipole source for each configuration when projected onto the receiver orientation. Weighting of each component can range from -1 to 1. The amplitude of the linear combination of these weights indicates the efficiency of transmitter-receiver coupling, and can range from 0 to 1. Root-mean-square errors in both tables were calculated relative to the unfiltered data, and are normalized by a noise figure of 0.008 V obtained by inspection of the stacked measurements. This choice of normalization was made so that the RMSE values given reflect the degree to which the model fits the unprocessed data. A RMSE value of 1 or less therefore indicates that the model fits the data to within the noise level in the measurement. Station numbers refer to locations indicated in Appendix C, and shown in Figure 5.4.

Model responses of the best-fitting double half-space models are plotted against the data in Appendix D, and those for the layer over a half-space model are plotted in Appendix E. Sensitivity×depth functions for the best-fitting half-space models for each station are shown in Figures 6.2 to 6.5, plotted at times selected to bracket the arrival times observed in the data, corresponding to the quarter period (one transition) of the transmitter signal divided by 50, 10, 5 and 1.

6.2 Discussion

The data are generally well fit using a uniform seafloor model. Data from stations 4, 5, 7, 11, 12 and 13 are fit to the level of measurement noise, while data from stations 2, 3, 8, 9 and 10 are less well fit. The presence of Alvin beside the transmitter is unlikely to account for such misfits. As the cylindrical metal part of Alvin's hull is anodized, and therefore highly resistive, its effect on the signal is small. The positions of the stations where fits are poor are, however, noteworthy. Stations 2, 3, 8 and 9 are all on the far side of the black smoker complex from the receiver, and station 10 is in the Kremlin zone amid active chimneys and diffuse flow. This suggests that the data from these stations contain

Station	Slant Range (m)	Rel. Depth (m)	In-line Weight	Broadside Weight	σ_1 (S/m)	$\pm$ (S/m)	RMSE Model
1	49	-3	-.097	-.727	3.6	0.7	2.13
2	67	6	-.351	.626	5.2	1.0	3.59
3	52	2	-.298	.590	5.1	1.0	6.90
4	82	23	-.181	.572	15.9	3.1	1.05
5	75	21	.676	.305	6.2	1.2	0.87
6	71	15	.402	-.315	2.3	0.5	1.86
7	69	10	-.898	.069	4.1	0.8	0.78
8	56	5	.041	-.220	11.6	2.3	2.27
9a	52	1	.136	.559	1.6	0.3	9.11
9b	52	1	.136	.559	1.4	0.3	11.86
9c	52	1	.136	.559	1.3	0.2	12.68
10	50	6	.831	-.074	6.7	1.3	4.22
11a	66	14	.845	.046	4.9	1.0	0.98
11b	66	14	.845	.046	4.9	1.0	0.90
11c	66	14	.845	.046	4.8	1.0	1.04
11d	66	14	.845	.046	4.8	1.0	1.06
12a	90	12	.023	-.122	4.7	0.9	0.57
12b	90	12	.023	-.122	4.7	0.9	0.72
12c	90	12	.023	-.122	4.7	0.9	0.71
12d	90	12	.023	-.122	4.7	0.9	0.64
12e	90	12	.023	-.122	4.8	1.0	0.77
13a	124	19	.903	-.097	3.4	0.7	0.68
13b	124	19	.903	-.097	3.2	0.6	0.66
13c	124	19	.903	-.097	3.3	0.6	0.91
13d	124	19	.903	-.097	3.2	0.6	0.69

Table 6.1: Summary of modeling results for a uniform seafloor model. Columns 4 and 5 scale the projection of in-line and broadside components onto the receiver orientation. Each of these can vary from +1 to -1 while their vector combination has an amplitude between 0 and 1, indicating the efficiency of transmitter-receiver coupling. Station locations are as indicated in Figure 5.4.

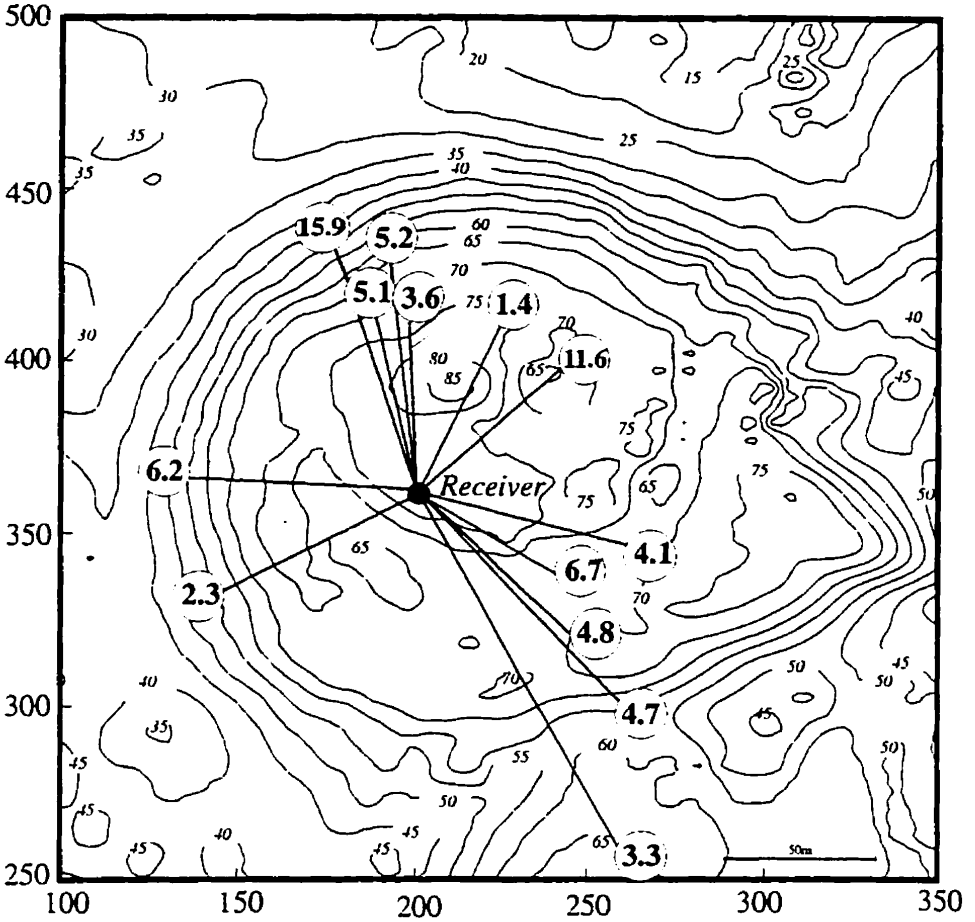

Figure 6.1: Map of the TAG mound with homogeneous sea-bed modeling results. Values in circles are apparent conductivities in S/m obtained from modeling the data from survey stations shown in Figure 5.4.

Station	σ_1 (S/m)	$\pm$ (S/m)	h_1 (m)	$\pm$ (m)	σ_2 (S/m)	$\pm$ (S/m)	RMSE
1	3.6	1.5	12.8	12.9	1.2	0.2	1.91
2	5.3	3.5	4.0	1.8	6.5	7.1	3.48
3	4.8	0.8	3.3	5.5	5.8	0.4	6.86
4	35.1	24.9	1.0	1.5	9.1	1.6	0.71
5	6.4	1.2	12.1	1.5	5.9	1.1	0.86
6	2.7	0.4	12.0	5.3	1.9	0.4	1.77
7	3.1	0.6	11.7	1.5	3.9	0.7	0.80
8	11.0	0.6	12.1	8.3	10.8	4.7	2.23
9a	4.0	4.4	4.5	15.3	0.7	1.5	8.07
9b	2.0	0.4	19.3	2.8	1.0	0.1	6.06
9c	1.8	0.3	20.5	2.8	0.2	0.02	5.89
10	11.7	3.8	3.0	4.6	6.0	0.3	2.52
11a	5.1	0.5	5.1	1.3	4.9	0.8	0.97
11b	5.2	0.8	7.1	1.2	4.7	0.8	0.89
11c	6.0	1.0	10.3	1.7	3.8	0.6	0.97
11d	5.6	1.0	9.6	1.7	4.3	0.7	1.01
12a	4.8	0.9	9.4	2.5	4.4	0.7	0.57
12b	4.8	0.9	9.6	4.3	4.4	0.4	0.72
12c	5.1	0.9	16.0	2.3	1.6	0.2	0.70
12d	5.7	1.2	9.3	3.7	4.2	0.7	0.60
12e	4.9	0.9	9.4	3.0	4.4	0.6	0.72
13a	3.7	0.3	14.4	7.3	3.1	0.2	0.68
13b	3.5	0.6	17.5	4.0	2.8	0.4	0.66
13c	3.7	0.6	12.2	4.8	3.0	0.4	0.91
13d	3.5	0.5	15.6	4.7	3.0	0.4	0.69

Table 6.2: Summary of modeling results for a seafloor modeled as a layer over a half-space. Range and relative depth for each station are as given in Table 6.1 in which weighting of in-line and broadside components in the measurement are also listed. Station locations are as indicated in Figure 5.4.

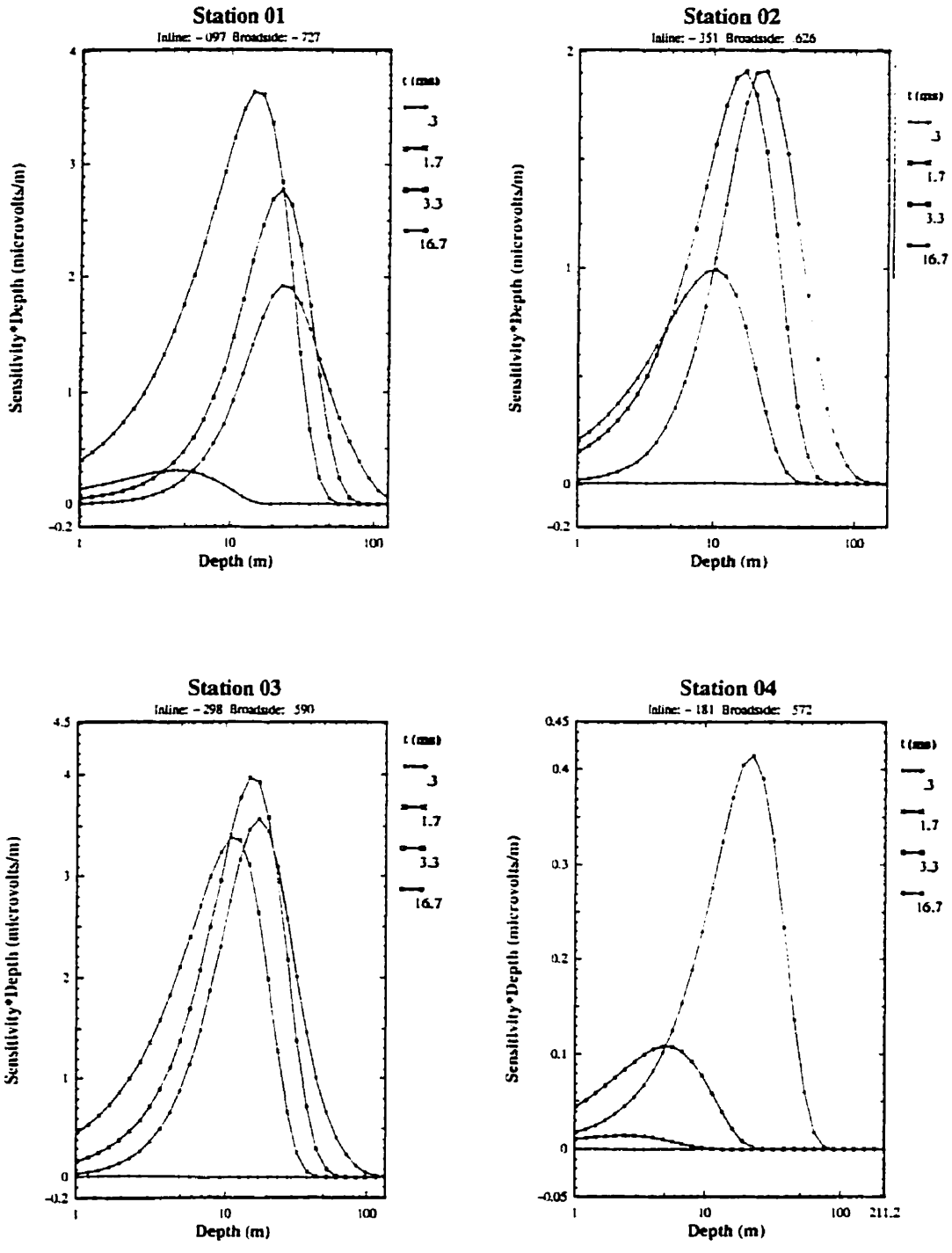

Figure 6.2: Sensitivity × depth for measurements from stations 1 to 4. Plotted at times corresponding to the quarter period of the transmitter signal divided by 50, 10, 5 and 1.

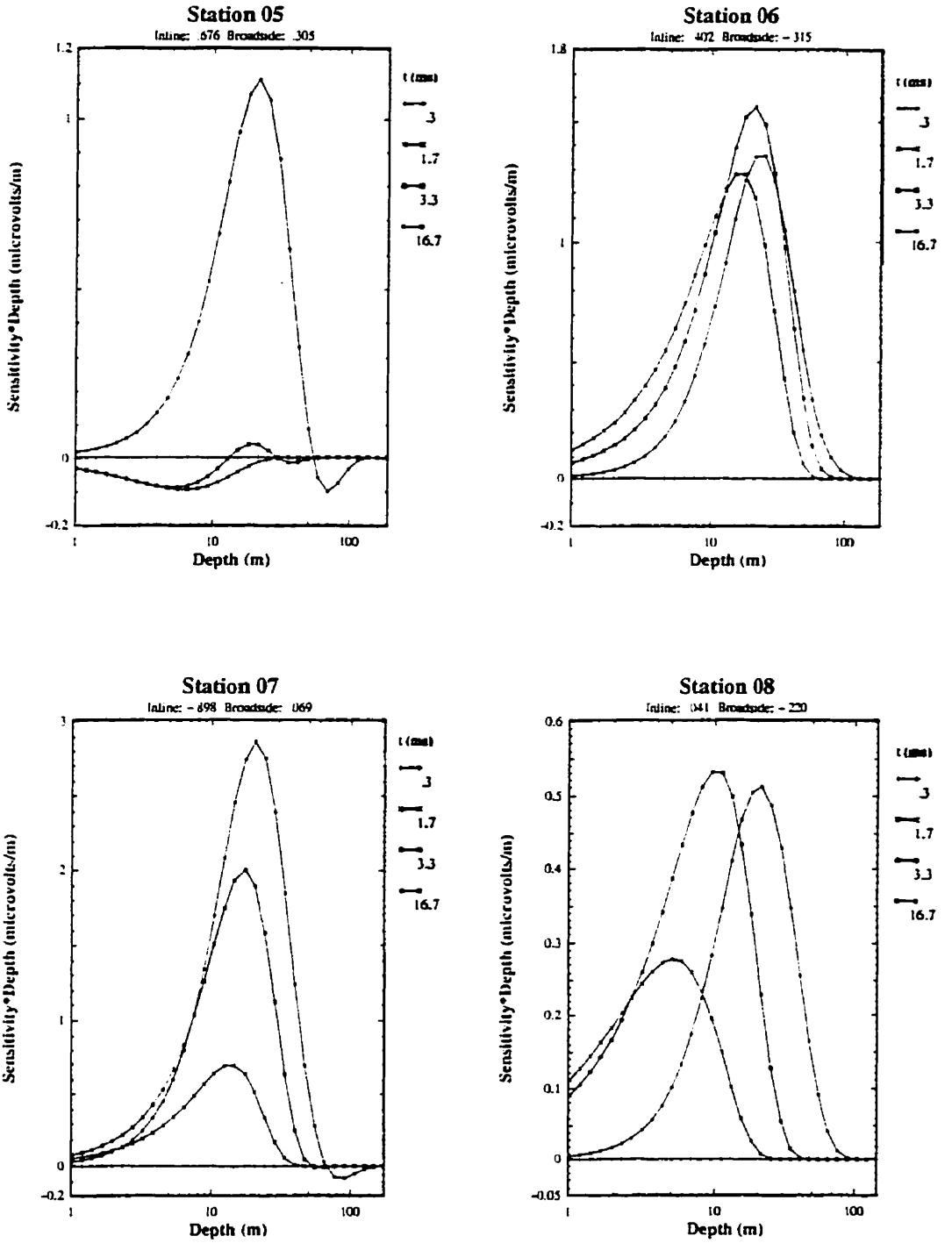

Figure 6.3: Sensitivity × depth for measurements from stations 5 to 8. Plotted at times corresponding to the quarter period of the transmitter signal divided by 50, 10, 5 and 1.

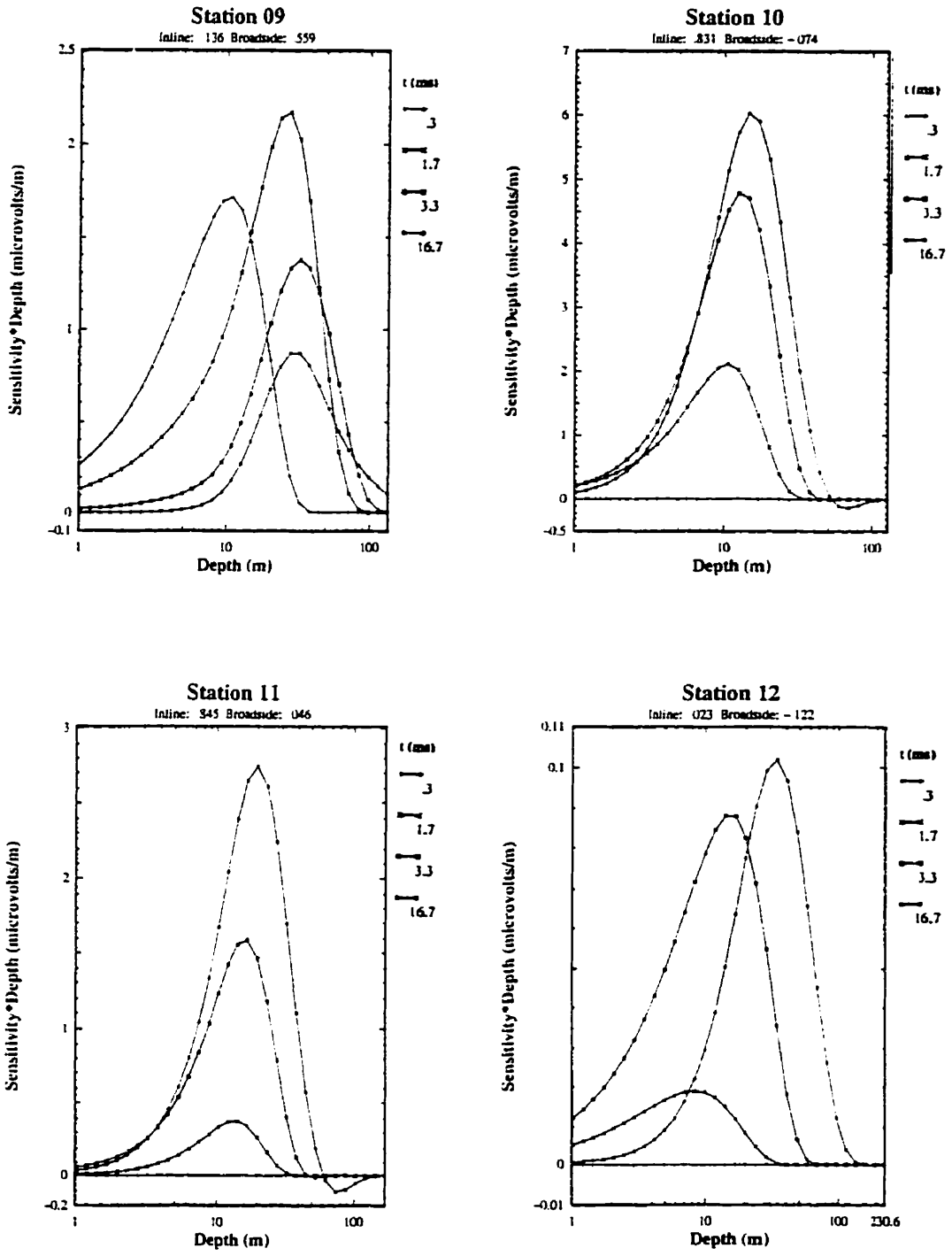

Figure 6.4: Sensitivity × depth for measurements from stations 9 to 12. Plotted at times corresponding to the quarter period of the transmitter signal divided by 50, 10, 5 and 1.

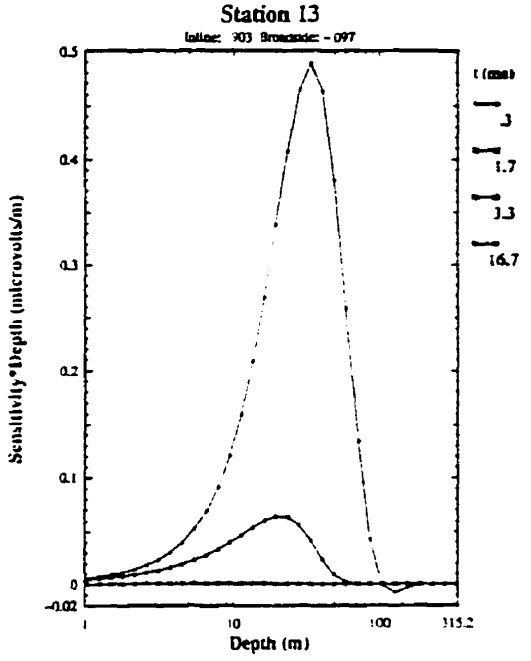

Figure 6.5: Sensitivity × depth for measurements from stations 13. Plotted at times corresponding to the quarter period of the transmitter signal divided by 50, 10, 5 and 1.

the signature of high-temperature fluid networks as discussed in Chapter 3. A pattern common to most of the fits is that the rise time of the recorded data is faster than that of the best-fitting half-space model, which suggests layering. One possible explanation for this was that the transmitter was a few meters off the seafloor when Alvin was in motion, although this was partially compensated for by the 3 m vertical offset of the transmitter in the modeling. It also agrees, however, with general knowledge of mound geology in which a crust of fine-grained partially oxidized sulfide particles which have settled from the plume forms the upper few meters.

Using a two-layered seafloor model, a small improvement of fit is seen at all stations. The significance of this improvement could theoretically be determined using an F-test as described by Menke, 1984. This test is difficult to apply in practice, however, as we do not know the degrees of freedom in the measurements and errors are correlated. Marked improvements of fit are observed only for measurements 9b and 9c and at station 10. At all but two stations the best-fitting models show a decrease in conductivity with depth, the upper layer being generally about 12 to 20 m thick. It is tempting to accept this result as it accords with ODP drill results (Humphries *et al.*, 1995). The eigensolution error

analysis suggests that this would be an overinterpretation of the data. In most cases, upper and lower layer conductivities fall within each other's error bounds, indicating that the layered model cannot unambiguously be distinguished from a uniform seafloor model. Error analysis does show a clear distinction between layers in the models used to fit measurements from stations 9b, 9c, 10 and 12c, yet none of these results appear dependable. The conductivities of the lower layers in 9b and 9c do not fall within each other's error bounds; the uncertainty in thickness of the upper layer at station 10 is greater than the layer's thickness; and the result from 12c where the data were already fit to the noise level using a uniform seafloor model is unsupported by results from four identical measurements at the same site. Accordingly, none of the layered seafloor models can be accepted with confidence and further interpretation is based conservatively on the results of modeling with a uniform seafloor model.

As the data modeled are linear combinations of in-line and broadside components weighted as shown in Table 6.1, measurement sensitivities share characteristics of those for each component. The measurements from stations 1 to 7 and 10 and 11 appear to be most sensitive to structure over a depth of roughly 10 to 30 meters below the seafloor. Due to a high apparent conductivity, the measurement from station 8 is influenced by shallower structure. Apparent conductivity at station 9 is low and this, combined with a heavy weighting of the broadside component, gives the measurement from that site a broad sensitivity over time and depth. Stations 12 and 13 are relatively far from the receiver, and data from those sites accordingly reflect deeper structure than do those from the other sites.

Apparent conductivities from Table 6.1 range from 1.4 to 15.9 S/m, being generally higher than the 3.2 S/m of seawater. The values are grouped about a median of 4.7 S/m, with a standard deviation of 3.1 S/m. As the data are primarily sensitive to structure 10 to 30 mbsf, we associate the median value with the general background of sulfide breccia observed in the upper 15 to 30 m of the mound during ODP drilling (Humphries *et al.*, 1995). This agrees with seafloor sulfide conductivities of 2-5 S/m reported by Francis (1985). While small variations about this mean are insignificant artifacts of geologic and measurement noise, apparent conductivities are observed which depart sufficiently from this mean to require explanation.

The model for station 4 on the northern edge of the mound has a surprisingly high conductivity. Measurement quality from this station is good: transmitter orientation was stable as Alvin was stationary on the seafloor, transmitter-receiver coupling was high and

the signal is strong. While the vertical offset at this site is considerable, the use of slant range in modeling the data accounts for this to first order. A possible explanation of the high conductivity is accumulation at the foot of the slope of fine-grained pyrite particles from the black smoker plume. Sensitivity analysis suggests otherwise, indicating that the measurement is primarily sensitive to structure at a depth of about 20 m. The location on the far side of the black smoker complex from the receiver makes it more plausible that the high apparent conductivity reflects diffusion of the signal through regions of the mound where temperature has been elevated by the hydrothermal fluid feeder network. Presence of the latter is supported by difficulties in fitting data from stations 2 and 3. Assuming that the feeder network becomes more focused as it approaches the surface, its imprint on measurements from stations 1, 2 and 3 would be that of a localized conductive region whereas at the depths to which the measurement from station 4 is sensitive a dispersed fluid network would raise the bulk conductivity of the mound. Accordingly, while data from stations 2 and 3 are poorly fitted, the bulk conductivity indicated by the matching arrival time is characteristic of the surrounding sulfide breccia, and data from station 4 are well fitted by a model with a high apparent conductivity.

Results from stations 5 and 6 on the western side of the mound show a moderate contrast in conductivity. Despite good transmitter-receiver coupling and similar ranges in the two cases, the signal from station 5 is weak while that from station 6 is solid. Sensitivity modeling suggests that the measurements from both sites are heavily weighted by response from structure over a depth range of 10 to 30 m. The lower conductivity observed at station 6 is unlikely to be due to the presence of anhydrite, as heat flow over this region of the mound is low (Becker *et al.*, 1996) and subsurface temperatures unlikely to be sufficiently high for anhydrite deposition. Gravity measurements by Evans (1996) as well as ODP drill results indicate that the mound is draped over the border of a platform in the basalt substrate, the edge of which occurs in the vicinity of stations 5 and 6. It is therefore probable that the low conductivity at station 6 reflects the influence of this resistive substrate.

A marked contrast is observed in apparent conductivities for stations 8 and 9 in the north-east quadrant of the mound. The high value for station 8 was initially interpreted as indicating a region of subsurface focusing of hydrothermal fluids. This interpretation received support a year after our survey when new black smoker activity was observed in the depression where this measurement was made (Evans, personal communication). The data from station 9 are poorly fit using a uniform seafloor model. Station 9 is located directly across the central black smoker complex from the receiver, and three-

dimensional effects are almost certainly involved. Despite high error of fit, the inversion result indicating a resistive path for diffusion remains broadly valid as the arrival time of the signal is matched although its shape is not. While initially puzzling, the presence of such a path was explained when ODP drilling revealed an abundance of anhydrite in this region. The black smoker complex is thought to be surrounded by a collar of resistive anhydrite, providing a fast path for near-surface transient diffusion around the high-temperature vents. This may also account for the relatively low conductivity at station 1 relative to stations 2 and 3.

Stations 7, 10 and 11 are on the south-eastern terrace in the Kremlin zone. Apparent conductivities from stations 7 and 11 are roughly equal to the background value assigned to brecciated sulfides. A somewhat elevated apparent conductivity is observed at station 10 which is attributed to its location amid shimmering waters and chimneys venting intermediate temperature fluids.

Station 12 is located at the south-eastern edge of the mound. Sensitivity analysis suggests that measurements from this site are primarily influenced by structure over a depth range of 10 to 50 m. While the basalt basement known to underlie this region should therefore influence the measurement, low absolute sensitivity and a poor signal-to-noise ratio make such effects ambiguous. It is worth noting, however, that the layered seafloor model for station 12c indicates a 16 m thick layer of sulfides overlaying a resistive basement which accords closely with what is known of the stratigraphy from ODP drilling.

Station 13 is located off the mound on pillow basalts. Modeling by Evans and Everett (1994) and by Yu and Edwards (1996) suggests that under such circumstances transient measurements are insensitive to mound structure as the signal recorded at the receiver is dominated by the seawater arrival. It is therefore reassuring that models used to fit the measurements from this station converge to the conductivity of seawater.

6.3 Conclusions

Measurements from half of the survey sites are well fit using a uniform seafloor model. Poor fits to data from the remaining stations suggests that three-dimensional regions of anomalous conductivity thought to be associated with hydrothermal fluid convection have left an imprint on the signal which cannot be duplicated with a uniform seafloor model. While the presence of such regions can be inferred qualitatively, neither the data set nor current modeling software are adequate for a quantitative interpretation. There

is a general ambiguity between heterogeneity in the structural matrix and conductivity variations related to hydrothermal fluid convection. The distinction is more readily made for extremes of high or low conductivity than for intermediate values: conductivities below that of seawater cannot be attributed to the fluid regime, while apparent conductivity above about 5-6 S/m is unlikely to reflect characteristics of the rock matrix.

On the basis of apparent conductivity, the TAG mound appears to have considerable structural heterogeneity. Apparent conductivities range from 1.4 to 15.9 S/m, showing a broad distribution about a median of about 5 S/m which we associate with the lens of massive pyrite breccia by comparison of depth of investigation inferred from sensitivity analysis and ODP drill results.

Chapter 7

Conclusions

7.1 Conclusions

The long-term goal of our research is the development of tomographic imaging techniques to probe the subsurface structure of seafloor hydrothermal mounds. This is a work in progress, and the TAG survey should be viewed as a pioneering step towards achieving this end. It was the first trial of the instruments and the first test of our proposed survey method. The survey accordingly suffered a number of shortcomings. Some of these were beyond our control, such as damage to the second receiver component during deployment on the seafloor and problems of navigation. Others, such as difficulties with the amplifiers and the loss of data due to excessive submersible motion, led to subsequent modification of the instruments and of our survey methodology.

The TAG experiment was successful in validating the feasibility of our approach by demonstrating that submersible-based transient electromagnetic measurements are capable of rapid acquisition of reliable data on the conductivity of seafloor mounds. The data set collected on a single receiver component in the space of a few hours remains the most comprehensive available to date on *in situ* conductivities typical of such environments. Apparent conductivities of the mound determined by modeling the data range from 1.4 to 15.9 S/m, showing considerable heterogeneity. While uncertainty in navigational parameters places large error bars on these results, the distribution of conductivity inferred from the data is in general accordance with our knowledge of mound geology. Evidence of distortion by three-dimensional features suggests that imaging of such regions may be achieved once suitable interpretive software is developed.

The story of this thesis would be incomplete without a brief description of the unsuccessful

measurement campaigns which have occurred since the TAG survey. These illustrate the adversity of conditions under which data such as those described in the foregoing chapters are collected, and lead to conclusions of practical import to future surveys.

In the fall of 1993, an experiment was conducted from R/V Melville to measure sediment thicknesses in Middle Valley on the East Pacific Rise. The experiment was performed from the surface ship, two receivers being dropped with buoyancy packages which permitted them to return to the surface autonomously. A powerful shipboard transmitter was used which transmitted through a 100 m long electric dipole towed along the seafloor behind the ship. Two deployments were attempted. On the first, a break developed in the transmitter cable. Immediately prior to the second, the battery packs on both receivers mysteriously developed short circuits.

New battery packs and amplifiers were developed over the winter of 1993/1994, and in July 1994 an experiment was conducted from CSS John P. Tully at the Magic Mountain hydrothermal site on the Juan de Fuca ridge using the ROPOS remotely operated submersible. Adverse weather conditions prevented deployment of ROPOS on all but three days out of two weeks at sea, and this dive time was shared with other researchers. As the hydrothermal mound could not be located within the first two days of dive time, the planned experiment was modified to one of measuring sulfide thicknesses at a site which later turned out to be near the base of Magic Mountain. While excellent quality electromagnetic measurements were made (examples in Appendix B), the transponder network which was part of the ROPOS system was inoperative throughout the dive and the data cannot be interpreted with any confidence due to lack of positional information.

We returned to Magic Mountain in July of 1995 with an almost identical result. Adverse weather conditions again prevented deployment of ROPOS on all but a few days out of two weeks of ship time, and the transponder network was again inoperative. Positioning on the seafloor was estimated by range measurements on the ROPOS cage. As this was swinging at the end of a 1.8 km long tether by more than the scale of the experiment, position estimates were poor and the data were consequently offscale.

In October and November of 1995, a calibration experiment was conducted in Schwartz Bay of Saanich Inlet on Vancouver Island, where the instruments were deployed in 30 m of water from a small research vessel. One instrument was laid on the seafloor transmitting into a 175 m long cable marked by floating buoys at each end, while a receiving instrument was moved by the ship to stations about this source. This was the first time that the instruments were deployed in an environment where noise due to sferics and power lines

was significant. After initial difficulties, a stacking algorithm designed to cancel 60 Hz noise and its harmonics was developed, and excellent electromagnetic measurements were collected against a high background noise level (examples in Appendix B). Unfortunately the differential GPS signal relied on for positioning could not be received, and the non-differential GPS data consequently recorded has an error comparable to the scale of the experiment. Without knowledge of either relative position or receiver orientation on the seafloor, the data cannot be interpreted.

In November 1996 an experiment was scheduled in the Sea of Japan to survey methane hydrate deposits. Two receivers were to be deployed from the ship while a transmitting dipole driven by a shipboard transmitter was towed about them in a manner similar to that used in the Melville survey of 1993. The planned experiment was aborted when a typhoon forced the ship into harbor. The instruments were instead deployed at short notice in shallow water of Nagoya Bay but the amplifier gain setting, selected for a deep water environment, was too high for shallow coastal waters. Noise from sferics and power lines drove the measurements offscale. Navigational data from this experiment was also poor.

As a footnote it is worth mentioning that the ROPOS submersible was lost at sea during a storm in the fall of 1996.

General conclusions drawn from these experiences are as follows:

1. Precise relative positional information is essential to the interpretation of electromagnetic travel time data on the scale of our surveys. Navigational systems have proved inadequate to varying degrees in every experiment, and a great deal of data has been either lost or rendered uninterpretable as a consequence. While navigational systems are generally not the responsibility of scientific personnel on research vessels, every possible measure must be taken to ensure their dependability.

2. Targets should be selected which are located in calm waters.

3. Deep water targets are preferable due to the lower levels of ambient noise. When measurements are to be made in shallow coastal waters, more than one deployment should be planned. Amplifier gain should be set low on the first deployment, the purpose of which is primarily observation of ambient noise levels.

4. Increasing the dynamic range of the receivers would provide a relatively inexpensive margin of protection against measurements going offscale. This could be accom-

plished using variable gain amplifiers controlled by the data loggers in a feedback loop, or by changing the data logger ADCs to ones with higher resolution.

7.2 Summary of Original Contributions

The original contributions made by this thesis are as follows:

1. A short-baseline marine transient electric dipole-dipole system was developed for measuring seafloor conductivities.
2. A submersible-based survey methodology was developed for seafloor conductivity surveys using these instruments.
3. The first electromagnetic soundings of a seafloor hydrothermal deposit were made on the TAG active mound, on the Mid-Atlantic Ridge.
4. The data from the TAG survey were interpreted in the context of TAG geology.

7.3 Suggestions for Further Work

Instruments

The instruments in their current version have proved reliable as minor problems encountered in early deployments have already been corrected. Only two modifications are suggested at present. As mentioned above, an increase in dynamic range of the receivers is recommended to provide a broader margin of protection against measurements going offscale. Developing a method of measuring instrument orientation on the seafloor is also suggested to reduce ambiguities in data interpretation.

For submersible-based surveys, the possibility of running a transmitter from the submersible's power is an attractive option. This would deliver signal strengths suitable for longer range measurements, such as would be required for sounding stockwork structure beneath hydrothermal mounds. Not needing batteries, transmitters designed for this purpose would be sufficiently compact to be mounted on the submersible without interfering with other experiments, allowing extensive electromagnetic data sets to be collected peripherally.

Data Interpretation

While the one-dimensional models used to interpret the TAG data are a poor approximation of the actual situation, inversion algorithms capable of resolving three-dimensional structure from a sparse transient data set are not yet available. Accurate computation of the fields of such structures is computationally prohibitive, but approximate models based on vortex currents at early time and current channelling at late time may provide first order estimates of the characteristics of three-dimensional features.

Although a comprehensive data set has not yet been collected, our capacity to do so presently exceeds our capability of using such measurements to their full potential. Tomographic imaging of a mound's inner structure cannot be accomplished by processing measurements individually. Inversion algorithms which process transient measurements simultaneously to constrain a three-dimensional model must be developed for this purpose.

Interpreting data only as far as apparent conductivity is not very satisfying. The geologist is interested in the individual parameters of porosity, rock composition, and fluid temperature distribution, whereas conductivity is a function of these parameters in combination. Unfortunately, the extreme heterogeneity of the hydrothermal environment makes it difficult to apply a priori constraints to any of the parameters. This suggests that EM data be interpreted in conjunction with that from other methods, such as heat flow and gravity. Steps are presently being taken in this direction. Yang *et al.* (1996) have developed a model for hydrothermal flow in a TAG-like structure, and a seafloor gravity meter is currently under development.

References

Accerboni, E. & Mosetti, F., 1967. A physical relationship among salinity, temperature and electrical conductivity of sea water, *Bol. Geof. Teor. Appl., 9*, 87-96.

Archie, G.E., 1942. The electrical resistivity log as an aid in determining some reservoir characteristics, *Trans. A.I.M.E., 146*, 54-62.

Backus, G. & Gilbert, F., 1968. The resolving power of gross earth data, *Geophys. J. R. astr. Soc., 16*, 169-205.

Ballard, R.D., Francheteau, J., Juteau, T., Rangan, C. & Normark, W., 1981. East Pacific Rise at 21° N: the volcanic, tectonic, and hydrothermal processes of the central axis, *Earth Pl. Sci. Lett., 55*, 1-10.

Bannister, P.R., 1968. Determination of the electrical conductivity of the seabed in shallow waters, *Geophysics, 33*, 995-1003.

Becker, K., Von Herzen, R.P., Francis, T.J.G., Anderson, R.N., Honnorez, J., Adamson, A.C., Alt, J.C., Emmermann, R., Kempton, P.D., Kinoshita, H., Laverne, C., Mottl, M.J. & Newmark, R.L., 1982. *In situ* electrical resistivity and bulk porosity of the oceanic crust Costa Rica Rift, *Nature, 300*, 594-598.

Becker, K., Von Herzen, R., Kirklin, J., Evans, R., Kadko, D., Kinoshita, M., Matsubayashi, O., Mills, R., Schultz, A. & Rona, P., 1996. Conductive heat flow at the TAG active hydrothermal mound: Results from 1993-1995 submersible surveys, *Geophys. Res. Lett., 23*, 23, 3463-3466.

Bonatti, E., 1975. Metallogenesis at oceanic spreading centers, *Annual Review of Earth and Planetary Sciences, 3*, 401-431.

Cann, J.R. & Edmond, J., 1988. Sub-seafloor water-rock interactions, *The Mid-Oceanic Ridge - A Dynamic Global System*, National Academy Press.

Chave, A.D., 1983. Numerical integration of related Hankel transforms by quadrature and continued fraction expansion, *Geophysics, 48*, 12, 1671-1686.

Chave, A.D., 1984. The Fréchet derivatives of electromagnetic induction, *J. Geophys. Res., 89*, B5, 3373-3380.

Chave, A.D., 1988. Electromagnetic methods in mid-ocean ridge studies, *The Mid-*

Oceanic Ridge - A Dynamic Global System, National Academy Press.

Chave, A.D. & Cox, C.S., 1982. Controlled electromagnetic sources for measuring electrical conductivity beneath the oceans, 1., forward problem and model study, *J. Geophys. Res.*, *87*, 5327-5338.

Cheesman, S.J., 1989. A short baseline transient electromagnetic method for use on the sea floor, Ph.D. thesis, University of Toronto.

Cheesman, S.J., Edwards, R.N. & Chave, A.D., 1987. On the theory of sea floor conductivity mapping using transient EM systems, *Geophysics*, *52*, 204-217.

Cheesman, S.J., Edwards, R.N. & Law, L.K., 1990. A test of a short-baseline sea floor transient electromagnetic system, *Geophys. J. Int.*, *103*, 431-437.

Cheesman, S.J., Law, L.K. & Edwards, R.N., 1991. Porosity determinations of sediments in Knight Inlet using a transient electromagnetic system, *Geo-Marine Lett.*, *11*, 84-89.

Cheesman, S.J., Law, L.K. & St. Louis, B., 1993. A porosity mapping survey in Hecate Strait using a seafloor electro-magnetic profiling system, *Marine Geology*, *110*, 245-256.

Coggon, J.H. & Morrison, H.F., 1970. Electromagnetic investigation of the seafloor, *Geophysics*, *35*, 476-489.

Corliss, J.B., Dymond, J., Gordon, L.I., Edmond, J.M., von Herzen, R.P., Ballard, R.D., Green, K., Williams, D., Bainbridge, A., Crane, K., & van Andel, T.H., 1979. Submarine thermal springs on the Glalapagos Rift, *Science*, *203*, 1073-1083.

Cox, C.S., Constable, S.C., Chave, A.D. & Webb, S.C., 1986. Controlled-source electromagnetic sounding of the oceanic lithosphere, *Nature*, *320*, 52-54.

Davis, B. & Martin, B., 1979. Numerical inversion of the Laplace transform: a survey and comparison of methods, *J. Comp. Phys.*, *33*, 1-37.

Edwards, R.N., 1997. On the resource evaluation of marine gas hydrate deposits using sea-floor transient electric dipole-dipole methods, *Geophysics*, *62*, 1, 63-74.

Edwards, R.N., Bailey, R.C. & Garland, G.D., 1981. Conductivity anomalies: lower crust or asthenosphere?, *Physics of the Earth and Planetary Interiors*, *25*, 263-272.

Edwards, R.N. & Chave, A.D., 1986. A transient electric dipole-dipole method for mapping the conductivity of the sea floor, *Geophysics*, *51*, 984-987.

Edwards, R.N. & Cheesman, S.J., 1987. Two-dimensional modeling of a towed transient magnetic dipole-dipole sea floor EM system, *J. Geophysics, 61*, 110-121.

Edwards, R.N., Law, L.K. & DeLaurier, J.M., 1981. On measuring the electrical conductivity of the oceanic crust by a modified magnetometric resistivity method, *J. Geophys. Res., 86*, 11609-11615.

Edwards, R.N., Law, L.K., Wolfgram, P.A., Nobes, D.C., Bone, M.N., Trigg, D.F. & DeLaurier, J.M., 1985. First results of the MOSES experiment: sea sediment conductivity and thickness determination, Bute Inlet, British Columbia, by magnetometric off-shore electrical sounding, *Geophysics, 50*, 153-160.

Edwards, R.N., Wolfgram, P.A. & Judge, A.S., 1988. The ICE-MOSES experiment: Mapping permafrost zones electrically beneath the Beaufort Sea. *Mar. Geophys. Res., 9*, 265-290.

Evans, R.L., 1996. A seafloor gravity profile across the TAG hydrothermal mound, *Geophys. Res. Lett., 23*, 23, 3447-3450.

Evans, R.L. & Everett, M.E., 1994. Discrimination of hydrothermal mound structures using transient electromagnetic methods, *Geophys. Res. Lett., 21*, 6, 501-504.

Evans, R.L., Constable, S.C., Sinha, M.C., Cox, C.S. & Unsworth, M.J., 1991. Upper crustal resistivity structure of the East Pacific Rise near 13°N, *Geophys. Res. Lett., 18*, 10, 1917-1920.

Evans, R.L., Sinha, M.C., Constable, S.C. & Unsworth, M.J., 1994. On the electrical nature of the axial melt zone at 13° N on the East Pacific Rise, *J. Geophys. Res., 99*, B1, 577-588.

Everett, M.E., Edwards, R.N., Cheesman, S.J., Utada, U. & Ferguson, I.J., 1988. Interpretation of seafloor electromagnetic data in applied geophysics, in *Applied Electromagnetics in Materials. Proceedings of the First International Symposium. Tokyo*, 143-153.

Filloux, J.H., 1973. Techniques and instrumentation for study of natural electromagnetic induction at sea, *Phys. Earth Planet. Inter., 7*, 323-338.

Francis, T.J.G., 1985. Resistivity measurements of an ocean floor sulphide mineral deposit from the submersible Cyana, *Mar. Geophys. Res., 7*, 419-438.

Gómez-Trevino, E. & Edwards, R.N., 1983. Electromagnetic soundings in the sedimentary basin of southern Ontario - A case history, *Geophysics, 48*, 3, 311-330.

Hekinian, R., Franchetau, J., Renard, V., Ballard, R.D., Choukroune, P., Cheminee, J.L., Albarede, F., Minster, J.F., Charlou, J.L., Marty, J.C., & Boulegue, J., 1983. Intense hydrothermal activity at the axis of the East Pacific Rise near 13°N: submersible witnesses the growth of sulfide chimney, *Mar. Geophys. Res., 6*, 1-114.

Hekinian, R., 1984. Undersea volcanoes, *Sci. American, 251*, 7, 46-55.

Humphris, S.E., Herzig, P.M., Miller, D.J., Alt, J.C., Becker, K., Brown, D., Brugmann, G., Chiba, H., Fouquet, Y., Gemmell, J.B., Guerin, G., Hannington, M.D., Holm, N.G., Honnorez, J.J., Iturrino, G.J., Knott, R., Ludwig, R., Nakamura, K., Petersen, S., Reysenbach, A.L., Rona, P.A., Smith, S., Sturz, A.A., Tivey, M.K. & Zhao, X., 1995. The internal structure of an active sea-floor massive sulphide deposit, *Nature, 377*, 713-716.

Humphris, S.E. & Kleinrock, M.C., 1996. Detailed morphology of the TAG active hydrothermal mound: Insights into its formation and growth, *Geophys. Res. Lett., 23*, 23, 3443-3446.

Karson, J.A. & Rona, P.A., 1990. Block-tilting, transfer faults, and structural control of magmatic and hydrothermal processes in the TAG area, Mid-Atlantic Ridge 26° N, *Geological Society of America Bulletin, 102*, 1635-1645.

Kaufman, A.A. & Keller, G.V., 1983. *Frequency and Transient Soundings*, Elsevier, New York.

Kleinrock, M.C. & Humphris, S.E., 1996. Structural asymmetry of the TAG rift valley: Evidence from a near-bottom survey for episodic spreading, *Geophys. Res. Lett., 23*, 23, 3439-3442.

Knight, J.H. & Raiche, A.P., 1982. Transient electromagnetic calculations using the Gaver-Stehfest algorithm, *Geophysics, 47*, 47-50.

Lalou, C., Thompson, G., Arnold, M., Brichet, E., Druffel, E. & Rona, P.A., 1990. Geochronology of TAG and Snake Pit hydrothermal fields, Mid-Atlantic Ridge: Witness to a long and complex hydrothermal history, *Earth and Plan. Science Letters, 97*, 113-128.

Lalou, C., Reyss, J.L., Brichet, E., Arnold, M., Thompson, G., Fouquet, Y. & Rona, P.A.,

1993. New age data for Mid-Atlantic Ridge hydrothermal sites: TAG and Snake Pit chronology revisited, *J. Geophys. Res.*, *98*, 9705-9713.

Lister, C.R.B., 1972. On the thermal balance of a mid-ocean ridge, *Geophys. J. R. astr. Soc.*, *26*, 515-535.

Lydon, J.W., 1984. Volcanogenic massive sulphide deposits. Part 1: a descriptive model, in *Ore Deposit Models*, Geoscience Canada Reprint Series 3, Eds. Roberts, R.G. & Sheahan, P.A., 145-153.

Lydon, J.W., 1988. Volcanogenic massive sulphide deposits. Part 2: genetic models, in *Ore Deposit Models*, Geoscience Canada Reprint Series 3, Eds. Roberts, R.G. & Sheahan, P.A., 155-181.

Macdonald, K.C., 1982. Mid-ocean ridges: fine scale tectonic, volcanic and hydrothermal processes within the plate boundary zone, *Ann. Rev. Earth Planet. Sci.*, *10*, 155-190.

McGregor, B.A., Harrison, C.G.A., Lavelle, J.W. & Rona, P.A., 1977. Magnetic anomaly patterns on Mid-Atlantic Ridge crest at 26° N, *J. Geophys. Res.*, *82*, 231-238.

Menke, W., 1984, *Geophysical Data Analysis: Discrete Inverse Theory*, Academic Press, New York.

Miller, A.R., Densmore, C.D., Degens, E.T., Hathaway, J.C., Manheim, F.T., McFarlin, P.F., Nelder, J.A. & Mead, R., 1965. A simplex method for function minimisation, *Computer Journal*, *7*, 308-313.

Nobes, D.C., 1984. The magnetometric off-shore electrical sounding (MOSES) method and its application in a survey of upper Jervis Inlet, British Columbia, Ph.D. thesis, University of Toronto.

Nobes, D.C., Law, L.K. & Edwards, R.N., 1986. The determination of resistivity and porosity of the sediment and fractured basalt layers near the Juan de Fuca Ridge, *Geophys. J. Roy. astr. Soc.*, *86*, 289-318.

Nobes, D.C., Law, L.K. & Edwards, R.N., 1992. Results of a sea-floor electromagnetic survey over a sedimented hydrothermal area on the Juan de Fuca Ridge, *Geophys. J. Int.*, *110*, 333-346.

Parasnis, D.S., 1956. The electrical resistivity of some sulphide and oxide minerals and their ores, *Geophysical Prosp.*, *4*, 249-279.

Parkhomenko, E.I., 1967. *Electrical Properties of Rocks*, Plenum Press (New York).

Petiau, G. & Dupis, A., 1980. Noise, temperature coefficient, and long time stability of electrodes for telluric observations, *Geophys. Prosp., 28*, 792-804.

Pocklington, H. & Jokela, A. , 1966. Hot brines and recent iron deposits in deeps of the Red Sea, *Geochimica et Cosmochimica Acta, 30*, 341-359.

Press, W.H., Teukolsky, S.A., Vetterling, W.T. & Flannery, B.P., 1992. *Numerical Recipes in Fortran.* Second Edition, Cambridge University Press.

Riordan, J. & Sunde, E.D., 1933. Mutual impedance of grounded wires for stratified two-layer earth, *Bell Syst. Jour., 12*, 162-177.

Rona, P.A., 1973. New evidence for seabed resources from global tectonics, *Ocean Management, 1*, 145-159.

Rona, P.A., 1986. Mineral deposits from sea-floor hot springs, *Sci. American, 254* 1. 84-92.

Rona, P.A., 1988. Hydrothermal mineralization at oceanic ridges, *Canadian Mineralogist. 26*, 431-465.

Rona, P.A., Hannington, M.D., Raman, C.V., Thompson, G., Tivey, M.K., Humphris, S.E., Lalou, S. & Petersen, S., 1993. Active and relict sea-floor hydrothermal mineralization at the TAG hydrothermal field, Mid-Atlantic Ridge, *Economic Geology. 88*, 8, 1989-2017.

Rona, P.A., Klinkhammer, G., Nelsen, T.A., Tretry, J.H. & Elderfield, H., 1986. Black smokers, massive sulfides, and vent biota at the Mid-Atlantic Ridge, *Nature, 321*, 33-37.

Rona, P.A., McGregor, B.A., Betzer, B.A., Bolger, G.W. & Krause, D.C., 1975. Anomalous water temperatures over Mid-Atlantic Ridge crest at 26° N, *Deep-Sea Research, 22*, 611-618.

Sommerfield, A., 1926. Uber die ausbreitung der wellen in der dratlosen telegraphie, *Annalen der Physik, 4*, 81, 1135-1153.

Sempere, J.C., Purdy, G.M. & Schouten, H., 1990. Segmentation of the Mid-Atlantic Ridge between 24° N and 30°40′ N, *Nature, 344*, 427-431.

Spiess, F.N., MacDonald, K.C., Atwater, T., Ballard, R., Carranza, A., Cordoba, D.,

Cox, C., Diaz Garcia, V.M., Francheteau, J., Guerrero, J., Hawkins, J., Haymon, R., Hessler, R., Juteau, T., Kastner, M., Larson, R., Luyendyk, B., MacDougall, J.D., Miller, S., Normark, W., Orcutt, J. & Rangin, C., 1980. East Pacific Rise: hot springs and geophysical experiments, *Science, 207*, 1421-1433.

Stehfest, H., 1970. Algorithm 368, numerical inversion of Laplace transforms, *Commun. ACM, 13*, 47-49.

Telford, W.M., Geldart, L.P., Sheriff, R.E. & Keys, D.A., 1986. *Applied Geophysics*, Cambridge University Press.

Tivey, M.A., Rona, P.A. & Schouten, H., 1993. Reduced crustal magnetization beneath the active sulfide mound, TAG hydrothermal field, Mid-Atlantic Ridge at 26° N, *Earth and Plan. Science Lett., 115*, 101-115.

Tivey, M.K., Humphris, S.E. & Thompson, G., 1995. Deducing patterns of fluid flow and mixing within the TAG active hydrothermal mound using mineralogical and geochemical data, *J. Geophys. Res., 100*, B7, 12,527-12,555.

Unsworth, M., 1994. Exploration of mid-ocean ridges with a frequency-domain electromagnetic system, *Geophys. J. Int., 116*, 447-467.

Villinger, H., 1984. Solving cylindrical geothermal problems using the Gaver-Stehfest inverse Laplace transform, *Geophysics, 50*, 1581-1587.

Von Herzen, R.P., Kirklin, J. & Becker, K., 1996. Geoelectrical measurements at the TAG hydrothermal mound, *Geophys. Res. Lett., 23*, 23, 3451-3454.

Vozoff, K. & Jupp, D.L.B., 1975. Joint inversion of geophysical data, *Geophys. J. Roy. astr. Soc., 42*, 977-991.

Webb, S.C., Constable, S.C., Cox, C.S. & Deaton, T.K., 1985. A seafloor electric field instrument, *J. Geomag. Geoelectr., 37*, 1115-1129.

Webb, S.C. & Edwards, R.N., 1995. On the correlation of electrical conductivity and heat flow in Middle Valley, Juan de Fuca Ridge, *J. Geophys. Res., 100*, B11, 22523-22532.

Webb, S.C., Edwards, R.N. & Yu, L., 1993. First measurements from a deep-tow electromagnetic sounding system, *Mar. Geophys. Res., 15*, 13-26.

Wolfgram, P.A., 1985. Development and application of a short-baseline electromagnetic exploration technique for the ocean floor, Ph.D. thesis, University of Toronto.

Wolfgram, P.A., Edwards, R.N., Law, L.K. & Bone, M.N., 1986. Polymetallic sulfide exploration on the deep sea floor: The feasibility of the MINI-MOSES technique, *Geophysics, 51*, 1808-1818.

Yang, J, Edwards, R.N., Molson, J.W. & Sudicky, E.A., 1996. Three-dimensional numerical simulation of the hydrothermal system within TAG-like sulfide mounds, *Geophys. Res. Lett., 23*, 23, 3475-3478.

Young, P.D. & Cox, C.S., 1981. Electromagnetic active source sounding near the East Pacific Rise, *Geophys. Res. Lett., 8*, 1043-1046.

Yu, L., 1994. Computation of the Electrical Responses of Mid-ocean Ridge Structures, PhD Thesis, University of Toronto.

Yu, L. & Edwards, R.N., 1992a. The detection of lateral anisotropy of the ocean floor by electromagnetic methods, *Geophys. J. Int., 108*, 433-441.

Yu, L. & Edwards, R.N., 1992b. Algorithms for the computation of the electromagnetic response of a multilayered, laterally anisotropic sea floor to arbitrary finite sources, *Geophys. J. Int., 111*, 185-189.

Yu, L. & Edwards, R.N., 1996. Imaging axi-symmetric TAG-like structures by transient electric dipole seafloor electromagnetics, *Geophys. Res. Lett., 23*, 23, 3459-3462.

Appendix A

First Generation Amplifiers

Figure A.1 is a block diagram of the FET chopper amplifiers that were used in the TAG survey. Their design was subject to the same considerations as those described in Section 4.3 for the second generation amplifier.

On input to the amplifier, the signal was chopped at 30 kHz by four low-noise, low-resistance FETs. This modulated the signal with carrier frequencies at the chopper's fundamental and odd harmonics, frequency shifting it to upper and lower sidebands about each carrier frequency. The chopping frequency therefore had to be sufficiently high that the upper and lower sidebands from adjacent carrier frequencies did not overlap. Chopping may be thought of as a form of sampling and is subject to the same issues of aliasing, which from this perspective consists of overlapping sidebands. If the possibility of even harmonics in the chopping signal is introduced, the condition on chopping frequency becomes exactly the Nyquist condition: the chopping frequency must be $\geq$ twice the measurable bandwidth of the signal in order to avoid aliasing.

The chopped signal fed into a Hammond 109L wideband audio transformer which served several purposes. It electrically isolated the electronics from the electrodes and seawater ground. It also had a low input impedance on the front end permitting low voltage noise pickup, and stepped up the signal voltage by a factor of 66. Finally, it acted as a bandpass filter, having a bandwidth of 30 Hz to 30 kHz. The chopping frequency was selected to coincide with the transformer's high frequency cutoff so that all but the lower sideband of the chopper's fundamental were attenuated.

The transformer's output fed into a FET differential amplifier. The total gain at the end of this stage was 5000. The signal next ran through filters designed to clean the lower

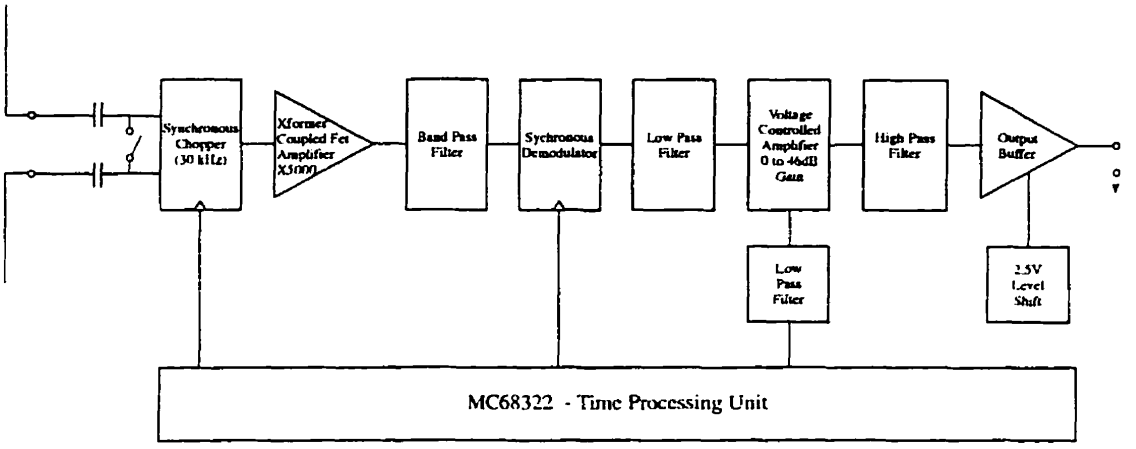

Figure A.1: Block diagram of FET chopper amplifiers used in TAG experiment.

sideband signal by stripping it of noise outside its bandwidth, and was then demodulated by remixing it with the chopper. While the lower sideband of the demodulating chopper's fundamental frequency was then back to the original frequency band of the signal, demodulating introduced high frequency artifacts. These were removed with an 8th order Bessel low-pass filter - the order being determined from the requirement of dropping amplitude by 72 dB (the dynamic range of the data logger's ADC) in the 20 kHz between the carrier's fundamental at 30 kHz and the upper frequency of the signal, up to 10 kHz.

The signal was then amplified through a voltage-controlled amplifier, and high-pass filtered to removed low frequency noise introduced in that stage. The amplified signal was then run through an optoisolator and level shifted for input to the data logger.

The chopping and demodulating signals were 30 kHz square waves generated by timer channels on the data logger's time-processing unit. Gain of the voltage controlled amplifier was controlled using another timer channel generating a variable duty cycle square wave at 50 kHz. This signal fed through a low-pass filter, providing an averaged voltage which determined the gain of the backstage amplifier.

With unity gain on the voltage-controlled amplifier, the system gain was fixed by the input stage as 74 dB. The maximum gain was tuned to 120 dB. Gain of the voltage-controlled amplifier varied linearly with the duty cycle of the control signal from the data logger's timer channel. The total gain of the amplifier as a function of the duty cycle of the control signal was accordingly 74 dB + 0.46×(100 - percent high time) dB.

Appendix B

Examples of Data Collected with the Second Generation Amplifiers

The data shown in Figures B.1 and B.2 were collected using the instrumental amplifiers described in Chapter 4. The range of the measurements is unknown as navigation systems failed during the experiments when these data were collected. The data in Figure B.1 were collected at a depth of 1.8 km at the base of Magic Mountain hydrothermal mound on the East Pacific Rise in an experiment using the ROPOS ROV. The data in Figure B.2 were collected in 30 m deep coastal waters during the first experiment in which we had to deal with significant levels of noise from power lines.

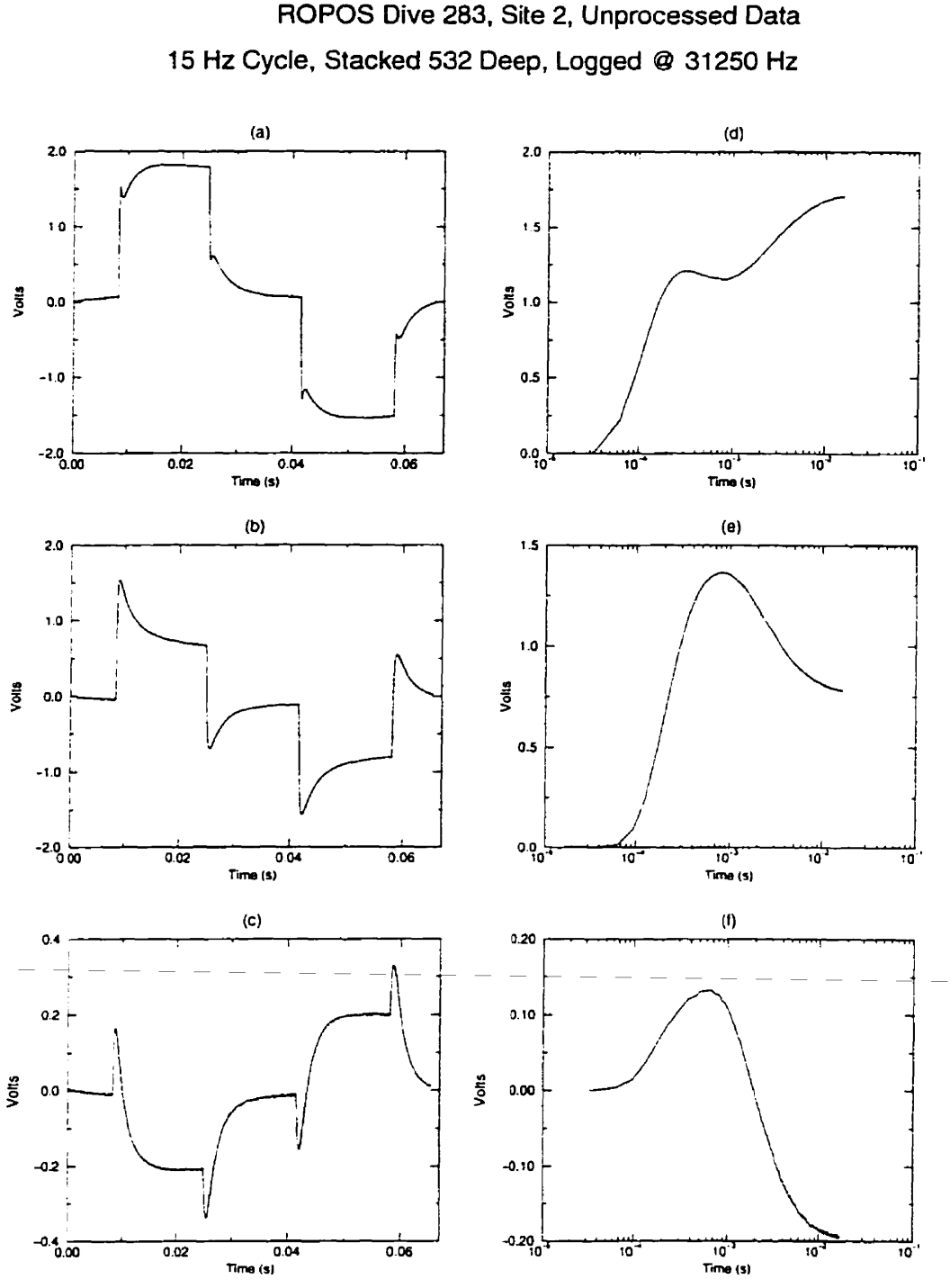

Figure B.1: Samples of unprocessed data collected at the base of the Magic Mountain hydrothermal site on the East Pacific Rise using ROPOS. While the data were very clean, they were uninterpretable due to lack of navigational information. Plates (a) to (c) show measurements of the complete transmitter period. Plates (d) to (f) show the 2nd transitions for these measurements extracted and plotted logarithmically.

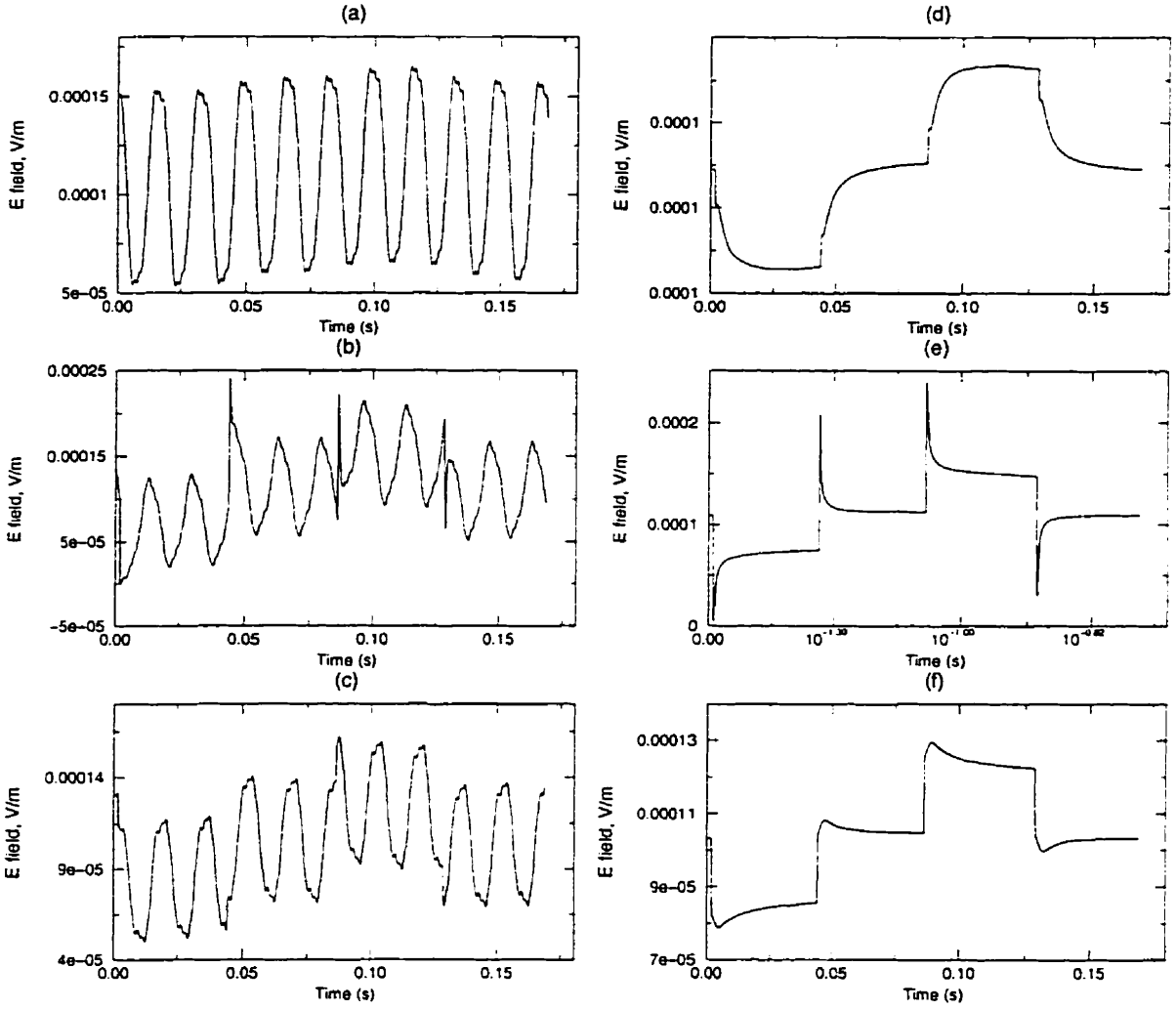

Figure B.2: Samples of unprocessed data collected in 30 m deep waters of Saanich Inlet. Plates (a) to (c) show unstacked data, which is dominated by 60 Hz noise. Plates (d) to (f) show the corresponding 2003 deep stacked data. The data could not be interpreted due to the failure of differential GPS positioning.

Appendix C

Results of Data Reduction

Site	Time	Slant Range (m)	Rel. Depth (m)	Polar Angle (deg)	Transmitter Orientation (deg)	Approx. Bandwidth (Hz)	Comments
1	11:00	49	-3	355	94	1000	Driving over northern scarp wall. Depth change 6.4 m during measurement, speed 0.12 m/s. Strong signal.
2	11:05	67	6	355	234	750	Stationary facing northern scarp wall. Strong signal.
3	11:10	52	2	348	235	1000	Deploying ODP marker C. Sub stationary. Strong signal.
-	11:15	-	-	-	-	-	At northern scarp wall. Strong signal. Discarded due to 19° bearing change.
4	11:20	82	23	344	241	300	Stationary facing base of northern scarp wall. Strong signal.
-	11:25	-	-	-	-	-	Beginning EM circle. Discarded due to 15° bearing change.

Table C.1: Summary of Pre-Processing Results, 11:00 to 11:25.

Site	Time	Slant Range (m)	Rel. Depth (m)	Polar Angle (deg)	Transmitter Orientation (deg)	Approx. Bandwidth (Hz)	Comments
5	11:30	75	21	268	297	250	Weak signal. Speed 0.21 m/s. Sulfide rubble.
6	11:35	71	16	243	223	750	Near sulfide/carbonate slope. Speed 0.18 m/s. Solid signal.
-	11:40	-	-	-	-	-	Solid signal discarded due to 22° bearing change.
-	11:45	-	-	-	-	-	Over carbonate slump slope. Weak signal. Discarded due to 32° bearing change.
-	11:50	-	-	-	-	-	Strong signal discarded due to 17° bearing change.
7	11:55	69	10	104	94	600	Kremlin area. Sulf. with extinct chimneys. Solid signal. Stable heading. Speed 0.22 m/s.
8	12:00	56	5	49	61	600	Over depression with rough sulf. near inactive chimneys. Solid signal. Stable heading. Speed 0.21 m/s.
-	12:05	-	-	-	-	-	Off bottom while turning. Discarded due to 59° bearing change.
-	12:10	-	-	-	-	-	Weak signal. Discarded due to 18° bearing change.

Table C.2: Summary of Pre-Processing Results, 11:30 to 12:10.

Site	Time	Slant Range (m)	Rel. Depth (m)	Polar Angle (deg)	Transmitter Orientation (deg)	Approx. Bandwidth (Hz)	Comments
9	12:15	52	1	29	318	2000	Patchy sediment on sulf. Attempted heat flow station. Very clean signal. Stationary.
9	12:20				355		Same except for heading change.
9	12:25						Same as 12:20.
-	12:30						Offscale.
-	12:35						Offscale.
-	12:40						Offscale.
10	12:45	50	6	120	267	1000	In Kremlin area. Chimneys and shimmering water. Bearing stable. Depth change 6 m during measurement. Solid signal. Poor transp. fixes.
-	12:50	-	-	-	-	-	Attempting HF station. Strong signal. Discarded due to 16° bearing change.
11	12:55	66	14	133	281	750	Stationary at HF site in carbonates. Clean, solid signal.
11	13:00						Same.
11	13:05						Same.
-	13:10	-	-	-	-	-	Discarded due to polarity reversal.
11	13:15						Same as 12:55.

Table C.3: Summary of Pre-Processing Results, 12:15 to 13:15.

Site	Time	Slant Range (m)	Rel. Depth (m)	Polar Angle (deg)	Transmitter Orientation (deg)	Approx. Bandwidth (Hz)	Comments
-	13:20	-	-	-	-	-	Leaving HF site. Discarded due to 15° bearing change.
-	13:25	-	-	-	-	-	Moving into position for HF site. Discarded due to 17° bearing change.
12	13:30	90	12	135	44	400	Stationary at HF station. Facing base of sed. slope. Signal weak.
12	13:35						Same.
12	13:40						Same.
12	13:45						Same.
12	13:50						Same.
-	13:55	-	-	-	-	-	Leaving HF station. Discarded due to 70° bearing change.
-	14:00	-	-	-	-	-	Very weak signal. Discarded due to polarity flip.
13	14:05	123	19	146	344	200	Stationary at heat flow site off mound amid carbonates with sed. covered pillows. Weak signal.
13	14:10						Same.
13	14:15						Same.
13	14:20						Same.
-	14:25	-	-	-	-	-	Very weak signal. Discarded due to break in nav. record.

Table C.4: Summary of Pre-Processing Results, 13:20 to 14:25.

Appendix D

Homogeneous Seafloor Modeling Results

In this appendix the processed transient from each station is plotted along with the transient response of the theoretical double half-space model which provided the best fit in a least-squares sense. (For details on processing of the data and modeling procedure, see Chapters 5 and 6 respectively). Solid lines are the recorded data, while dotted lines are the model response. The 20 logarithmically spaced points in time at which the data were fitted are denoted by diamonds on the model response. Seafloor conductivity for the best fit model is included in each figure, along with absolute error in seafloor conductivity as determined from eigenparameter analysis, and root-mean-square error of fit of the model response to the unfiltered data.

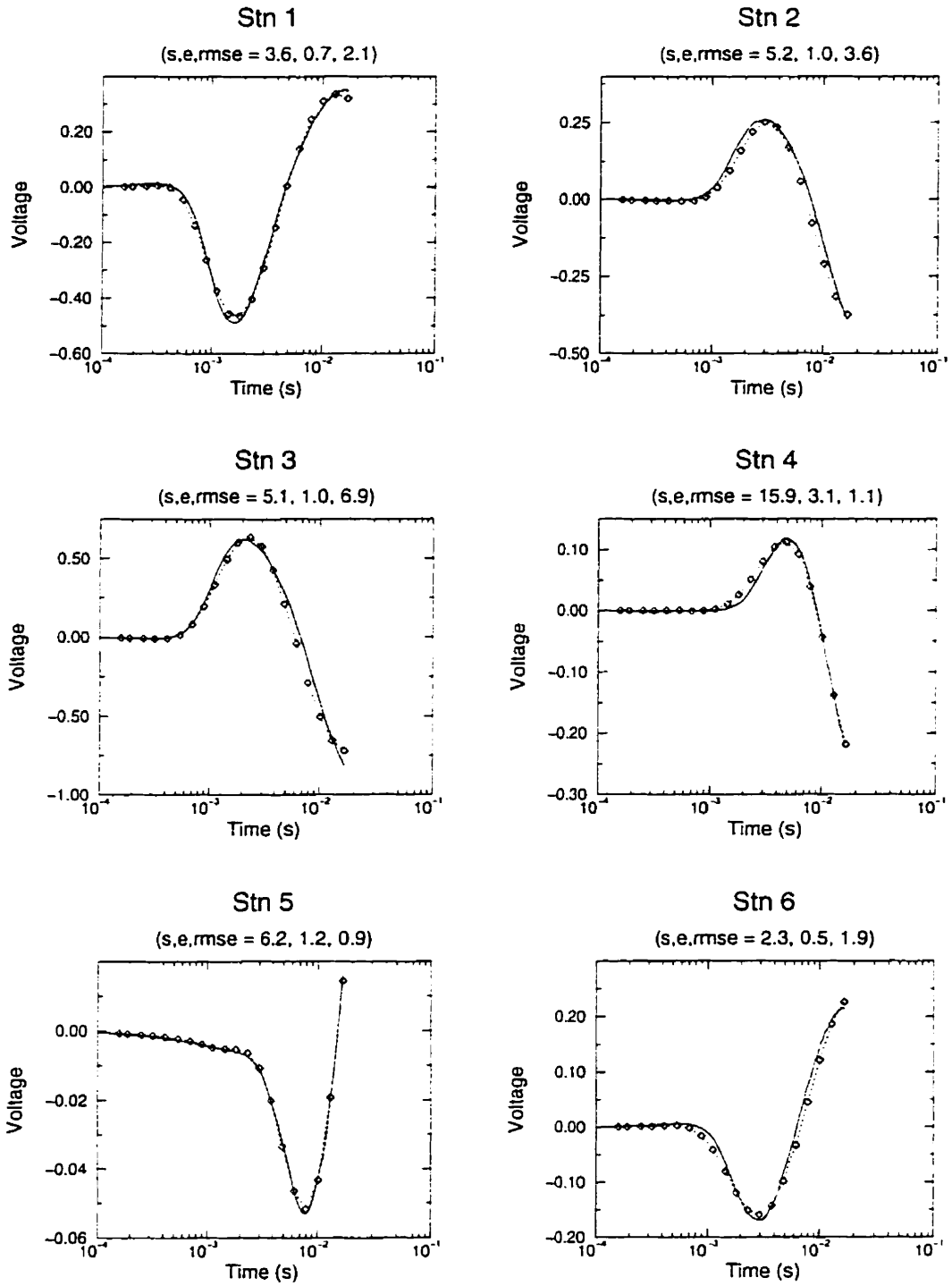

Figure D.1: The data recorded for sites 1 to 6 (solid lines) after filtering are plotted with the best-fit double half-space models (diamonds and dotted lines). The variables s, e and rmse stand for seafloor conductivity, absolute error in seafloor conductivity from eigenparameter analysis, and root-mean-square error of fit to the unfiltered data.

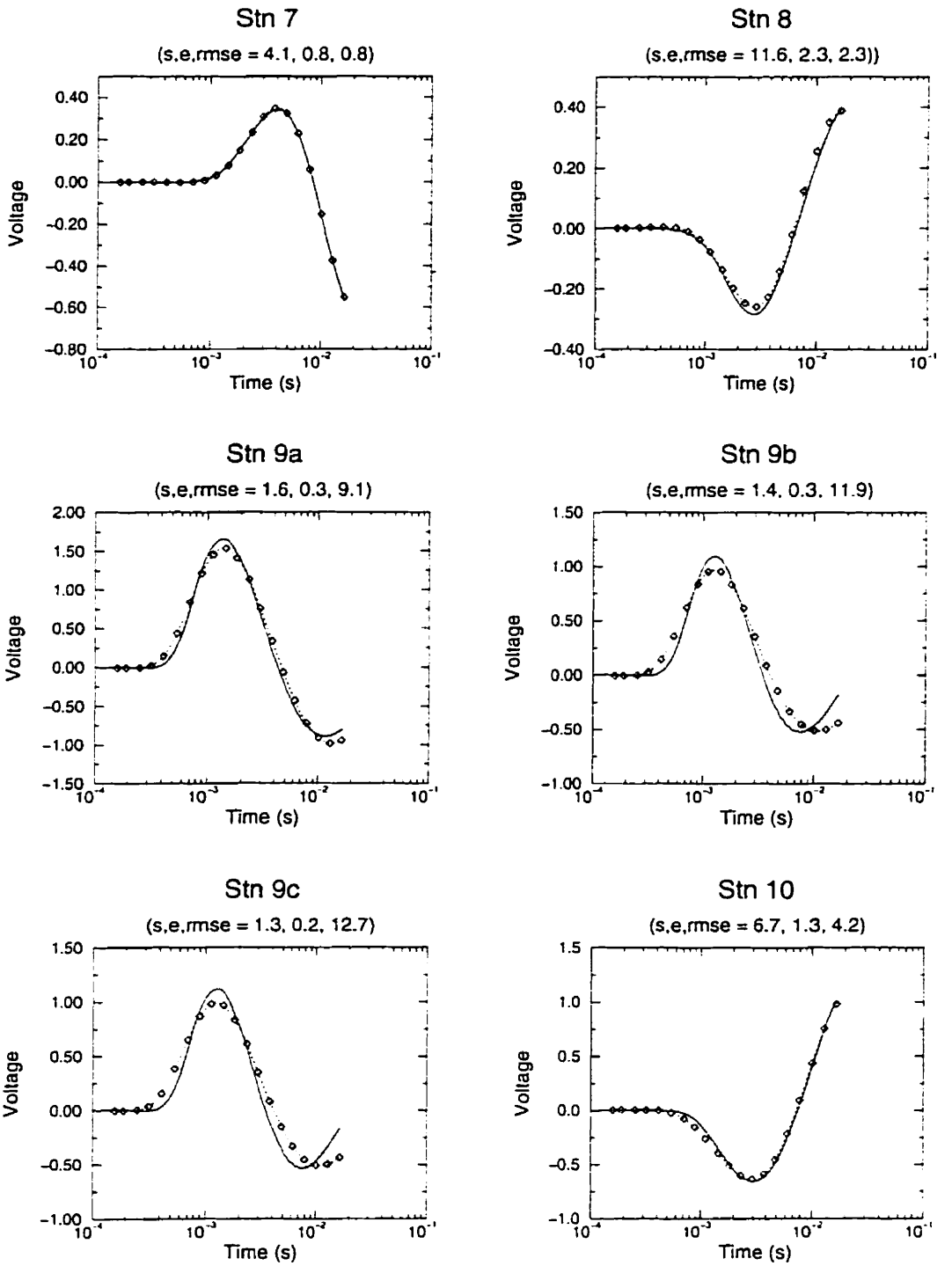

Figure D.2: The data recorded for sites 7 to 10 (solid lines) after filtering are plotted with the best-fit double half-space models (diamonds and dotted lines). The variables s, e and rmse stand for seafloor conductivity, absolute error in seafloor conductivity from eigenparameter analysis, and root-mean-square error of fit to the unfiltered data.

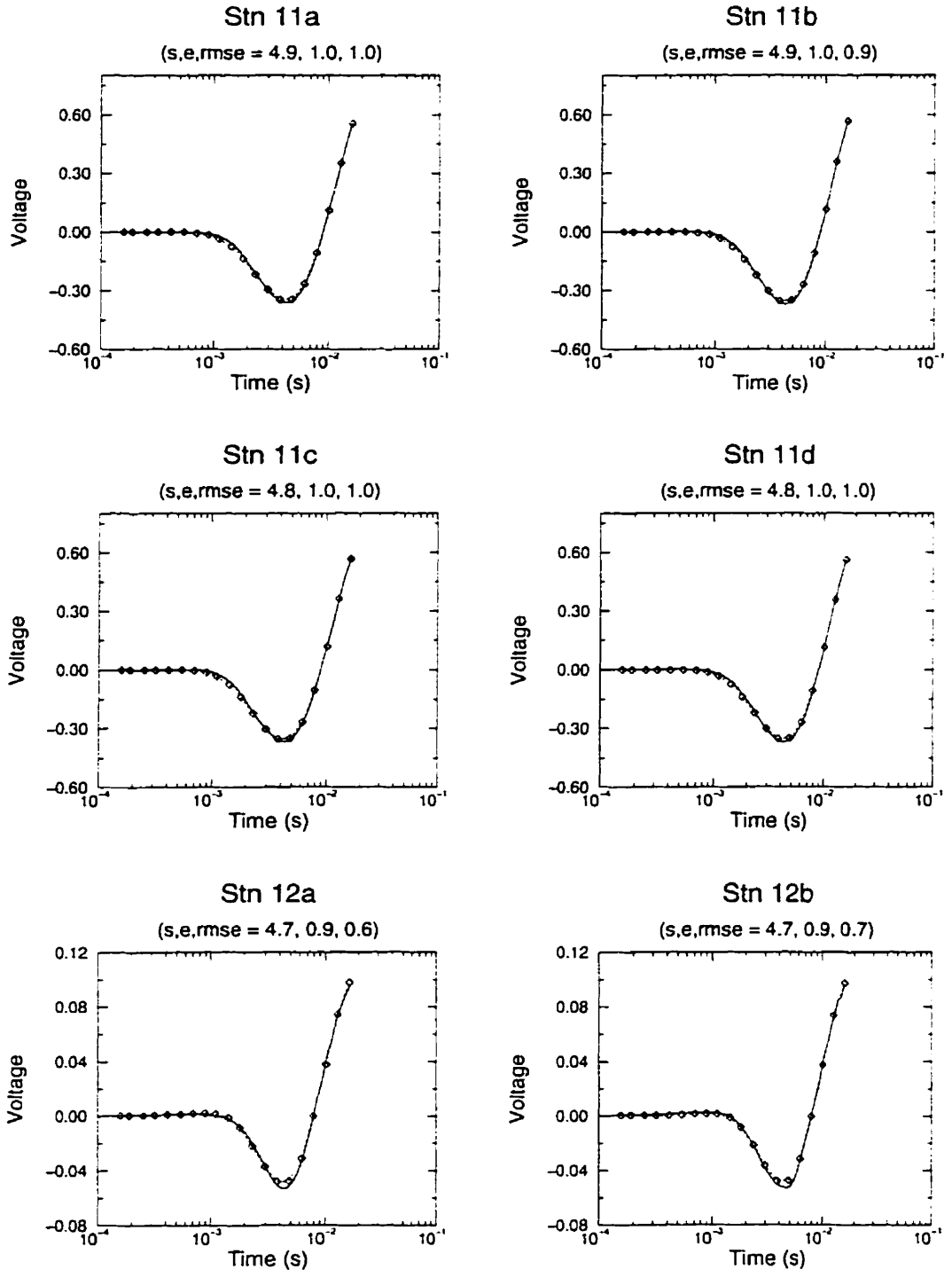

Figure D.3: The data recorded for sites 11 and 12 (solid lines) after filtering are plotted with the best-fit double half-space models (diamonds and dotted lines). The variables s, e and rmse stand for seafloor conductivity, absolute error in seafloor conductivity from eigenparameter analysis, and root-mean-square error of fit to the unfiltered data.

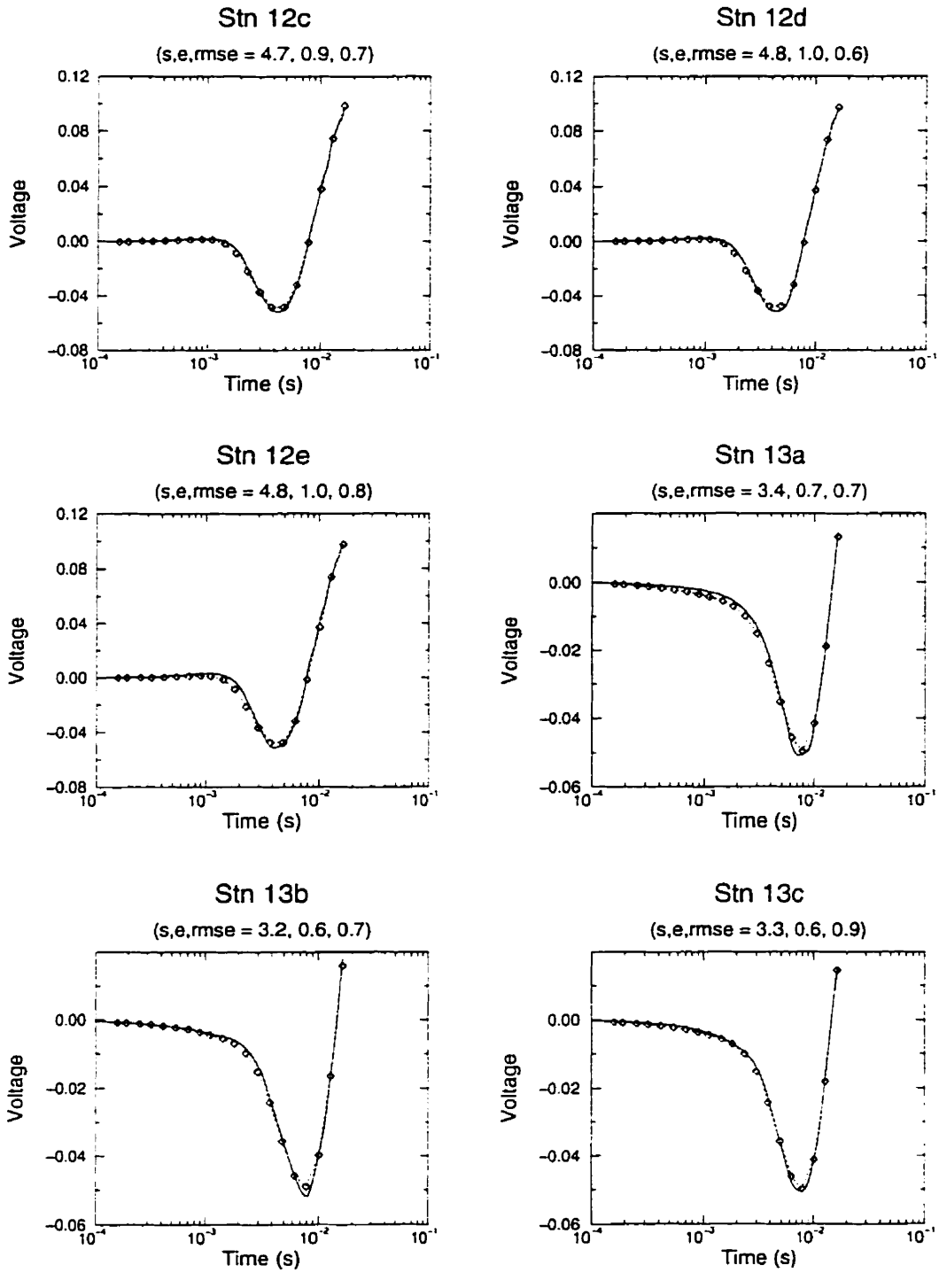

Figure D.4: The data recorded for sites 12 and 13 (solid lines) after filtering are plotted with the best-fit double half-space models (diamonds and dotted lines). The variables s, e and rmse stand for seafloor conductivity, absolute error in seafloor conductivity from eigenparameter analysis, and root-mean-square error of fit to the unfiltered data.

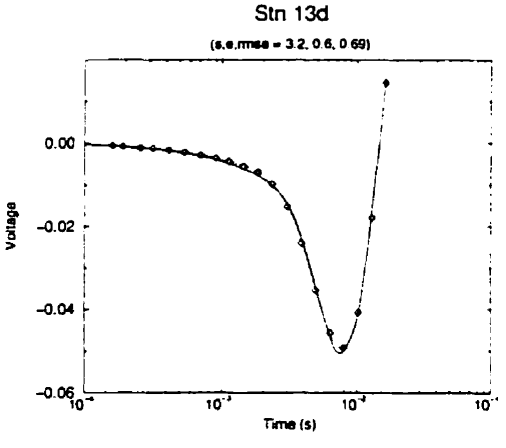

Figure D.5: The data recorded for site 13d (solid lines) after filtering are plotted with the best-fit double half-space models (diamonds and dotted lines). The variables s, e and rmse stand for seafloor conductivity, absolute error in seafloor conductivity from eigenparameter analysis, and root-mean-square error of fit to the unfiltered data.

Appendix E

Layered Seafloor Modeling Results

In this appendix the processed transient from each station is plotted along with the transient response of the layer over a half-space model which provided the best fit in a least-squares sense. (For details on processing of the data and modeling procedure, see Chapters 5 and 6 respectively). Solid lines are the recorded data, while dotted lines are the model response. The 20 logarithmically spaced points in time at which the data were fitted are denoted by diamonds on the model response.

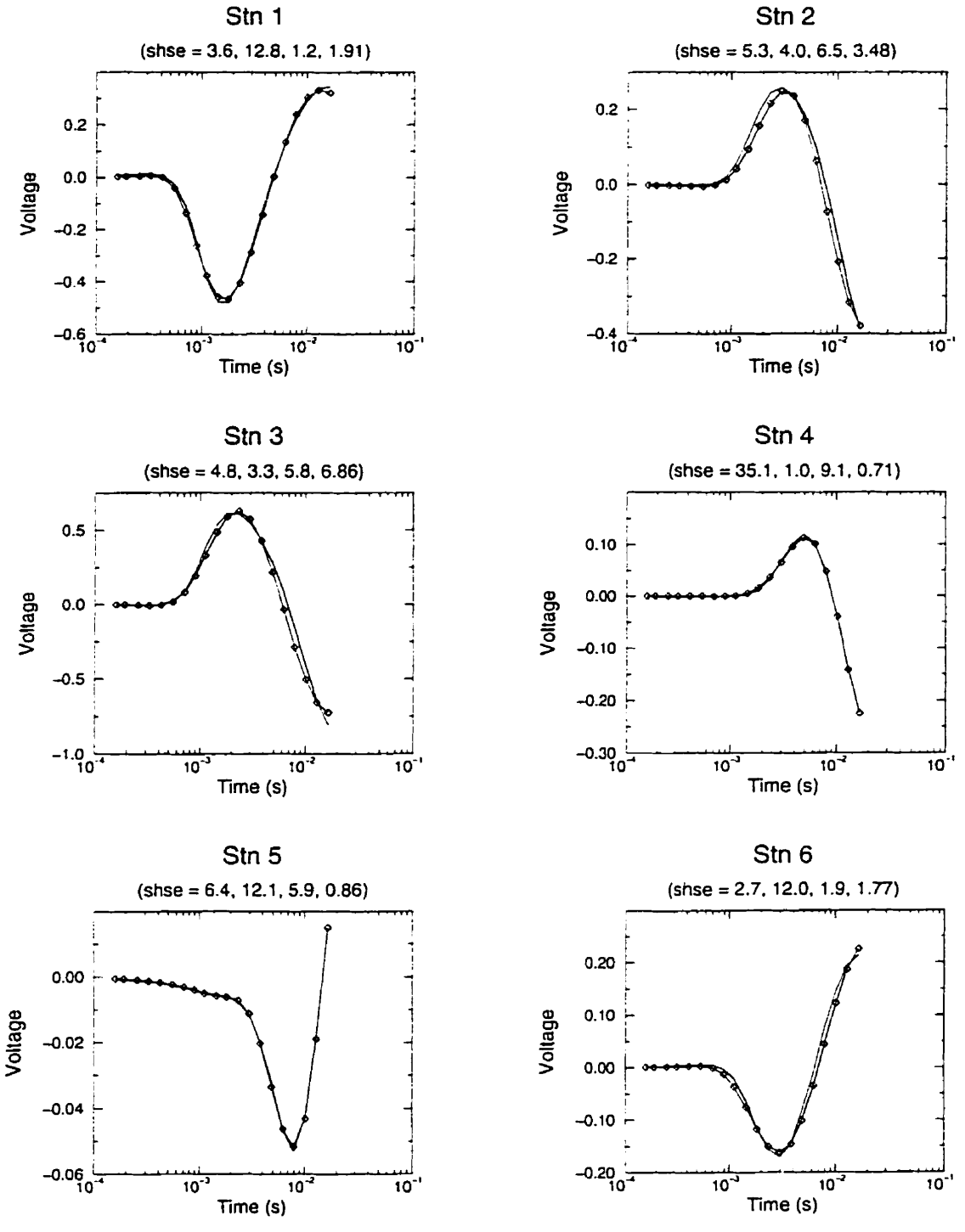

Figure E.1: The data recorded for sites 1 to 6 (solid lines) after filtering are plotted with the best-fit layer over a half-space models (diamonds and dotted lines). The variables s, h, s and e in the figure heading stand for conductivity of the upper layer, thickness of the layer, conductivity of the basement, and root-mean-square error of fit to the unfiltered data.

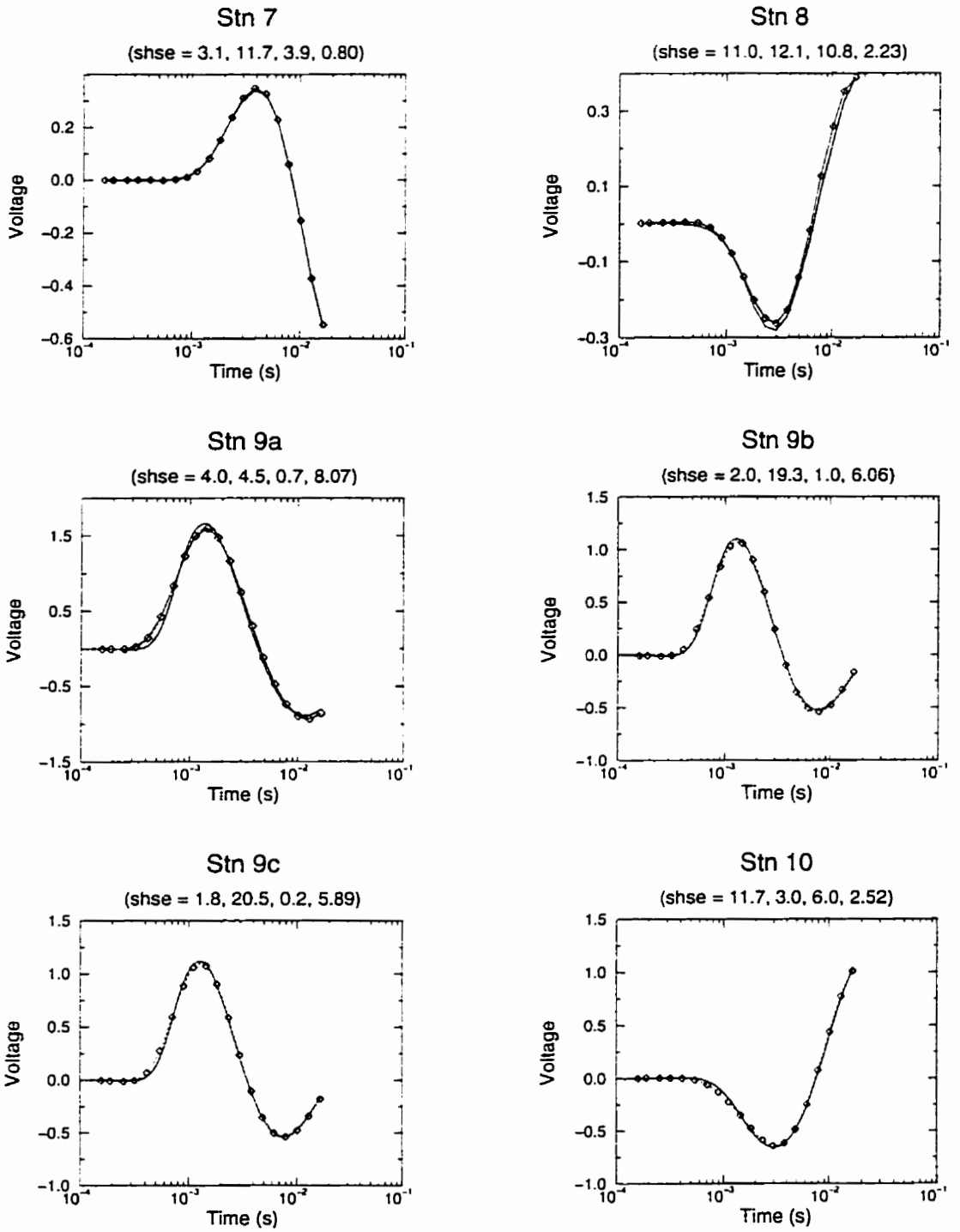

Figure E.2: The data recorded for sites 7 to 10 (solid lines) after filtering are plotted with the best-fit layer over a half-space models (diamonds and dotted lines). The variables s, h, s and e in the figure heading stand for conductivity of the upper layer, thickness of the layer, conductivity of the basement, and root-mean-square error of fit to the unfiltered data.

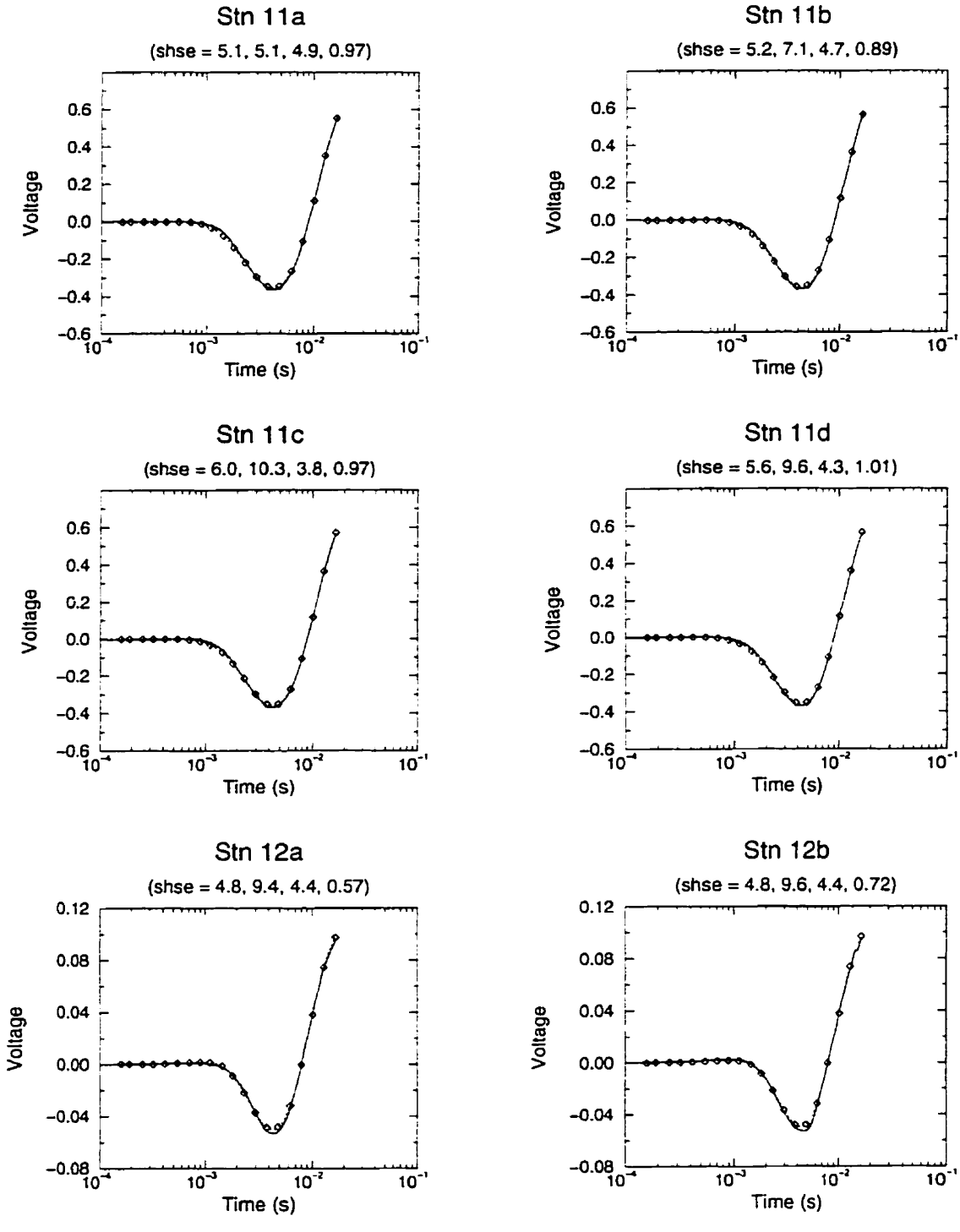

Figure E.3: The data recorded for sites 11 to 12 (solid lines) after filtering are plotted with the best-fit layer over a half-space models (diamonds and dotted lines). The variables s, h, s and e in the figure heading stand for conductivity of the upper layer, thickness of the layer, conductivity of the basement, and root-mean-square error of fit to the unfiltered data.

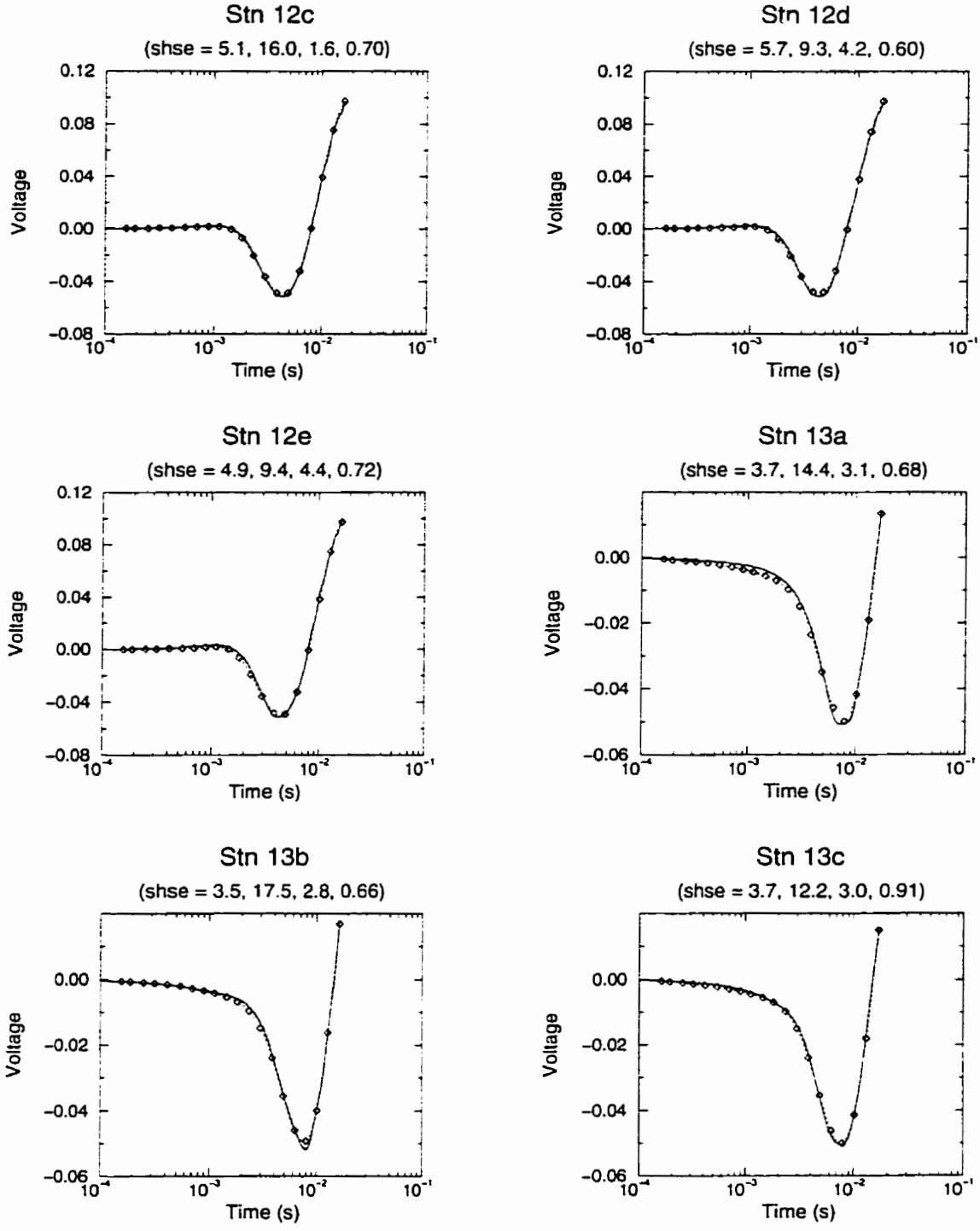

Figure E.4: The data recorded for sites 11 to 12 (solid lines) after filtering are plotted with the best-fit layer over a half-space models (diamonds and dotted lines). The variables s, h, s and e in the figure heading stand for conductivity of the upper layer, thickness of the layer, conductivity of the basement, and root-mean-square error of fit to the unfiltered data.

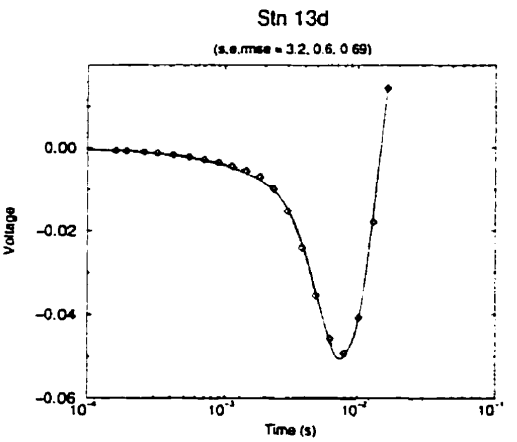

Figure E.5: The data recorded for sites 13d (solid lines) after filtering are plotted with the best-fit layer over a half-space models (diamonds and dotted lines). The variables s, h, s and e in the figure heading stand for conductivity of the upper layer, thickness of the layer, conductivity of the basement, and root-mean-square error of fit to the unfiltered data.

Appendix F

The TEM Software

In the following pages the current version of the control program for the TEM instruments is listed. This version is simpler than that used at TAG as the present amplifiers operate independently from the data logger. The program is written in Think C and makes extensive use of Tattletale library functions.

```
/*************************************************************************
** myheader.h  --  General variable and prototype definitions  **
** for TDEM logging program.                                    **
** March 20, 1993                                              **
*************************************************************************/
#pragma once

// TT7 include libraries

#include <TT7.h>
#include <atod.h>
#include <rtc.h>
#include <uee.h>
#include <tpu.h>
#include <pins.h>
#include <sim.h>
#include <psram.h>
#include <serio.h>
#include <pario.h>
#include <timing.h>
#include <drive.h>
#include <datafile.h>
#include <offload.h>
#include <userio.h>

#include <stdio.h>
#include <stdlib.h>
#include <time.h>
#include <math.h>

// Structure in which logging parameters are stored

struct General_Parms
{
char direction;
ulong TxPeriod;
ushort ADCPeriod;
ushort Stack_depth;
time_t start;
ushort cycles;
ushort cyc_offs;
ushort cycles_to_disc;
ushort SyncPeriod;
ulong T2CLK;
char Inst_name[10];
char survey[10];
};

struct cycle_struct
{
time_t start;
char component;
};

ulong Transmit(ushort i, char *datastart);
ulong Receive(ushort i, char *datastart);

// User I/O menus

void Interact(void);
ushort ShowSystemParms(void);
ushort ShowGeneralParms(void);
ushort ShowSchedule(void);
ushort TestMenu(void);
void TestTransmitter(ulong TxPeriod, ushort ADCPeriod, ushort Stack);
void TestReceive(ulong TxPeriod, ushort ADCPeriod, ushort  Stack);
bool QueryUShort(ptr prompt, ptr defFmt, ptr scanFmt, ushort *value);
```

```
void ViewStackedData(char *memptr, ulong Samples, ushort Stack);
void ViewRawData(char *memptr, ulong Samples);


// 8 bit DIO pin bus control functions

void ConfIOPins(void);
void Latch(ushort Chip);
void SetPins(ushort byte);
void TxPower(ushort byte);

// utility functions

bool Schedule(void);
bool CheckParms(void);
char *WriteHeader(ushort i, char *txtptr,ushort Stack, bool LIVE);
char *WriteTailor(ulong counts, char *txtptr,ushort Stack);
void SetupADC(ulong ADCPeriod);
void SetupTransmit(char comp, ulong TxPeriod);
void SetupReceive(char comp, ulong TxPeriod);
void TriggerRxX(void);
void TriggerRxY(void);
void TriggerTx_X(void);
void TriggerTx_Y(void);
float ZeroPSRAM(char *StartAddr, long numbytes);
ulong LogRTPolled(char *memptr,ushort Stack,ulong Samples,ushort ADCChan,ushort TxChan);
void DisableTPUChans(void);
ulong WriteToDisk(short StartDFNum, ushort numfiles);
float MeasureSyncPeriod(void);
void UeeErrCheck(UeeErr  err);
void MonCmd(char *cmdstrm);

// define ADC channel allocations

#define ADC_RX_X 0
#define ADC_RX_Y 1
#define ADC_TX_X 2
#define ADC_TX_Y 3

// define TPU channel allocations

#define TPU_TX_REF 6
#define TPU_TXPOL_X 7
#define TPU_TXON_X 8
#define TPU_TXPOL_Y 10
#define TPU_TXON_Y 11
#define TPU_AMP_TEST         12
#define TPU_ADC_TH 14

// define data register labels for assembler sections

#define dDATA d0
#define dCISR d1
#define dSAMP d2
#define dSTACK d3
#define dCHECK d4
#define dLSB d5
#define dMASK d6

// define address register labels for assembler sections

#define aADMS a0
#define aADLS a1
#define aPTR a2
#define aCISR a3
#define aADCMD a4
```

```
#define DISK_WRITE_SECS  60
#define HOURS_TO_START  2

// Define pins on 8 bit I/O bus with Chip Select 2

#define TX_CH1_ENB 0x02 // AS (E,5)
#define TX_CH2_ENB 0x01 // DSACK1 (E,1)
#define TX_OFF 0x00

#define OurTickRate  1000
#define hdrblock 1024
#define blocksize  131072
```

```
/*************************************************************************
**  main.c -- the main logging kernel for TDEM program.
*************************************************************************/


#include "myheader.h"

struct General_Parms GP;
struct cycle_struct *cycle;

char *PSStart;
long memsize;
short DFNUM = 0;
ulong tcr1;
float tcr2;
bool    LIFE=FALSE;

main()
{
time_t now;
char cmd, *txtptr,*datastart;
ushort i;
ulong counts,t;

UeeErrCheck(UeeReadBlock(0, (uchar *)&GP.direction, sizeof(GP)));

if (_TMCR->PSCK == 1)
tcr1 = (SimGetFSys() >> 2) >> _TMCR->PRSCL1;
else
tcr1 = (SimGetFSys() >> 5) >> _TMCR->PRSCL1;

if (!SetTickRate(OurTickRate))
printf("\n\nERROR SETTING TICK RATE");

PSMemFreeAll();
if ((PSStart = PSMemAllocAll(&memsize)) == NULL)
printf("\nError Allocating PSRAM");
printf("\nMEMSIZE = %ld", memsize);

ConfIOPins();
TxPower(TX_OFF);
DisableParIO();
DisableTPUChans();

printf("\nIs there life out there ? (5 seconds to hit keyboard)\n");
if (SerTimedGetByte(5000) != -1)
  LIFE = TRUE;

if (LIFE)
  Interact();
else
  GenerateCycles(GP.start, GP.Cycoffs, GP.WinOffs);

now = RtcToCtm();
i = 0;
do {
if (now > cycle[i].start) i++;
} while (now > cycle[i].start);

for (i; i < GP.cycles; i++)
{
if (i%GP.cycles_to_disc == 0) ZeroPSRAM(PSStart,memsize);
txtptr = PSStart + (i%GP.cycles_to_disc)*blocksize;
datastart = txtptr + hdrblock;
if (((ushort)datastart %2) != 0) datastart += 1;

txtptr = WriteHeader(i,txtptr,GP.Stack_depth,TRUE);
```

```
if (GP.direction == 'T')
counts = Transmit(i,datastart);
else
counts = Receive(i,datastart);

if (counts == 0) break;

txtptr = WriteTailor(counts,txtptr,GP.Stack_depth);

if (((i+1)%GP.cycles_to_disc) == 0)
t = WriteToDisk(DFNUM, GP.cycles_to_disc);

} // End of logging loop

waketime.secs = GP.release;
waketime.ticks = 0;
        SleepTill(waketime);
        Release();

cmd = SerGetByteLP();
printf("\nBACK FROM THE WATERY DEEPS - MISSION ACCOMPLISHED !!!");
printf("\n\nPROGRAM TERMINATED NORMALLY");

}  // main



ulong Transmit(ushort i, char *datastart)
{
ushort TxChan, ADCChan;
ulong counts = 0,samples;
time_tt waketime;

samples = (ulong)GP.TxPeriod/GP.ADCPeriod;

if (cycle[i].component == 'X')
{
TxPower(TX_CH1_ENB);
ADCChan = ADC_TX_X;
TxChan = TPU_TXPOL_X;
}

else
{
TxPower(TX_CH2_ENB);
ADCChan = ADC_TX_Y;
TxChan = TPU_TXPOL_Y;
}

SetupTransmit(cycle[i].component, GP.TxPeriod);
SetupADC(GP.ADCPeriod);

waketime.secs = cycle[i].start;
waketime.ticks = 0;

if (cycle[i].component == 'X')
{
SleepTill(waketime);
CHANPRIOR(15, Disabled);
TriggerTx_X();
}
else
{
SleepTill(waketime);
CHANPRIOR(15, Disabled);
TriggerTx_Y();
```

```
}

counts = LogRTPolled(datastart, GP.Stack_depth, samples, ADCChan, TxChan);

DisableTPUChans();

if (!SetTickRate(OurTickRate))
printf("\n\nERROR SETTING TICK RATE");

TxPower(TX_OFF);

return(counts);

}  // TransmitCycle()



ulong Receive(ushort i, char *datastart)
{
ushort ADCChan;
ulong counts = 0,samples;
time_tt waketime;

samples = (ulong)GP.TxPeriod/GP.ADCPeriod;

if (cycle[i].component == 'X')
{
ADCChan = ADC_RX_X;
}
else
{
ADCChan = ADC_RX_Y;
}

SetupReceive(cycle[i].component, GP.TxPeriod);
SetupADC(GP.ADCPeriod);

waketime.secs = cycle[i].start;
waketime.ticks = 0;

if (cycle[i].component == 'X')
{
SleepTill(waketime);
CHANPRIOR(15, Disabled);
TriggerRxX();
}
else
{
SleepTill(waketime);
CHANPRIOR(15, Disabled);
TriggerRxY();
}

counts = LogRTPolled(datastart, GP.Stack_depth, samples, ADCChan, TPU_TX_REF);

DisableTPUChans();

if (!SetTickRate(OurTickRate))
printf("\n\nERROR SETTING TICK RATE");

return(counts);

} // ReceiveCycle()
```

```
/*****************************************************************************
**   interact.c -- User I/O routines
*****************************************************************************/


#include "myheader.h"

extern struct  General_Parms GP;
extern struct  cycle_struct *cycle;
extern char *PSStart;
extern ushort DFNUM;
extern long   memsize;
extern ulong tcr1;
extern  float tcr2;


void Interact(void)
{
ushort i = 0;

while (1)
{
switch (i)
{
case 0: {
i = ShowSystemParms();
break;
}

case 1: {
i = ShowGeneralParms();
break;
}

case 2: {
i = ShowSchedule();
break;
}

case 3: {
  i = TestMenu();
break;
}

case 4: {
UeeErrCheck(UeeWriteBlock(0, (uchar *)&GP.direction, sizeof(GP)));
return;
break;
}

case 99: {
printf("\n*** Program Aborted by User ***");
UeeErrCheck(UeeWriteBlock(0, (uchar *)&GP.direction, sizeof(GP)));
exit(0);
break;
}

} // switch (i)

UeeErrCheck(UeeWriteBlock(0, (uchar *)&GP.direction, sizeof(GP)));

} // while (1)
} // Interact()
```

```
ushort ShowSystemParms(void)
{
float SyncPeriod;
long FSys;
time_t now;
struct tm *date;
char cmd,s[80];

MonCmd("CLOCK");
if (_TMCR->T2CG != 0)
{
printf("\n\n***** ERROR: The T2CG bit (#9 in TMCR field) must be set");
printf("\n to 0 if you are running an external clock into it. It is ");
printf("\n a write once register, so the program will abort and you ");
printf("\n must change the tmcr field of the options EEPROM accordingly,");
printf("\n save the new setting, and reset the Tattletale. This is done");
printf("\n with the following commands:\n");
printf("\n OPT  (to view present settings)");
printf("\n mm (address of tmcr field);w   (get address from OPT, mm is");
printf("\n                                memory modify, w is for 2 byte word");
printf("\n Type in previous value XOR'd with hex #0200 <return>");
printf("\n . (period)  <return> to get out of memory modify");
printf("\n OPT W  (Write new setting to options EEPROM");
printf("\n RES    (reset) ... and start again\n\n");
return(99);
}

if (GP.T2CLK == 78125) cmd = 'b';
else cmd = 'a';

printf("\nTo which frequency of the master clock is T2CLK jumpered ?\n");
printf("\n (a)  1.25   MHz");
printf("\n (b)  78125  Hz\n");
QueryChar("\nWhich frequency (ab)",cmd,"ab",&cmd);

if (cmd == 'a')
{
GP.T2CLK = 1250000;
tcr2 = 1250000 >> _TMCR->PRSCL2;
}
else
{
GP.T2CLK = 78125;
if (_TMCR->PRSCL2 == 0) tcr2 = 78125;
if (_TMCR->PRSCL2 == 1) tcr2 = (float)78125/2;
if (_TMCR->PRSCL2 == 2) tcr2 = (float)78125/4;
if (_TMCR->PRSCL2 == 3) tcr2 = (float)78125/8;
}


if (QueryYesNo("\n\nDo you want to measure the Sync pulse on IRQ6", TRUE))
{
printf("\nMeasuring Sync Period ... Please Wait");
SyncPeriod = MeasureSyncPeriod();
printf("...Done !\n");
printf("\nThe Period of the Sync pulse is %f seconds", SyncPeriod);
GP.SyncPeriod = (ushort)(SyncPeriod*10) + 1;
printf("\nStored in GP as %hu tenths of seconds", GP.SyncPeriod);
}

else printf("\n...Then the previous Sync Period of %hu tenths of secs will be used.",
GP.SyncPeriod);

FSys = SimGetFSys();

now = RtcToCtm();
date = localtime(&now);
```

```
strftime(s, 80, "%c", date);

printf("\n\n\nSYSTEM PARAMETERS:\n");
printf("\nRTC date and time: %s", s);
printf("\nNominal System Frequency %ld Hz", FSys);
if (GP.T2CLK == 1250000)
printf("\n\nT2CLK is jumpered to %.3f MHz", (float)GP.T2CLK/1000000);
else
printf("\n\nT2CLK is jumpered to %lu Hz", GP.T2CLK);

printf("\n\nThe TPU counter frequencies:\n");
printf("\n tcr1 is set to %7lu Hz", tcr1);
printf("\n tcr2 is set to %10.3f Hz", tcr2);

if (!QueryYesNo("\n\nExit if these values are not correct. Continue ?", TRUE))
return(99);

return(1);

}  // ShowSystemParms()



ushort ShowGeneralParms(void)
{
time_t now, start, finish;
struct tm *date;
char ss[80],sf[80];
char cmd,*config,*name,*survey;
float samples;

while(1)
{
date = localtime(&GP.start);
strftime(ss, 80, "%Y/%m/%d %H:%M:%S", date);
finish = GP.start + GP.cycles*GP.cyc_offs;
date = localtime(&finish);
strftime(sf, 80, "%Y/%m/%d %H:%M:%S", date);

    if (GP.direction == 'R') config = "Receiver";
    else if (GP.direction == 'T') config = "Transmitter";
    else config = "Unknown";
name = GP.Inst_name;
survey = GP.survey;
samples = (float) GP.TxPeriod/GP.ADCPeriod;

printf("\n\n\n GENERAL LOGGING PARAMETERS:");
printf("\n (a)  This is instrument %s", name);
printf("\n (b)  Survey: %s", survey);
printf("\n (c)  Instrument configuration: %s", config);
printf("\n (d)  Transmitter TPUPeriod: %lu, Frequency: %.4f Hz",
GP.TxPeriod,(float) tcr2/GP.TxPeriod);
printf("\n (e)  ADC TPUPeriod: %hu, Frequency: %.4f Hz",
GP.ADCPeriod,(float) tcr2/GP.ADCPeriod);
printf("\n      Calculated samples per frame: %.2f", samples);
printf("\n (f)  Stack Depth: %hu", GP.Stack_depth);
printf("\n (g)  Number of logging cycles: %hu", GP.cycles);
printf("\n (h)  Logging cycle offset: %hu seconds = %.2f minutes",
GP.cyc_offs, (float)GP.cyc_offs/60);
printf("\n (i)  Cycles per disc access: %hu",GP.cycles_to_disc);
printf("\n (j)  1st cycle START time   = %s", ss);
printf("\n      Calculated FINISH time = %s\n", sf);
printf("\n (T)  Go to Bench Tests");
printf("\n (Q)  Quit and exit to monitor");
printf("\n (P)  Proceed to view Window Parameters and optionally Launch");
```

```
printf("\n\nChoose (a..j) to edit parameters, or (TQP) for program flow");
if (!QueryChar("",'T', "abcdefghijTQP", &cmd))
return(99);


switch (cmd)
{
case 'a': {
printf("\n\nInstrument names can be up to 10 characters long");
printf("\nInput new instrument name: ");
if (!InputLine(GP.Inst_name,sizeof(GP.Inst_name)+1))
break;
break;
}

case 'b': {
printf("\n\nThe survey name can be up to 10 characters long.");
printf("\nInput new survey name: ");
if (!InputLine(GP.survey,sizeof(GP.survey)+1))
break;
break;
}


case 'c': {
if (!QueryChar("\n\nChoose Receiver or Transmitter Configuration (RT)",
 GP.direction,"RT",&GP.direction))
   break;
break;
}

case 'd':  {
do {
printf("\n\nThe Transmitter TPU period must be a multiple of 4.");
if (!QueryNum("\nChoose Transmitter TPU period",
"%lu","%lu",&GP.TxPeriod))
break;
} while (GP.TxPeriod%4 != 0);
break;
}

case 'e':  {
if (!QueryUShort("\n\nChoose ADC TPU period","%hu","%hu",
&GP.ADCPeriod))
break;
break;
}

case 'f': {
if (!QueryUShort("\n\nStack Depth","%hu","%hu",
&GP.Stack_depth))
break;
break;
}

case 'g': {
if (!QueryUShort("\n\nNumber of Logging Cycles (Should be even)",
"%hu","%hu",&GP.cycles))
break;
if (GP.cycles_to_disc > GP.cycles)
GP.cycles_to_disc = GP.cycles;
break;
}

case 'h': {
    if (!QueryUShort("\n\nCycle Offset in seconds","%hu","%hu",
```

```
     &GP.cyc_offs))
     break;
    break;
    }

case 'i': {
if (!QueryUShort("\n\nCycles per Disc Access",
"%hu","%hu",&GP.cycles_to_disc))
break;
break;
}

case 'j': {
time(&now);
start = now/1800;   // round next half hour
start = (start + 1)*1800;
start = start + HOURS_TO_START*3600;
date = localtime(&start);
if(!QueryDateTime("\n\nAccept Default or Enter New Start Time",
FALSE, date))
break;
GP.start = mktime(date);
break;
}

case 'T': {
return(3);
break;
}

case 'Q': {
return(99);
break;
}

case 'P': {
return(2);
break;
}

}  // switch

} // while(1)

} // ShowGeneralParms()



ushort ShowSchedule(void)
{
ushort i;
float offset;
char cmd, s[80],sf[80],*config;
struct tm  *date;
time_t now,stop;

if (!Schedule()) return(1);

printf("\n\n LOGGING PARAMETERS:");
printf("\nCycle Dir/Comp                              Disc Stack\n");

for (i=0; i<GP.cycles; i++)
{
date = localtime(&cycle[i].start);
strftime(s,80,"%Y/%m/%d  %H:%M:%S",date);
if (((i+1)%GP.cycles_to_disc) == 0)
```

```
{
offset =(GP.Stack_depth+1)*(float)GP.TxPeriod/tcr2 + DISK_WRITE_SECS + (float)GP.SyncPeriod/10;
stop = cycle[i].start + (time_t)offset;
date = localtime(&stop);
strftime(sf,80,"%Y/%m/%d  %H:%M:%S",date);
printf("\n%3hu%7c%c Start %s DA %hu",i,GP.direction,
  cycle[i].component,s,GP.Stack_depth);
printf("\n Stop %s\n", sf);
}
else
{
offset =(GP.Stack_depth+1)*(float)GP.TxPeriod/tcr2 + (float)GP.SyncPeriod/10;
stop = cycle[i].start + (time_t)offset;
date = localtime(&stop);
strftime(sf,80,"%Y/%m/%d  %H:%M:%S",date);
printf("\n%3hu%7c%c Start %s -- %hu",i,GP.direction,
  cycle[i].component,s,GP.Stack_depth);
printf("\n Stop %s\n", sf);
}

} // for (i=1 to GP.cycles)

printf("\n\n(R) Return to General Parameter Window");
printf("\n(Q) Quit and exit to monitor");
printf("\n(L) LAUNCH WITH PRESENT PARAMETERS !!!\n");

if (!QueryChar("\nChoose (RQL) for flow control",'R',"RQL",&cmd))
return(1);  // Ctrl_C takes you back to general parms menu.

switch (cmd)
{
case 'R': {
return(1);
break;
}

case 'Q': {
return(99);
break;
}

case 'L': {
    if (GP.direction == 'R') config = "Receiver";
    else if (GP.direction == 'T') config = "Transmitter";
    else config = "Unknown";
printf("\n\nInstrument set up as %s",config);

now = RtcToCtm();
date = localtime(&now);
strftime(s,80,"%Y/%m/%d   %H:%M:%S",date);
printf("\n\nThe RTC time is now     %s", s);

date = localtime(&cycle[0].start);
strftime(s,80,"%Y/%m/%d   %H:%M:%S",date);
printf("\nThe START time is       %s", s);

if (!QueryYesNo("\n\nARE YOU SURE YOU WANT TO LAUNCH",FALSE))
break;
printf("\nBye !!!\n\n");
return(4);
break;
}

} // switch (cmd)

} // ShowCycleParms
```

```
ushort TestMenu(void)
{
float SyncPeriod;
char cmd;

while(1)
{
printf("\n\n\n BENCH TESTS:\n");
printf("\n (a)  Reset System Time");
printf("\n (b)  Measure Period of Sync Pulse on IRQ6");
printf("\n (c)  Read ADC voltages");
printf("\n (d)  Test Transmition");
printf("\n (e)  Test Receive Cycle");
printf("\n\n (Q)  Quit (Exit to Monitor)");
printf("\n (R)  Return to General Parameter Menu");

if (!QueryChar("\n\nChoose (abcde) for tests or (QR) for flow control:", 'R',
"abcdeQR", &cmd))
return(99);


switch (cmd)
{
case 'a': {
printf("\n\n");
MonCmd("CLOCK");
break;
}

case 'b': {
printf("\n\nMEASURE SYNC PERIOD");
printf("\nThe Sync Pulse must be Connected to IRQ6 (D11)");
if (!QueryYesNo("\nContinue", TRUE))
break;
while(1)
{
printf("\nWaiting for sync ...");
SyncPeriod = MeasureSyncPeriod();
printf("Done !");
printf("\n\nThe period of the sync pulse is %f seconds",
SyncPeriod);
GP.SyncPeriod = (ushort)(SyncPeriod*10) + 1;
printf("\nStored in GP as %hu tenths of secs", GP.SyncPeriod);
if (!QueryYesNo("\nRepeat Measurement",TRUE))
break;
}  // while(1)
break;
}

case 'c': {
MonCmd("AD");
break;
}

case 'd': {
TestTransmitter(GP.TxPeriod, GP.ADCPeriod, GP.Stack_depth);
break;
}

case 'e': {
TestReceive(GP.TxPeriod, GP.ADCPeriod, GP.Stack_depth);
break;
}
```

```
case 'Q': {
return(99);
break;
}

case 'R': {
return(1);
break;
}

}  // switch

} // while(1)

} // TestMenu()


void TestTransmitter(ulong TxPeriod, ushort ADCPeriod, ushort Stack)
{
char comp = 'X',cmd,*blockptr,*txtptr;
ushort i = 0,TxChan, ADCChan;
ulong counts;
float  t,samples,duration;

printf("\n\nZeroing PSRAM for data acquisition ...");
t = ZeroPSRAM(PSStart, memsize);
printf("Done !");
printf("\n%ld bytes zeroed in %.3f seconds", memsize, t);

while (1)
{
printf("\n\n\n TRANSMITTER TEST:\n");
printf("\n (a)  Transmitter Component: %c", comp);
printf("\n (b)  Transmitter TPU period: %lu, Frequency: %.4f Hz",
TxPeriod,(float)tcr2/TxPeriod);
printf("\n (c)  ADC TPU period: %hu, Frequency %.2f", ADCPeriod,
(float)tcr2/ADCPeriod);
samples = (float)TxPeriod/ADCPeriod;
printf("\n      Samples/Frame: %.2f", samples);
printf("\n (d)  Stack Depth: %hu\n",Stack);
printf("\n (S)  Start Transmitter with above parameters and optionally log current");
printf("\n (W)  Write Logged data to disk");
printf("\n (R)  Return to Bench Tests Menu");

if (!QueryChar("\n\nChoose (abcd) to edit or (SWR) for flow control",'R',
"abcdSWR", &cmd))
break;

switch (cmd)
{
case 'a': {
QueryChar("\n\nChoose Transmitter Component [XY]",comp,
"XY", &comp);
break;
}

case 'b': {
do {
printf("\n\nThe Tx period must be a multiple of 4.");
if (!QueryNum("\nChoose a new Tx TPU Period:","%lu",
    "%lu",&TxPeriod))
break;
} while (TxPeriod%4 != 0);
if ((6*TxPeriod/ADCPeriod + hdrblock) > blocksize)
{
printf("\n\n*** WARNING: THE NUMBER OF SAMPLES LOGGED WITH THESE PARAMETERS");
```

```
printf("\nWILL OVERRUN THE BLOCKSIZE DEFINED IN MYHEADER.H");
}
break;
}

case 'c': {
if (!QueryUShort("\n\nChoose a new ADC TPU Period:",
"%hu","%hu",&ADCPeriod))
break;
if ((6*(float)TxPeriod/ADCPeriod + hdrblock) > blocksize)
{
printf("\n\n*** WARNING: THE NUMBER OF SAMPLES LOGGED WITH THESE PARAMETERS");
printf("\nWILL OVERRUN THE BLOCKSIZE DEFINED IN MYHEADER.H");
}
break;
}

case 'd': {
if (!QueryUShort("\n\nChoose a new stack depth:",
"%hu","%hu",&Stack))
break;
break;
}

case 'S': {
if (comp == 'X')
TxPower(TX_CH1_ENB);
else
TxPower(TX_CH2_ENB);

printf("\n\nThe Transmitter has been powered. Do you want to check ");
if (QueryYesNo("\nthe current monitor offsets on the ADC?",TRUE))
 MonCmd("AD");

// Disable TPU Chan15 to reduce scheduler load during transmission
// MUST ENABLE AGAIN AFTER OR NONE OF THE TIME FUNCTIONS WILL WORK

CHANPRIOR(15, Disabled);

SetupTransmit(comp, TxPeriod);

SetupADC(ADCPeriod);

if (comp == 'X')
{
HOSTSERVREQ(TPU_TXPOL_X, 2);
while (HOSTSERVSTAT(TPU_TXPOL_X) & 3)
;
CHANPRIOR(TPU_TXPOL_X, HighPrior);

HOSTSERVREQ(TPU_TXON_X, 2);
while (HOSTSERVSTAT(TPU_TXON_X) & 3)
;
CHANPRIOR(TPU_TXON_X, HighPrior);
}

else
{
HOSTSERVREQ(TPU_TXPOL_Y, 2);
while (HOSTSERVSTAT(TPU_TXPOL_Y) & 3)
;
CHANPRIOR(TPU_TXPOL_Y, HighPrior);

HOSTSERVREQ(TPU_TXON_Y, 2);
while (HOSTSERVSTAT(TPU_TXON_Y) & 3)
;
CHANPRIOR(TPU_TXON_Y, HighPrior);
```

```
} // if (comp == 'X' else ...)


HOSTSERVREQ(TPU_ADC_TH, 2);
while (HOSTSERVSTAT(TPU_ADC_TH) & 3)
;
CHANPRIOR(TPU_ADC_TH, MiddlePrior);


printf("\n Transmitter should be running... ");

if (QueryYesNo("\nDo you want to log Tx Current", FALSE))
{
duration = (float)Stack*TxPeriod/tcr2;
printf("\nThe measurement will take %.0f seconds, %.2f minutes",
duration, duration/60);

if (comp == 'X')
{
ADCChan = ADC_TX_X;
TxChan = TPU_TXPOL_X;
}
else
{
ADCChan = ADC_TX_Y;
TxChan = TPU_TXPOL_Y;
}

txtptr = PSStart + i*blocksize;
blockptr = txtptr + hdrblock;
if (((ushort)blockptr%2) != 0) blockptr += 1;
printf("\nLogging to %p block ...", blockptr);

txtptr = WriteHeader(i,txtptr,Stack,FALSE);
counts = LogRTPolled(blockptr, Stack, (ushort)samples, ADCChan, TxChan);

DisableTPUChans();

if (!SetTickRate(OurTickRate))
printf("\nError setting tick rate");

TxPower(TX_OFF);
txtptr = WriteTailor(counts,txtptr,Stack);

printf("Done\n%lu samples taken as %hu deep stack + 1 raw frame",
counts, Stack);

i += 1;
ViewRawData(blockptr+4*(ushort)samples+10, (ushort)samples);
ViewStackedData(blockptr, (ushort)samples,Stack);
break;

} // if QueryYesNo(Do you want to log...)

else {
DisableTPUChans();

if (!SetTickRate(OurTickRate))
printf("\nError setting tick rate");

TxPower(TX_OFF);
break;
}

}  // case 'S'
```

```
case 'W': {
if (i == 0)
{
printf("\n\n\nERROR! No data has been logged to write to disk !!!");
break;
}

else
{
printf("\nWriting %hu data records to disk ...",i);
t = WriteToDisk(DFNUM, i);
printf("Done !");
printf("\nDatafiles %hu to %hu written in %.3f seconds",
DFNUM - i, DFNUM - 1, (float) t/GetTickRate());
}
break;

} // case 'W'


case 'R': {
return;
break;
}

} // switch (cmd)

 } // while (1)

} // TestTransmitter()




void TestReceive(ulong TxPeriod, ushort ADCPeriod, ushort  Stack)
{
char cmd,comp = 'X',*blockptr,*txtptr;
ushort i = 0,ADCChan;
ulong counts,samples;
float t,duration;

printf("\n\nZeroing PSRAM for data acquisition ...");
t = ZeroPSRAM(PSStart, memsize);
printf("Done !");
printf("\n%ld bytes zeroed in %.3f seconds", memsize, t);

while(1) {
printf("\n\n RECEIVER TEST:\n");
printf("\n (a)  Receiver component: %c", comp);
printf("\n (b)  Stack depth: %hu", Stack);
printf("\n (c)  ADC TPU Period: %hu, Frequency: %.2f",
  ADCPeriod,(float)tcr2/ADCPeriod);
printf("\n      Stack TPU Period: %lu, Frequency: %.4f",
TxPeriod,(float)tcr2/TxPeriod);
samples = (ulong)TxPeriod/ADCPeriod;
printf("\n      Samples/Frame: %lu\n",samples);
printf("\n (L)  Log data and optionally view it");
printf("\n (W)  Write logged data to disc");
printf("\n (R)  Return to Bench Tests Menu\n");

if (!QueryChar("\nChoose (abc) to edit or (LWR) for flow control:",'R',
"abcLWR", &cmd))
break;

switch (cmd)
{
```

```
case 'a': {
QueryChar("\n\nChoose Receiver Component (XY): ",comp,"XY",&comp);
DisableTPUChans();
break;
}

case 'b': {
if (!QueryUShort("\n\nChoose a new stack depth:",
"%hu","%hu",&Stack))
break;
break;
}

case 'c': {
if (!QueryUShort("\n\nChoose a new ADC TPU Period:",
"%hu","%hu",&ADCPeriod))
break;
if ((6*(float)(GP.TxPeriod/GP.ADCPeriod) + hdrblock) > blocksize)
{
printf("\n\n*** WARNING: THE NUMBER OF SAMPLES LOGGED WITH THESE PARAMETERS");
printf("\nWILL OVERRUN THE BLOCKSIZE DEFINED IN MYHEADER.H");
}
break;
}

case 'L': {
duration = (float)Stack*TxPeriod/tcr2;
printf("\nThe measurement will take %.0f seconds, %.2f minutes",
duration, duration/60);
    DisableTPUChans();
    SetupReceive(comp,TxPeriod);
SetupADC(ADCPeriod);
CHANPRIOR(15, Disabled);

if (comp == 'X')
ADCChan = ADC_RX_X;

else ADCChan = ADC_RX_Y;

txtptr = PSStart + i*blocksize;
blockptr = txtptr + hdrblock;
if (((ushort)blockptr %2) != 0) blockptr += 1;
printf("\n\nLogging to %p block", blockptr);

txtptr = WriteHeader(i,txtptr,Stack,FALSE);

PConfInp(F,6);
while(!Pin(F,6));
while(Pin(F,6));

HOSTSERVREQ(TPU_TX_REF, 2);
while (HOSTSERVSTAT(TPU_TX_REF) & 3)
;
CHANPRIOR(TPU_TX_REF, MiddlePrior);

HOSTSERVREQ(TPU_ADC_TH, 2);
while (HOSTSERVSTAT(TPU_ADC_TH) & 3)
;
CHANPRIOR(TPU_ADC_TH, HighPrior);

counts = LogRTPolled(blockptr, Stack,samples, ADCChan, TPU_TX_REF);
txtptr = WriteTailor(counts,txtptr,Stack);

printf("\nDone: %lu samples taken as %hu deep stack + 1 raw frame",
counts, Stack);

i += 1;
```

```
ViewRawData(blockptr+4*samples, samples);
ViewStackedData(blockptr, samples,Stack);

break;

}  // case 'L'

case 'W': {
if (i == 0)
{
printf("\n\n\nERROR! No data has been logged to write to disk !!!");
break;
}

else
{
printf("\nWriting %hu data records to disk ...",i);
t = WriteToDisk(DFNUM, i);
printf("Done !");
printf("\nDatafiles %hu to %hu written in %.3f seconds",
DFNUM - i, DFNUM - 1, (float) t/GetTickRate());
}
break;

}  // case 'W'


case 'R': {
DisableTPUChans();
if (!SetTickRate(OurTickRate))
  printf("\nERROR SETTING TICK RATE");
return;
break;
}

} // switch (cmd)

}  // while(1)

} // TestReceive()



/*****************************************************************************
** QueryUShort Query user for a ushort numeric value.
**
** Return TRUE for all replies except ctrl-C.  Print prompt string (verbatim)
** followed by optional default value (if defFmt in non-NULL and not a NULL
** string) inside square brackets, followed by a question mark.  Return default
** value if just return pressed, otherwise scan reply using scanFmt string.
**
** NOTES:
** 1. defFmt and scanFmt are scanf specifiers (e.g. "%ld", "lu", "%lx")
** 2. carriage return is not echoed.
*****************************************************************************/
bool QueryUShort(ptr prompt, ptr defFmt, ptr scanFmt, ushort *value)
{
char buf[20];

while (1)
{
printf(prompt);
if (defFmt)
if (*defFmt)
{
printf(" [");
printf(defFmt, *value);
```

```
printf("]");
}
printf(" ? ");

if (! InputLine(buf, sizeof(buf)))
return (FALSE);

if (! *buf) /* just return keyed */
return (TRUE);

if (sscanf(buf, scanFmt, value))
return (TRUE);

if (*prompt != '\n')
putchar('\n'); /* reprompt and try again */
}

} /* QueryUShort() */



void ViewRawData(char *memptr, ulong Samples)
{
ushort j,k,*ptr,modulus = 20;

ptr = (ushort *)memptr;

if (!QueryYesNo("\n\nView raw data?",TRUE))
return;
if (!QueryUShort("\n\nEnter modulus of data to display","%hu","%hu",
&modulus))
return;

for (j=0,k=0; j < Samples; j++,ptr++)
{
if (j%modulus == 0)
{
if ((k%8) == 0)
printf("\n %p   ",ptr);
printf("%8.3f",(float)*ptr*5/4096);
k += 1;
}
}
printf("\n\n");
}  // ViewShortData



void ViewStackedData(char *memptr, ulong Samples, ushort Stack)
{
ushort j,k,modulus=20;
ulong *ptr;

ptr = (ulong *)memptr;

if (!QueryYesNo("\n\nView stacked data?",TRUE))
return;
if (!QueryUShort("\n\nEnter modulus of data to display","%hu","%hu",
&modulus))
return;

for (j=0,k=0; j < Samples; j++,ptr++)
{
if (j%modulus == 0)
{
if ((k%8) == 0)
printf("\n %p   ",ptr);
```

```
printf("%8.3f",(float)*ptr*5/4096/Stack);
k += 1;
}
} // for(j,k)

printf("\n\n");
}  // ViewLongData
```

```
/*****************************************************************************
** utils.c -- utility functions for TDEM program
*****************************************************************************/

#include "myheader.h"

#define SPWM  0x07

extern struct General_Parms GP;
extern struct cycle_struct  *cycle;
extern char *PSStart;
extern long memsize;
extern short DFNUM;
extern ulong tcr1;
extern  float tcr2;


/*****************************************************************************
** Schedule
** This function generates the logging cycle schedule using variables
** from the GP General Parameters structure for start and offsets.
** It first calls the boolean function CheckParms to make sure memory
** blocksize and cycle offsets are adequate.
*****************************************************************************/

bool Schedule(void)
{
ushort i;

if (!CheckParms())
{
if (QueryYesNo("\n\nReturn to main menu to redefine parameters?",TRUE))
return(FALSE);
}

cycle = (struct cycle_struct *)calloc(GP.cycles,sizeof(struct cycle_struct));

for (i=0; i<GP.cycles; i++)
{
if (i == 0) cycle[i].start = GP.start;
else cycle[i].start = cycle[i-1].start+GP.cyc_offs;

if ((GP.direction == 'T') || (i%2 == 0)) cycle[i].component = 'X';
else cycle[i].component = 'Y';

}

return(TRUE);

}  // Schedule()



bool CheckParms(void)
{
time_t period;
bool good = TRUE;
ulong mem;

mem = 6*(float)GP.TxPeriod/GP.ADCPeriod + hdrblock;
if (mem > blocksize)
{
good = FALSE;
printf("\n\n*** WARNING: THE NUMBER OF SAMPLES LOGGED WITH THESE PARAMETERS");
printf("\nWILL OVERRUN THE BLOCKSIZE DEFINED IN MYHEADER.H");
}
```

```
else if (mem*GP.cycles_to_disc > memsize)
{
good = FALSE;
printf("\n\nCheckParms calculates the total memory requirements per");
printf("disc access interval \n to exceed the TT7's PSRAM space of ");
printf("%.2f MBytes.",(float)memsize/1048576);
}

period = (GP.Stack_depth+1)*(float)GP.TxPeriod/tcr2 + DISK_WRITE_SECS + (float)GP.SyncPeriod/10;

if (period > GP.cyc_offs)
{
good = FALSE;
printf("\n\n*** WARNING: THE CYCLE OFFSET TIME IS INSUFFICIENT FOR LOGGING");
printf("\n AND DISC ACCESS.");
}

return(good);

} // CheckParms()


void ConfIOPins(void)
{
// Port and Pin definitions corresponding to
// { DSACK1, AS, SIZ0, SIZ1, IRQ1, PCS2, PCS1, PCS0, DSACK0, AVEC }
// {  E1     E5   E6    E7    F1    D5    D4    D3     E0     E2  }

PConfOutp(E,1); // DSACK1
PConfOutp(E,5); // AS
PConfOutp(E,6); // SIZ0
PConfOutp(E,7); // SIZ1
PConfOutp(D,5); // PCS2
PConfOutp(D,4); // PCS1
PConfOutp(D,3); // PCS0
PConfOutp(E,0); // DSACK0
PConfOutp(E,2); // AVEC
PConfOutp(F,1); // IRQ1

} // ConfIOPins()


void TxPower(ushort byte)
{
SetPins(byte);
Latch(2);
} // TxPower()


void SetPins(ushort byte)
{
ushort bit, i;

for (i = 0; i < 8; i++)
{
bit = (byte >> i) & 0x0001;

switch (i)
{
case 0: { if (bit == 0) PClear(E,1);
else PSet(E,1);
break;
}

case 1: { if (bit == 0) PClear(E,5);
else PSet(E,5);
break;
```

```
}

case 2: { if (bit == 0) PClear(E,6);
else PSet(E,6);
break;
}

case 3: { if (bit == 0) PClear(E,7);
else PSet(E,7);
break;
}

case 4: { if (bit == 0) PClear(F,1);
else PSet(F,1);
break;
}

case 5: { if (bit == 0) PClear(D,5);
else PSet(D,5);
break;
}

case 6: { if (bit == 0) PClear(D,4);
else PSet(D,4);
break;
}

case 7: { if (bit == 0) PClear(D,3);
else PSet(D,3);
break;
}

} // switch (i)

} // for i

} // SetPins()


void Latch(ushort Chip)
{
ushort i;

if (Chip == 1)
{
PSet(E,0);
PClear(E,0);
}
else
{
PSet(E,2);
PClear(E,2);
}

}  // Latch


/*****************************************************************************
** DisableTPUChans
** This function turns off TPU chans 0-14, and configures them as DIO bits
**  set high.  Since the TPU channels are generally disabled after a
** cycle in which TPU 15 was disabled to minimise loading on the scheduler,
** it should be started again with SetTickRate to reinable various timing
** functions including Sleep and SleepTill.
**
```

```
*****************************************************************************/

void DisableTPUChans(void)
{
ushort i;

for (i = 0; i < 15; i++)
{
CHANPRIOR(i, Disabled); // Disable channel
if (i!=2 && i!=5 && i!=14)
TPUSetPin(i, 0); // hold most TPU channels low when not in use
}
TPUSetPin(2,1); // hold gain channels high when not in use
TPUSetPin(5,1);
TPUSetPin(14,1); // hold ADC T/H high when not in use

}  // DisableTPUChans()



char *WriteHeader(ushort i,char *txtptr,ushort Stack,bool LIVE)
{
struct tm *date;
time_t now;
char s[40],*config,*name,*survey;

name = GP.Inst_name;
survey = GP.survey;
if (GP.direction == 'R') config = "Receiver";
else if (GP.direction == 'T') config = "Transmitter";
else config = "Unknown";
if (LIVE) {
date = localtime(&cycle[i].start);
strftime(s, sizeof(s), "%Y/%m/%d %H:%M:%S", date);
txtptr += sprintf(txtptr,"Survey %s",survey);
txtptr += sprintf(txtptr,"\nInstrument %s configured as the %s",name, config);
txtptr += sprintf(txtptr,"\nCycle %hu, %c%c, Starting at %s",i,GP.direction,
cycle[i].component, s);
}

else {
now = RtcToCtm();
date = localtime(&now);
strftime(s, sizeof(s), "%Y/%m/%d %H:%M:%S", date);
txtptr += sprintf(txtptr,"Survey %s TEST",survey);
txtptr += sprintf(txtptr,"\nInstrument %s configured as the %s",name, config);
txtptr += sprintf(txtptr,"\nLogging started at %s",s);
}
txtptr += sprintf(txtptr,"\ntcr2 = %.4f, TxPeriod = %lu, TxRate = %.6f",
tcr2, GP.TxPeriod, (float)tcr2/GP.TxPeriod);
txtptr += sprintf(txtptr,"\nADCPeriod = %hu, ADCRate = %.4f",
GP.ADCPeriod, (float)tcr2/GP.ADCPeriod);
txtptr += sprintf(txtptr,"\nStack depth = %hu",Stack);
txtptr += sprintf(txtptr,"\nSamples per frame = %.2f",
(float)GP.TxPeriod/GP.ADCPeriod);
return(txtptr);

} // WriteHeader()



char *WriteTailor(ulong counts, char *txtptr,ushort Stack)
{
struct tm *date;
time_t now;
char s[40];
```

```
time(&now);
date = localtime(&now);
strftime(s, sizeof(s), "%Y/%m/%d %H:%M:%S", date);
txtptr += sprintf(txtptr,"\n\nFinished at %s", s);
txtptr += sprintf(txtptr,"\n%lu Samples logged as %hu deep stack + 1 raw frame",
counts, Stack);
return(txtptr);
} // WriteTailor()



/*************************************************************************/
/* WriteToDisk                                                           */
/*                                                                        */
/* This function simply writes the number of datafiles to disc  */
/* specified by numfiles.                                               */
/* CAVEAT EMPTOR: the size of the memory block written to the      */
/* Datafiles depends on the choice that was made when formatting   */
/* the disk, and at this point is predetermined. I assume I'm      */
/* working with blocks of 32768, but the datafile size should be   */
/* checked. The files can be  transferred in one spin up to  */
/* minimise power consumption.                                    */
/*************************************************************************/
ulong WriteToDisk(short StartDFNum, ushort numfiles)
{
short i;
char *dfStart; // ptr to beginning of mem block to be copied
time_tt t1, t2; // used to check time to write data
ulong t;

t1 = ttmnow();

DriveOn(FALSE);
DelayMilliSecs(15000);

for (i = 0; i < numfiles; i++)
{
dfStart = PSStart + i*blocksize;
DFWrite(dfStart, StartDFNum + i);
}

DFNUM = DFNUM + numfiles;
DriveOff();
DisableParIO(); // lowers power consumption

t2 = ttmnow();
t = ttmcmp(t2,t1);

// DelayMilliSecs(2000);

// NOTE: SHOULD THINK ABOUT WHETHER TO WAIT THE DISK SPIN DOWN TIME AS ABOVE

return(t);
}



/*************************************************************************/
/* Zero a memory block prior to data aquisition and stacking */
/* The blocksize is set to 32768 to match smallest Datafile size */
/* Note this must be done BEFORE writing header or header will be  */
/* wiped. Timing the loop is just a check but requires TPU15 to be */
/* running with SetTickRate, so this must be done before TPU is set*/
/* up for Tx or Rx and channel 15 is disabled.                    */
/*************************************************************************/
float ZeroPSRAM(char *StartAddr, long numbytes)
{
```

```
short saveSR;
ulong start,stop;
float t;

StopWatchStart();
start = StopWatchTime();

asm  {
movem.l d0-d7/a0-a6,-(A7)
move sr, saveSR ; save state
move.w #0x2700, sr ; don't want rupts in asm cycle
move.l StartAddr, aPTR ; ptr to start of block to clear
move.l numbytes, dSAMP ; number of bytes to zero

 @cont clr.l (aPTR)+ ; faster to clear as longs
  subq.l #4, dSAMP ; counting down
  bne.s @cont ; not done yet

  move.w saveSR, sr ; reenable previous rupts levels
  movem.l (a7)+,d0-d7/a0-a6
  }

  stop = StopWatchTime();
  CHANPRIOR(14,Disabled);
  *CIER = 0;

  stop = stop - start;

  t = (float) stop/1000000;

  return(t);

 } // Zeroblock()




/*****************************************************************************
** Log Real Time Polled
**
** ASSUMES THAT MEMORY BLOCK POINTED TO BY *MEMPTR HAS ALREADY BEEN ZEROED.
**
** This logs data on ADCChan and stacks it in real time: i.e. stacking
** each byte as it comes in. The TPU TxIRQ flag on TxChan is polled with
** every conversion. The TxChan may be either the TxPolarity Channel
** during transmission, or a reference channel when receiving. Each frame
** is terminated when the IRQ flag goes high. "Stack" cycles are
** stacked, then one more cycle is taken into the contiguous memory range
** to provide a raw sample for noise estimation.
**
*****************************************************************************/
ulong LogRTPolled(char *memptr,ushort Stack,ulong Samples, ushort ADCChan,ushort TxChan)

{
short saveSR;
ulong counts;
ushort IRQbit = 0;
char *rawptr; // prt to start of raw data sample

IRQbit = (1 << TxChan); // setup bit for Tx IRQ polling
rawptr = memptr + 4*Samples;

*ADSFR = 0; // initialise ADC
*ADSFR = M_P26FN; // enable T/H conversions from TPU

asm {
```

```
movem.l d0-d7/a0-a6,-(A7) ; save all user registers
move sr, saveSR ; save status register
move #0x2700, sr ; disable IRQs during logging
move ADCChan,dLSB ; use dLSB temporarily to pick ADCChan
lea ADMS, aADMS ; ADC most significant byte
lea ADLS, aADLS ; ADC least significant byte
lea CISR, aCISR ; TPU interrupt status register
lea ADCMD,aADCMD

move.b dLSB,(aADCMD) ; choose multiplexer channel on ADC
move.w Stack, dSTACK ; stack depth passed to function
move.w IRQbit, dMASK ; bit for checking IRQ flag

clr.l dDATA
clr.l dCHECK

eor.w dMASK, (aCISR) ; clear IRQ flag from last cycle

   @txwait move.w (aCISR), dCISR ; wait for next IRQ flag
    and.w IRQbit, dCISR
    beq.s @txwait ; no IRQ yet

   @irq eor.w dMASK, (aCISR) ; clear IRQ flag
    move.w Samples, dSAMP ; samples per cycle
    subq.w #1, dSTACK ; counting cycles stacked
    bmi @raw ; go collect raw frame, don't change ptr
    move.l memptr, aPTR ; ptr to beginning of stack

   @trkng1 move.b (aADMS), dDATA ; msb & busy flag in d7
    bpl.s @trkng1 ; not busy, tracking

   @busy1 move.b (aADMS), dDATA ; msb & busy flag in d7
    bmi.s @busy1 ; busy, converting

    lsl.w #8, dDATA ; shift into MSB position of data word
    move.b (aADLS), dDATA ; shift LSB into lower byte of data word
    add.l dDATA, (aPTR)+ ; add to stack and increment memory ptr

   addq.l #1, dCHECK ; used to check No. of samples logged

    move.w (aCISR), dCISR ; poll Tx IRQ flag
    and.w dMASK, dCISR ; masked check
    bne @irq ; irq true: start new cycle
    subq.w #1, dSAMP ; no irq: continue logging
    bne @trkng1 ; not done: get next sample
    beq @txwait ; done, wait for next TxIRQ to start next cycle

   @raw move.l rawptr, aPTR ; ptr to beginning of raw block

   @trkng2 move.b (aADMS), dDATA ; msb & busy flag in d7
    bpl.s @trkng2 ; not busy, tracking

   @busy2 move.b (aADMS), dDATA ; msb & busy flag in d7
    bmi.s @busy2 ; busy, converting

move.b (aADLS), dLSB ; get LSB
move.b dDATA, (aPTR)+ ; write MSB to mem and incr. ptr
move.b dLSB, (aPTR)+ ; write LSB to mem and incr. ptr

addq.l #1, dCHECK ; counting No. of samples logged

    move.w (aCISR), dCISR ; poll Tx IRQ flag
    and.w dMASK, dCISR ; masked check
bne.s @done ; irq: finished logging
beq @trkng2 ; go get another sample

@done move.l dCHECK, counts ; No. samples taken
```

```
move.b #0, ADSFR ; disable ADC T/H conversions
move.w saveSR, sr ; re-enable rupts
movem.l (a7)+,d0-d7/a0-a6 ; restore user registers

}


return(counts);

} //  LogRTPolled



/*****************************************************************************
** SetupReceive()
** This function sets up the TPU for an Rx cycle. This consists of setting
**  up a Tx Reference Channel running at the Tx frequency to be used
** as a reference in stacking.
** Since the setup is not time critical, channels etc. are handled as variables.
** The ADC and Tx Reference channels will be triggered by the sync on IRQ6.
*****************************************************************************/

void SetupReceive(char comp, ulong TxPeriod)
{
ushort RefHigh, RefPeriod;
ushort RefChan;

/* Make sure TPU channels are configured for output and set them low  */
TPUSetPin(TPU_TX_REF,0);

/* Setup PWM channel running at transmitter frequency to be used as a      */
/* reference in timing the stack. It will be triggered by the external     */
/* sync signal on IRQ6 for synchronisation with the transmitter. Here      */
/* I just set it up.  */

RefHigh = TxPeriod/2;
RefPeriod = TxPeriod;

FUNSEL(TPU_TX_REF, PWM);
HOSTSEQ(TPU_TX_REF, 0);

PRAM[TPU_TX_REF][0] = OutputChan | Cap2Match2 | NoChangePAC | ForceLow;
PRAM[TPU_TX_REF][2] = RefHigh;
PRAM[TPU_TX_REF][3] = RefPeriod;

} // SetupReceive()



/*****************************************************************************
** SetupTransmit()
** This function sets up the TPU channels for a transmission cycle. The
** channels are not started here but by separate triggering functions.
** Since this is just a setup routine, it is not time critical and therefore
** I use variable channels. The triggering routines to start the channels
** after the IRQ6 are very time critical and need to be written individually
** for each channel.
** The TxPolarity and Tx On/Off are set up as linked in SPWM mode with the
** latter running at twice the frequency of the former and phase shifted
** relative to it.
*****************************************************************************/

void SetupTransmit(char comp, ulong TxPeriod)
{
ushort TxPolChan, TxOnChan;
ushort Start_Link_Chan, Link_Channel_Count, Ref_Addr1;
```

```
if (comp == 'x' || comp == 'X')
{
TxPolChan = TPU_TXPOL_X;
TxOnChan  = TPU_TXON_X;
}
else if (comp == 'y' || comp == 'Y')
{
TxPolChan = TPU_TXPOL_Y;
TxOnChan  = TPU_TXON_Y;
}
else printf("\nERROR passing components to SetupTransmit");

/* Configure TPU channels for output and set them low  */

TPUSetPin(TxPolChan, 0);
TPUSetPin(TxOnChan, 0);

/* Set up Polarity channel and On/Off channel as linked. TxPeriod has been  */
/* defined globally in GP.TxPeriod. It should be an integer multiple of 4,  */
/* as warned in the General Parms menu where it was set  */

FUNSEL(TxPolChan, SPWM);
HOSTSEQ(TxPolChan, 2);

Start_Link_Chan = (TxPolChan << 12);
Link_Channel_Count = 0x200;
Ref_Addr1 = (TxPolChan << 4);

PRAM[TxPolChan][0] = OutputChan | Cap2Match2 | NoChangePAC | ForceLow;
PRAM[TxPolChan][2] = TxPeriod/2;
PRAM[TxPolChan][3] = TxPeriod;
PRAM[TxPolChan][4] = Start_Link_Chan | Link_Channel_Count | Ref_Addr1;
PRAM[TxPolChan][5] = 0;

FUNSEL(TxOnChan, SPWM);
HOSTSEQ(TxOnChan, 0);

PRAM[TxOnChan][0] = OutputChan | Cap2Match2 | NoChangePAC | ForceLow;
PRAM[TxOnChan][2] = TxPeriod/4;
PRAM[TxOnChan][3] = TxPeriod/2;
PRAM[TxOnChan][4] = Ref_Addr1;
PRAM[TxOnChan][5] = 0;

} // SetupTransmit()



/*****************************************************************************
** TriggerRxX
** This function polls the IRQ6 bit waiting for a high to low transition to
** trigger the start of ADC and Tx_Ref waveforms. The Tx is given higher
** scheduler priority as it provides the most absolute time reference.
** Since both of these channels are independent of components, we do not
** need separate routines for X and Y as in the transmission triggering.
*****************************************************************************/
void TriggerRxX(void)
{
/* Wait for High to Low transition on IRQ6    */

PConfInp(F,6);     // making sure

while(!Pin(F,6)) // if it starts low, wait it out
;
while (Pin(F,6)) // wait out high
;
```

```
/* Start TPU Channels in order of time priority  */

HOSTSERVREQ(TPU_TX_REF, 2);
while (HOSTSERVSTAT(TPU_TX_REF) & 3)
;
CHANPRIOR(TPU_TX_REF, MiddlePrior);

HOSTSERVREQ(TPU_ADC_TH, 2);
while (HOSTSERVSTAT(TPU_ADC_TH) & 3)
;
CHANPRIOR(TPU_ADC_TH, HighPrior);

} // TriggerRxX()


void TriggerRxY(void)
{
/* Wait for High to Low transition on IRQ6    */

PConfInp(F,6);     // making sure

while(!Pin(F,6)) // if it starts low, wait it out
;
while (Pin(F,6)) // wait out high
;

/* Start TPU Channels in order of time priority  */

HOSTSERVREQ(TPU_TX_REF, 2);
while (HOSTSERVSTAT(TPU_TX_REF) & 3)
;
CHANPRIOR(TPU_TX_REF, MiddlePrior);

HOSTSERVREQ(TPU_ADC_TH, 2);
while (HOSTSERVSTAT(TPU_ADC_TH) & 3)
;
CHANPRIOR(TPU_ADC_TH, HighPrior);

} // TriggerRxY()


/*****************************************************************************
** TriggerTx_X
** This function polls the IRQ6 bit waiting for a high to low transition to
** trigger the start of ADC and Tx_X waveforms. The Tx is given higher
** scheduler priority.
*****************************************************************************/
void TriggerTx_X(void)
{
/* Wait for High to Low transition on IRQ6    */

PConfInp(F,6);     // making sure

while(!Pin(F,6)) // if it starts low, wait it out
;
while (Pin(F,6)) // wait out high
;

/* Start TPU Channels in order of time priority  */

HOSTSERVREQ(TPU_TXPOL_X, 2);
while (HOSTSERVSTAT(TPU_TXPOL_X) & 3)
;
CHANPRIOR(TPU_TXPOL_X, HighPrior);
```

```
HOSTSERVREQ(TPU_TXON_X, 2);
while (HOSTSERVSTAT(TPU_TXON_X) & 3)
;
CHANPRIOR(TPU_TXON_X, HighPrior);

HOSTSERVREQ(TPU_ADC_TH, 2);
while (HOSTSERVSTAT(TPU_ADC_TH) & 3)
;
CHANPRIOR(TPU_ADC_TH, MiddlePrior);

}  // TriggerTx_X



/*****************************************************************************
** TriggerTx_Y
** This function polls the IRQ6 bit waiting for a high to low transition to
** trigger the start of ADC and Tx_Y waveforms. The Tx is given higher
** scheduler priority.
*****************************************************************************/
void TriggerTx_Y(void)
{
/* Wait for High to Low transition on IRQ6    */

PConfInp(F,6);     // making sure

while(!Pin(F,6)) // if it starts low, wait it out
;
while (Pin(F,6)) // wait out high
;

/* Start TPU Channels in order of time priority  */

HOSTSERVREQ(TPU_TXPOL_Y, 2);
while (HOSTSERVSTAT(TPU_TXPOL_Y) & 3)
;
CHANPRIOR(TPU_TXPOL_Y, HighPrior);

HOSTSERVREQ(TPU_TXON_Y, 2);
while (HOSTSERVSTAT(TPU_TXON_Y) & 3)
;
CHANPRIOR(TPU_TXON_Y, HighPrior);

HOSTSERVREQ(TPU_ADC_TH, 2);
while (HOSTSERVSTAT(TPU_ADC_TH) & 3)
;
CHANPRIOR(TPU_ADC_TH, MiddlePrior);

}  // TriggerTx_Y



#define TRACKTIMEFREQ 250000 //  gives 4 us tracktime

void SetupADC(ulong ADCPeriod)
{
ulong tracktime;

/* Gives 4 us tracktime for   tcr2 =1250000   */
/* Gives 3.2 us tracktime for tcr2 = 625000   */
/*       3.2 us               tcr2 = 312500   */
/*       6.4 us               tcr2 = 156250   */
/*      12.8 us               tcr2 =  78125   */
/*  25.6 us              tcr2 = 39062.5  */
/*      51.2 us              tcr2 = 19531.25  */
```

```
/*      102.4 us                tcr2 = 9765.625 */

tracktime = tcr2/TRACKTIMEFREQ;
if (tracktime < 1) tracktime = 1;

if (ADCPeriod < 2*tracktime) printf("\nERROR: INVALID ADC SETTINGS");

/* Setup PWM for track and hold on ADC, but do not start yet.           */
/* Start will be initiated with IRQ1 from external oscillator.          */

TPUSetPin(TPU_ADC_TH, 1);

FUNSEL(TPU_ADC_TH, PWM);
HOSTSEQ(TPU_ADC_TH, 0);

PRAM[TPU_ADC_TH][0] = OutputChan | Cap2Match2 | NoChangePAC | ForceLow;
PRAM[TPU_ADC_TH][2] = ADCPeriod - tracktime;
PRAM[TPU_ADC_TH][3] = ADCPeriod;

} //  SetupADC()



/*****************************************************************************
** MeasureSyncPeriod
** This function uses the TT7 stopwatch functions to measure the period
** of the sync signal on IRQ1. The stopwatch uses TPU channel 14, which
** is also the ADC T/H channel, so care should be taken in its use.
**
*****************************************************************************/
float MeasureSyncPeriod(void)
{
ulong Start, Stop;
float SyncPeriod;

PConfInp(F,6);

StopWatchStart();

while (!Pin(F,6))  // wait out low
;

while (Pin(F,6)) // wait out high
;

Start = StopWatchTime(); // start time at high to low trans.

while (!Pin(F,6))  // wait out low
;

while (Pin(F,6)) // wait out high
;

Stop = StopWatchTime(); // stop time at high to low trans.

CHANPRIOR(14,Disabled);
*CIER = 0;

TPUSetPin(14,1);

Stop = Stop - Start;

SyncPeriod = (float) Stop/1000000;

return(SyncPeriod);
```

```
} // MeasureSyncPeriod()



/*****************************************************************************
** UeeErrCheck
** Checks error codes returned by Uee funtions using error enums in uee.h
*****************************************************************************/

void UeeErrCheck(UeeErr  err)
{
ushort errorLocation;
static char *errmsgs[] =
{
"",
"Busy",
"Can't Access",
"Can't Erase",
"Address Error"
};

if (err == ueeOk)
return;

UeeError(&errorLocation);
printf("\nUEE Error %d @ %x  <%s>\n", err, errorLocation, errmsgs[err]);

return;
}  // UeeErrCheck
```

IMAGE EVALUATION
TEST TARGET (QA-3)

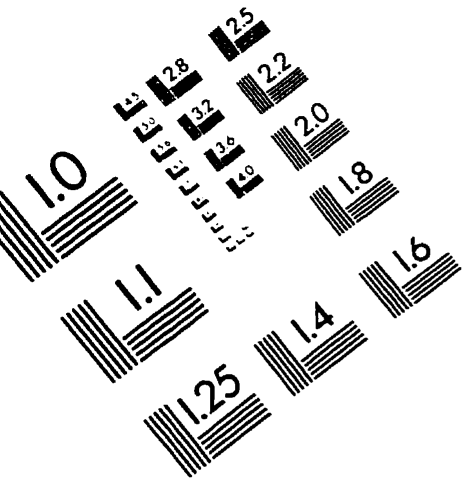

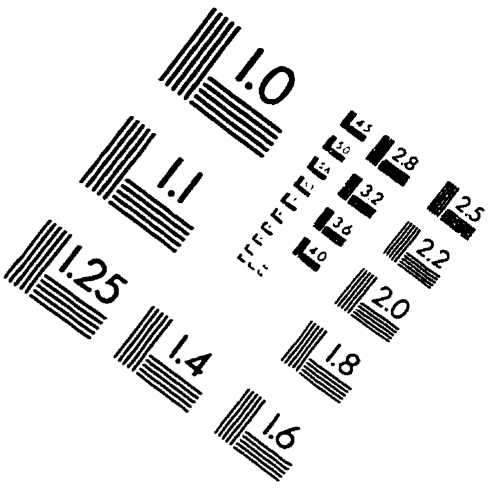

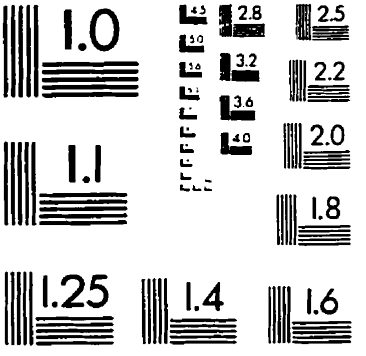

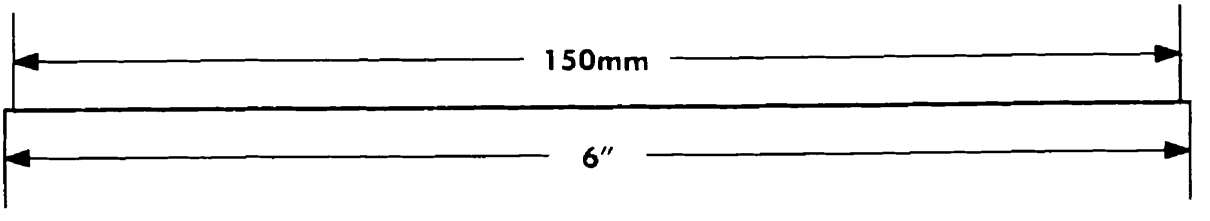

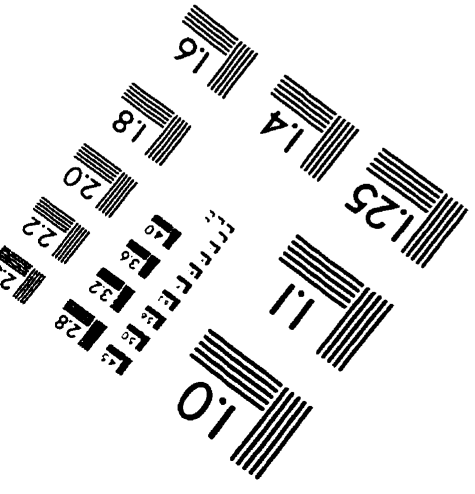

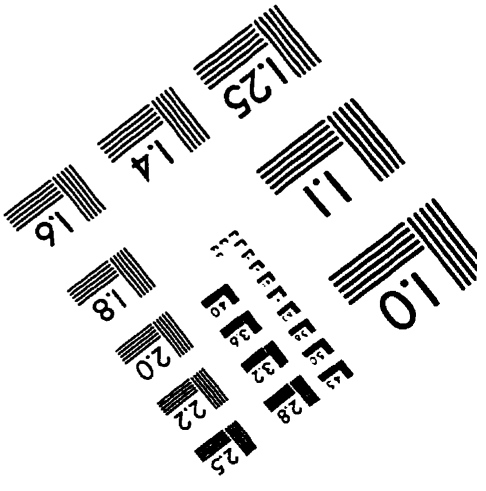

APPLIED IMAGE, Inc
1653 East Main Street
Rochester, NY 14609 USA
Phone: 716/482-0300
Fax: 716/288-5989